TÉCNICO LISBOA

ACADEMIA MILITAR
MILITARY ACADEMY

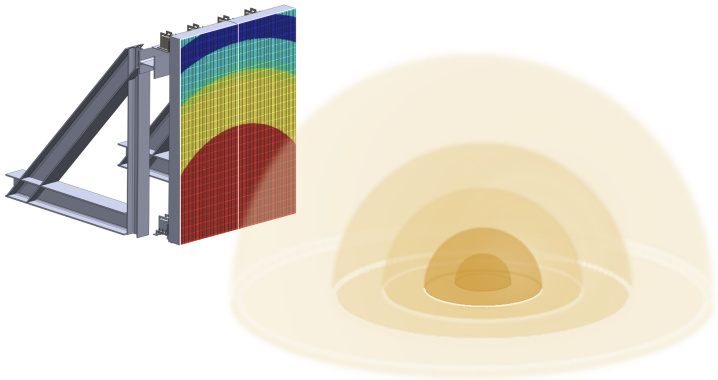

Numerical Analysis of an Innovative Blast Protective System for Buildings

Luís Miguel Marinho Pires

Dissertation to obtain the Master of Science Degree in

Military Engineering

Supervisors: TCor. Eng. Gabriel de Jesus Gomes
Prof. Dr. Eduardo Nuno Brito Santos Júlio

Examination Committee

Chairperson: Prof. Dr. Mário Manuel Paisana dos Santos Lopes
Supervisor: Prof. Dr. Eduardo Nuno Brito Santos Júlio
Members of the Committee: Prof. Dr. Valter José da Guia Lúcio
TCor. Eng. Pedro Gonçalves Matias

November 2021

I declare that this document is an original work of my own authorship and that it fulfills all the requirements of the Code of Conduct and Good Practices of the University of Lisbon.

Preface

The work presented in this thesis was developed at Instituto Superior Técnico (Lisboa, Portugal), complemented with numerical research performed at Academia Militar (Amadora, Portugal), during the period February-October/2021, under the supervision of both TCor. Gabriel Gomes, and Prof. Eduardo Júlio.

The experimental blast data used for the present numerical analysis was methodically carried out by TCor. Gabriel Gomes, inserted in several projects (SI4E - Security and Integrity of Strategic Buildings under Accidental or intentional Explosions or PRINSEF - Protection of Infrastructures and Physical Security), at testing center of Instituto Tecnológico da Marañosa (Madrid, Spain) for research purposes for his doctorate degree in the specialty of structures at Universidade Nova de Lisboa (Lisbon, Portugal).

The solution presented in this work is being developed within the scope of PROTEDES project, lead by School of Science and Technology - NOVA FCT of the New University of Lisbon and counts with the participation of Portuguese Army and Instituto Superior Técnico.

Acknowledgments

Thank you to Escola Secundária de Fafe, to Instituto Superior Técnico (IST) and to Academia Militar (AM) for finding good students and making them great. To IST and AM for allowing me to have access to the best software tools available. For the challenges that enabled me to grow academically, and as a person.

I am also indebted to my supervisors, Prof. Eduardo Júlio and TCor. Eng. Gabriel Gomes for their generosity in having allowed me to pursue my will. For being a shining example of great professionals and friends, for their precious advice and motivation. I have benefited enormously from their guidance since the earlier emails, without which a great number of errors and mistakes I would have made and any that might remain are mine alone.

I also acknowledge Althima - Engineering Software Solution, Lda and Altair Engineering Inc. for providing an Altair license allowing for the development of the CAE simulation conducted during the present dissertation. To Eng. Laura Rosso and Eng. João Lourenço, both responsible for this opportunity.

Likewise, to KeyShot Education, especially to Mr. David Farris who agreed to help by delivering the license to their software, useful to better showcase the models and their components.

To the root of this work, Ten. André Pinto and Ten. Vitor Pereira, that inspired and planted this dream on me. For the countless times that they went beyond what was necessary to help me, even though they didn't have to.

To Eng. Ameen Topa, who helped me understand and solve advanced problems within LS-DYNA software, whose inputs were crucial to accomplish the numerical analysis in the time available.

To Prof. José Moitinho for inspiring me in the realm of numerical analysis, as well as being available to meet and help me understand some theoretical concepts.

To the FOXTROT class, especially Rodolfo Rodrigues for the companionship, the shared procrastination, and the multiple nights struggling getting this project done. To Inês Moreira and Ana Borralho for their support and help with LaTeX system. To Carlos Santos for the graphic aid. To Rui Miguel and Zenda Costa for being generous in reviewing the work and giving feedback.

To Sargento-Chefe Coelho for the help with technical problems within VPN connection and LS-DYNA software license. For saving this dissertation analyses twice!

To TCor. Eng. Matias for being supportive and for allowing me to contribute to this project.

Pouring our heart and soul into a goal can be a selfish time, I know I had my moments, and I am beyond grateful to all those who understood and gave me support. A salute to all my Friends, Teachers, Instructors, and Employees who crossed my path. I leave full of huge learning's, memories, and friendships. To the biggest supporters, my Family. To my Mom, Father and Brother, for all their sacrifices, for teaching me the single most important values of life, hard work and kindness. It's a pride to be yours, this is for you!

Abstract

One of the fundamental principles that must be satisfied, is the safety and protection of human life, which occasionally is threatened by explosions derived from accidents or intentional actions. Studying an innovative protective system for infrastructures against explosions can help mitigate this threat.

Within the scope of TCor. Gabriel Gomes doctoral thesis (in progress) an innovative protective system was developed and successfully tested with proven capabilities. The present work aims to contribute to this study by developing an advanced numerical analysis of this solution. Here the physical system is idealized into a 3D model using SolidWorks. Then the model is divided into elements using HyperMesh. Following the definition of the problem parameters through LS-Prepost, the input is processed by the solver LS-DYNA, and results are reviewed. Additionally, three methods are used to enhance the trust, efficiency, and precision of results. Through benchmarking, mesh convergence, and experimentation, the numerical study aims to comprehend and simulate the system behavior. On top of that, using simulation method, the numerical study aims to explore further ideas and solutions.

Findings reveal that the capacity of the system is high, reducing significantly the blast effects. Even when the system has imperfections, leading to eccentricities, it does not lose its performance, on the contrary, it tends to improve. In the more severe cases, buckling phenomena may occur, but even then, the system always shows deformation by inversion, supporting the effectiveness of this absorption system.

Keywords: Blast; inverted tube; energy-absorption; LS-DYNA; numerical analysis.

Resumo

Um dos princípios fundamentais que deve ser satisfeito, é a segurança e proteção da vida humana, que ocasionalmente é ameaçada por explosões, derivadas de acidentes ou ações intencionais. O estudo de um sistema de proteção inovador para infraestruturas contra explosões pode ajudar a mitigar esta ameaça.

No âmbito da tese de doutoramento do TCor. Gabriel Gomes, em curso, desenvolveu-se um sistema de proteção inovador. Foi testado com sucesso e as suas capacidades foram comprovadas. O presente trabalho pretende contribuir através do desenvolvimento de uma análise numérica avançada desta solução. Nesta fase, o sistema físico é idealizado num modelo 3D através do SolidWorks. Depois, o modelo é dividido em elementos recorrendo ao HyperMesh. Após a definição de parâmetros do problema através do LS-Prepost, o produto é processado pelo solver LS-DYNA, e os resultados são posteriormente revistos. Além disso, são utilizados três métodos para aumentar a confiança, eficiência e precisão dos resultados. Através de análise comparativa, convergência de malha e experimentação, o estudo numérico tem como objetivo compreender e simular o comportamento do sistema. Para complementar, através do método de simulação, pretende-se explorar ideias e soluções adicionais.

Os resultados revelam que a capacidade do sistema é elevada, reduzindo significativamente os efeitos da explosão. Mesmo quando o sistema apresenta as suas imperfeições que conduzem a excentricidades, não perde o seu desempenho, muito pelo contrário. Nos casos mais graves, podem ocorrer fenómenos de encurvadura. No entanto, o sistema apresenta sempre deformação por inversão, sustentando a eficácia deste sistema de absorção.

Palavras-chave: Explosão; tubo invertido; absorção de energia; LS-DYNA; análise numérica.

Contents

List of Tables

List of Figures

Nomenclature

α	Angle of Incidence.
β	Decay Coefficient of the Curve.
$\dot{\varepsilon}$	Strain rate.
ϵ_{max}	Elongation Under Maximum Load.
σ	Tensile Strength.
σ_o	Initial Tensile Yield Strength.
σ_u	Tensile Ultimate Strength.
σ_y	Tensile Yield Strength.
$c_{r\alpha}$	Reflection Coefficient.
E	Young's Modulus.
f_{cm}	Mean Concrete Strength.
f_{ctm}	Mean Concrete Tensile Strength.
H^d_{EXP}	Heat of the Explosive in Study Detonation.
H^d_{TNT}	Heat of the TNT Detonation.
i	Specific Impulse.
i_r	Specific Reflected Impulse.
i_s^+	Specific Positive Impulse.
i_s^-	Specific Negative Impulse.
P	Pressure.
P_o	Ambient Pressure.
P_r	Peak Reflected Pressure.

P_{so} Peak Incident Pressure.

R Distance to the Target.

t Time.

t_a Arrival Time of the Blast Front.

t_d Positive Phase Duration of the Simplified Linear Blast-Wave Profile.

t_o^+ Positive Phase Duration.

t_o^- Negative Phase Duration.

W_{EXP} Weight of the Explosive in Study.

W_{TNT_e} Equivalent TNT Weight.

Z Scaled Distance.

Abbreviations

ALE Arbitrary Lagrangian-Eulerian.

CAD Computer-Aided Design.

CCW Counterclockwise Direction.

COR Correction.

CW Clockwise Direction.

EAC Energy Absorption Core.

EAD Energy Absorption Device.

HE High Explosive.

IED Improvised Explosive Device.

IVG Initial Velocity Generation.

LBE Load Blast Enhanced.

LSS Load Segment Set.

Chapter 1

Introduction

1.1 Problem and Motivation

Explosives were invented more than one thousand years ago with the development of gunpowder in China, a dangerous mixture that releases its energy when exposed to flames. Later evolved into dynamite, followed by TNT, C4, and others, more safe and powerful. Due to its intrinsic characteristics, its development has been illuminated by the intersection between military necessity and technological adaptation in the face of economic constraints [1]. This is the duality of all explosives: they are capable of many benefits, but they can also be chaotic and deadly.

Our malevolent nature is not a new phenomenon, in virtually every culture in history, it has existed some word for “evil” [2]. One of the tools designed to kill, were and still are, explosive weapons. Many of these events are associated with terrorism, which true cost goes far beyond the casualties and the financial loss.

Terrorism true power lies in its capacity to leverage changes, to create a sense of shock, fear, and outrage. Including consequences on the health and psychological well-being of the survivors, with clear evidence on post-traumatic stress disorders, through an exaggerated perception of the threat [3]. Reminding Seneca’s words, “we suffer more often in imagination than in reality” [4]. Media indirectly can play into terrorist organization’s hands and aid them in their campaign of recruitment. Likewise, political responses that tend to reinforce the situation also enable terrorism movements to continue to recruit. Some authors even imply that it can push democracy to its limits because it increases public support for draconian and anti-democratic attitudes, exacerbates differences between ideological and religious groups, and erodes trust between immigrants and host societies [5].

Focusing on available data, from 2001 to 2019, eighteen Portuguese citizens were killed in terrorist attacks [6], which makes roughly 0,2% of the Portuguese road’s deaths, in the same time period, with almost 9 000 fatalities [7]. However, recent reports available indicate that attackers in Europe seem to gain increasing interest in the use of explosives, especially improvised explosive devices (IED). These can assume many forms, ranging from homemade solutions to sophisticated devices with massive damage capacities. They can also be delivered in numerous ways with ease, from suicide vests to vehicles.

Some are very easy to manufacture, remaining the most preferred, the homemade explosives, whose knowledge can be facilitated online [8, 9].

Subsequently, as a result of the increasing risk of such events around the world, it is imperative to deal with this issue. The implementation of strengthening or protective techniques is a method that may contributes to ensure the survivability of the structures and their occupants.

Protection should be intelligent, thoughtful, and holistic in approach, not blind and expensive, such as hardening against the greatest explosive charge weight that a terrorist might theoretically be able to deliver [3]. Additionally, increasingly more advanced, powerful computational techniques and resources, as well as a substantial increase of publications in this field of research, create the perfect environment to give contributions better than ever before. Moreover, numerical analysis importance has been rising primarily due to their flexibility, the low cost, and the possibilities involved. To be able to translate a real-life problem into a model and then into a solvable mathematical problem makes them an incredible tool. Being able to virtually test new scenarios, understand the dynamics involved, explore new solutions and improve the overall system, contributes strongly to a better, safer, and more affordable protection design.

1.2 Objectives and Methodology

The problem described in the previous section, has increasingly become under the spotlight. Therefore, a great number of impact engineering problems have been investigated during the last decades, especially in the field of the dynamic response of structures in the plastic range. The research project PROTEDES (Protection of Strategic Buildings Against Explosions), where the doctoral thesis of TCor. Gabriel Gomes is included, aims to employ tubes, while focusing on the protection of infrastructures. Nevertheless, one of the most interesting variations, the tube inversion, is adopted. A major limitation of this structure is the lack of reliable information on its deformation mode regarding the dynamic behavior, mainly because most of the existing studies were performed under quasi-static conditions.

The present dissertation aims to contribute to deepen the knowledge of the phenomena, with the following major objectives:

- To present the experimental activity, explaining the mechanism of the energy absorption device, its respective testing campaign, and results;
- To build a highly-detailed 3D model of both the energy-absorption device and the entire protective system, including modelling details, and afterwards to divide these domains into a finite number of elements;
- To perform a numerical analysis with a strong focus on simulating the true dynamic behavior of the protective system against blast effects based on experimental test data provided by Gomes' doctoral thesis;

- To contribute to the development of knowledge in this area, particularly regarding this protection system, addressing:
  - The analysis of the effect of magnitude of the blast wave and initial impact velocity;
  - The understanding of deformation modes, and their mechanisms;
  - The study of the energy dissipation efficiency on the building's shield;
  - The determination of the maximum capacity of the connectors alone and the whole system;
  - The assessment of how the presence of the energy-absorption devices affects the performance of the system;
  - The evaluation of the influence of different scenarios and variables.

This analysis is achieved through a highly-detailed methodology, which prioritizes the simulation of the true behavior of the system, carrying a meticulous characterization of the model. Models constitute the input of the analysis, therefore requiring high detail, which together with appropriate methods avoid error propagation. Some simplifications are possible without compromising the quality of the results, saving computational resources and attaining faster analysis.

Once concluded the modelling stage, the model is meshed and the problem parameters are defined. Afterwards it goes through the solver, producing approximate solutions. Eventually, some methods are applied to further increase the reliability of the results and allow the simulation phase, where new ideas and solutions are numerically tested, saving the costs and work associated to the development of real scale experimental blast testing, thus being an economical and suitable option for extrapolation of other scenarios.

1.3 Dissertation Outline

The present dissertation is organized in 6 Chapters. In the present Chapter 1, a general approach to the problem that motivates this study is outlined and the objectives and the approach adopted are delimited. In Chapter 2, a brief introduction of the state-of-art of explosives as a threat is presented, including the implications of the latter when designing structural elements. It is followed by some knowledge on explosions phenomenon, blast effects and related characteristics parameters, as well as the methods to estimate these. Chapter 3 gives a short introduction and description of the energy-absorption devices, the materials, the campaign testing setup, methods of data acquisition and respective data results which are the foundation of this dissertation. Chapter 4 displays the most relevant steps in numerical analysis explaining the techniques and tools used, as well as the methodology associated. Additionally, the models are briefly described, together with part of their parameters. Chapter 5 features all the significant findings, comparing numerical and experimental results, as well as exploring additional ideas that were not possible experimentally. Finally, in Chapter 6, a summary of the findings and suggestions on future directions of related research are presented.

Chapter 2

Explosions, Blast Effects and Loading

2.1 Introduction

The unpredictable and destructive aftermath posed by explosions can emerge from accidental hazards, such as the gas explosion of 21^{st} of October 2021, in China, killing four people and injuring forty-seven [10], to intentional acts of mankind like the Kabul airport attack of 26^{th} of August 2021, whose blast killed 169 Afghans and 13 American service members, one of the deadliest attacks in the country [11].

Attempts to create terror among combatants and civilians have reached a new significance since the iconic terrorist attack of September 11, 2001. Terrorist organizations have revolutionized the way terrorism is executed. Supported by a powerful propaganda engine, it combines narrative, ideology, and spectacle to achieve levels of popularity and recruitment that any official military organization would like to possess. Europe suffers from this propaganda: lone wolves, terrorist cells, foreign fighters, and a polarized society [12]. Such reality is reflected in Figure 2.1.

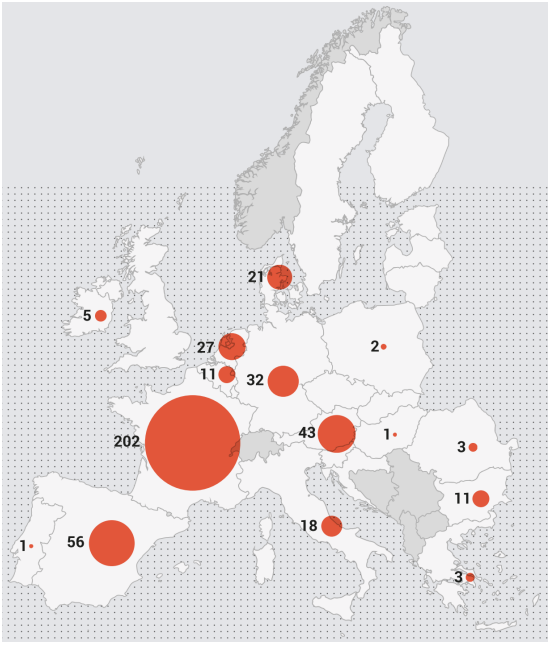

Figure 2.1: Number of suspects arrested for jihadist terrorism in EU Member States in 2019 [13].

In recent decades, considerable awareness has been raised to the improvised explosive device (IED) threats. IEDs are ubiquitous across time and space, its existence goes back to the discovery of explosive chemistry and are currently in use in most countries around the world [14]. According to the literature, non-nuclear explosives are elected as the most prevalent terrorist weapons, often as IEDs carried by suicide bombers [15, 16]. Their use by terrorist groups is a growing problem in modern societies. Non-military institutional buildings, as well as areas with high concentration of people (metro and train stations, stadiums, among others), are the common bombing targets [17].

Explosive devices have become more sophisticated: smaller in size and more powerful, which leads to increased mobility of explosive material and a bigger range of effects [18]. Apart from the rising number of incidents, the injuries they cause are also exponentially worse [19]. Knowledge has been disseminated online, which granted homemade solutions easier than ever before to produce. Hence, the risk for potential losses is increasing. Since most engineering structures are vulnerable to such type of loading, actions should be taken to prevent extreme situations with harmful and destructive effects identical to Figure 2.2. Incidents like the attack in Oklahoma City, USA in 1995, the bombing attack at the World Trade Center, USA in 1993, as well as the accidental Beirut explosion recently in 2020, Lebanon, are good examples, of how a structure failure, including shattered glass, results in far more fatalities and injuries than the blast wave itself [3, 20].

Figure 2.2: Examples of the aftermath of different blast scenarios. First picture from the left, is relative to USA Oklahoma City truck bombing (blast close to surface) [21]. The second image is relative to the USA World Trade Center (underground blast) bombing [22], and the last one, concerning the recent Beirut explosion (blast close to surface) [23].

Therefore, a concern and a need to consider the behavior of engineering structures under blast loading has been established in order to enhance the capacity to predict the effects of an explosive blast for design proposes.

When designing structural elements to resist blast loads, the most effective and least costly mitigation approach is to increase the standoff distance. Nonetheless, this approach requires large perimeters with restricted access for individuals and vehicles, and such perimeters cannot be made infinitely large due to existing structures and urban settings [24, 25]. If sufficient standoff distances are not possible, protective measures and systems should be used alone or combined, such as: a) shielding a structural element; b) provide catching systems to allow existing elements to break, and c) strengthening of the structural elements and connections, which is an option that may be essential to resist progressive collapse [26, 27]. Buildings are designed so that the onset of collapse is not sudden, meaning that there is enough

residual structural capacity to exhibit post-elastic behavior rather than undergoing a sudden, catastrophic failure [3]. Additionally, glazing systems must be considered or alternatives designed for blast loading that minimize injury and damage from glazing fragments and shards [28]. Airborne glass fragmentation remains to be identified as one of the most lethal aspects of building component responses to explosive incidents [24].

During the lifetime of a structure, it is subjected to static and dynamic loading of higher or lower magnitude, being explosions a sporadic event with highly dynamic actions. Explosions have characteristics that make them different from other dynamic loadings, either by their high speed, low duration, and high potential magnitudes. Therefore, a detailed, comprehensive approach of the phenomenon and the dynamic response of the system is required to quantify the blast loading on structures.

Considering what was previously mentioned, [29] suggests four principles of blast design philosophy. Firstly, strengthening the structure should be the last resort. Secondly, one should seek an equal level of protection. Thirdly, it is advisable to follow a resilient design approach. And fourthly, one should never forget that blast is an extreme load.

Of the several informative sources openly available, the most reliable and quoted references to predict explosion parameters and structural response to explosions appear to be some USA military publications, such as those by Baker et al. [30], Kingery and Bulmash [31], and the UFC 3-340-02, made available by the Department of Defense, which gives information and procedures for the design of blast-resistant structures [32].

2.2 Explosions and Blast Effects

Explosions can be both incredible and devastating. Nevertheless, without explosives and explosions, there would be no Panama Canal, no Simplon Tunnel, and very few skyscrapers with firm foundations [33]. Explosions have been categorized with a slight variation over time. Some authors, like Baker et al. [30], defined explosion stored energy system categories as nuclear, chemical, electrical, or pressure energy, while others defined explosion categories as chemical, nuclear, or mechanical [34], or even as natural, chemical, electrical and nuclear [35]. In this research, the most common approach will be followed, which states that explosions categories may be: physical, nuclear, or chemical events [3, 36]. Examples of physical explosions include the failure of a compressed gas cylinder, the eruption of a volcano, or the violent mixing of two liquids at different temperatures. In the event of a nuclear explosion, due to the formation of different atomic nuclei by the readjustment of the protons and neutrons, energy is released [3]. Once chemical events are to a great extent, the most common, the analysis will be focused on them.

The explosion phenomenon can be defined as the combustion of explosive material, a very rapid chemical reaction, faster than the speed of sound which makes a detonation and produces transient air pressure waves, called blast waves. A huge amount of energy and hot gases is produced by an action that only lasts some milliseconds, decaying back to ambient pressure over a short duration of time [33]. During detonation, the hot gases produced expand outwards by pushing the surrounding air through

space, leading to the wave type propagation transmitted spherically and forming a small layer of highly compressed air on the wavefront, the shock wave. It contains a large part of the energy released during detonation and moves faster than the speed of sound [18]. As the shock wave travels moving away from the focus, the air around that region cools down and reduces the pressure. In some cases, it may temporarily drop below ambient pressure until equilibrium occurs.

The velocity of energy release is an important aspect. It can be illustrated by considering compressed air in a pneumatic tire. If this energy is released suddenly, as in a blowout, the effect is that of a small ”explosion”. If, however, there is a slow-release by leakage, this is not an explosion.

2.3 Explosion types

Explosions can be specified in function of their location relatively to the target and the degree of the confinement according to UFC 3-340-02 [32], which provides information and guidance on the construction of structures to withstand the effects of explosions. They can be classified as:

- Confined (or internal) explosions;
- Unconfined (or external) explosions;
- Explosive attached to a structure.

Confined explosions are related to explosions that occur within a building. The corresponding overpressures with the initial shock front will be elevated and will consequently be amplified by successive reflections within the building. Depending on the level of venting, various types of confined explosions are possible.

Non-contact, unconfined explosions, external to a structure will be the ones considered in this research. Therefore, a more in-depth analysis will be herein presented. They can be subdivided into:

- Free-air burst: The explosive charge is detonated in the air, and the origin above the ground is so high that, when the blast wave propagates spherically outwards, it impinges directly onto the target without any prior interaction or amplification, illustrated on Figure 2.3 [30, 32].

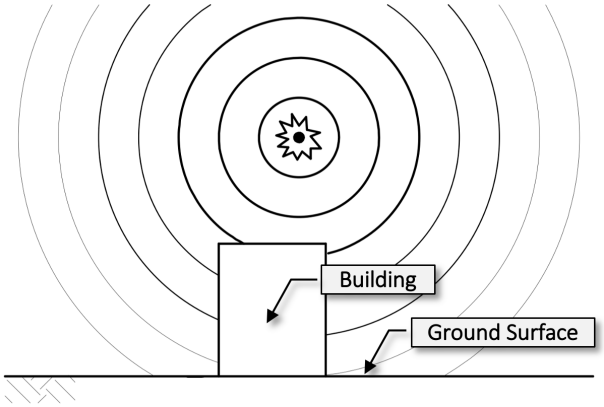

Figure 2.3: Free-air burst explosion adapted from [37].

- Airburst: The explosive charge is detonated in the air, and the initial blast wave propagates spherically outwards and impinges onto the structure after having interacted (reflected) first with the ground, originating a reflected wave, faster than the original incident wave, overlapping it, which creates a Mach front, also called Mach stem. Mach stem is the result of this process, where the reflected wave catches up and fuses with the incident wave, at some point above the reflecting surface to produce a third wavefront. The point where the three waves cross and meet is defined as the triple point, as shown in Figure 2.4 [30, 32].

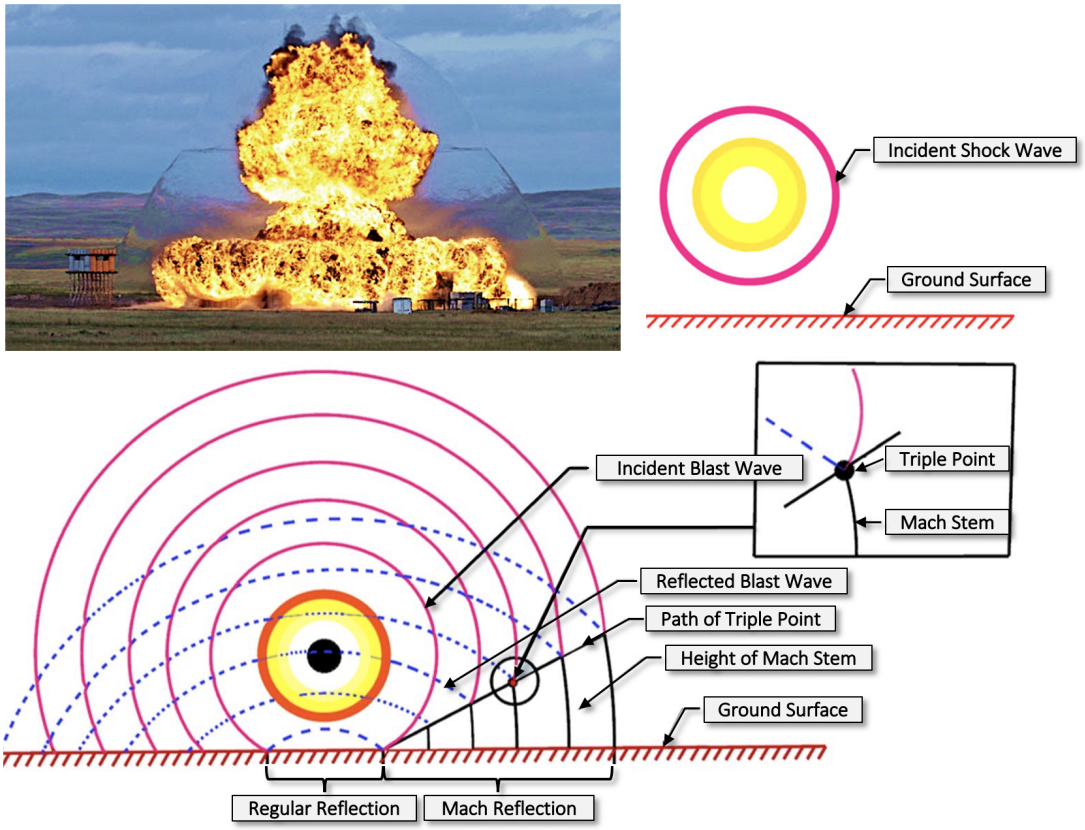

Figure 2.4: Detonation of a TNT explosive close to the ground surface adapted from [38, 39].

- Surface burst: The explosive charge is detonated close to or on the ground surface, as represented in Figure 2.5.

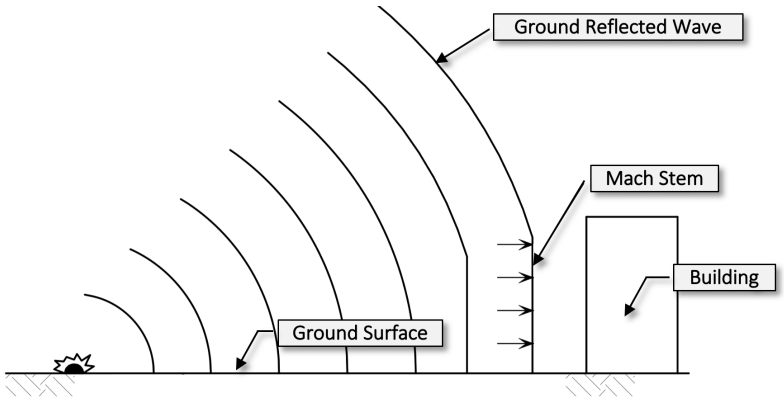

Figure 2.5: Surface burst explosion adapted from [37].

It immediately interacts locally with the ground surface to produce a reflected wave creating inter-medium amplifications before it hits the target. The reflected wave has a superior velocity higher than the initial, overlapping it and propagating hemispherically outwards in group, with pressures over two times those of the original shock wave [30, 32].

2.3.1 Surface burst

Surface burst is the type of explosion adopted in the context of the experimental testing campaign, since it is the most common in terrorist attacks [37]. Unlike the airburst, it creates an immediate interaction between ground and blast wave. So, instead of creating a Mach front at a certain distance from the point of blast initiation, the incident wave is amplified at the point of detonation due to the ground reflections. For a sufficient considerable standoff distance, this wave can be considered locally as a plane, and the pressure loading of a structure can, for practical purposes, be considered uniform [3, 30].

Hypothetically assuming that the ground is a rigid surface, the generated pressure would be twice that produced by the same charge under free-air burst conditions. This observation allows the use of the pressure relationships derived for free-air blasts, also in the case of surface bombings, by doubling the original charge weight. However, as energy generated by the explosion is partially absorbed by the ground, resulting in the formation of a crater and ground shock, the enhancement factor has to be reduced, usually taken as 1.7 to 1.8 [30, 32].

The physical properties along the ground surface from an explosive source on, or close to, the ground depend strongly on the height of the burst. In this case, a significant amount of the energy may create a crater and seismic waves in the ground. For this reason, the properties of the blast wave produced by a hemispherical charge on the ground surface will not be identical to those produced by a spherical mass of twice the size in the free air. As the height of burst is increased, the blast effects at ground zero, the point on the ground immediately beneath the charge, will decrease, but the effects at greater distances may increase. Therefore, there is an optimum height of burst for a given charge size to produce specified blast effects at the greatest possible distance from ground zero. For this reason, the nuclear explosions over Hiroshima and Nagasaki were airburst explosions [40].

2.4 Blast Wave Characterization

During the late 1950s-1980s, blast wave parameters of conventional high explosive (HE) materials have been widely investigated in several studies [30–32, 41]. One of the first attempts to provide and define parameters of the blast wave from a spherical charge of TNT was conducted by Brode [41, 42], which later developed the well-known Brode curves based on the assumption of spherical or hemispherical charge shape. Later, among others, the contributions of Baker's work should be pointed out [30], a compilation from 1984 with collected and correlated data from literally hundreds of other references on experimental data that were the origin of the widely accepted and used Kingery-Bulmash curves [31]. Still, two of the most familiar and recurrent approaches used to define the parameters of the shock

waves were proposed (i) by Kingery and Bulmash [31], being the basis for diagram curves used in the American military criteria, UFC 3-340-02 [32], and TM 5-855-1 [43], and (ii) the expressions from Kinney and Graham [44]. Their formulations are an international reference accepted in the realm of protection design of structures against explosive loadings [45].

All blast wave parameters are graphically sketched in UFC 3-340-02 [32], concerning the scaled distance using the test data collected by Kingery and Bulmash [31]. The Conventional Weapons Program (CONWEP) [46] software (incorporating the high degree polynomial equation as developed by Kingery and Bulmash [31]) is generally used by engineers and researchers who carry out the evaluation of the blast wave parameters, knowing that the pressure-time history is assumed to be similar to modified Friedlander's equation. In this software, the target surface is assumed to be rigid and the wave-structure interaction is neglected. Therefore, the CONWEP results, tend to overestimate the scaled impulse and, by doing so, they become a conservative design tool, which is corroborated by several studies (Børvik et al. [47], Smith et al. [48]). Hence it can be considered satisfactory for practical design purposes only [49]. Moreover, numerical methods can also be used to evaluate the blast wave parameters where fundamental laws of physics are usually implemented using numerical techniques such as the finite element method.

Nowadays, commercially available software, such as ABAQUS, LS-DYNA, AUTODYN and Air3D, are widely used by researchers to determine the blast loads and corresponding structural responses. Several researchers, [50–61], provide the details of the methodology for the prediction blast loads.

When describing blast effects, the relevant parameters primarily depend on the amount of energy released in the detonation [32, 62]. The characteristic parameters of a blast wave are defined for free-air ideal burst conditions as one of the most extensively studied explosion scenarios. For the analysis of structures under blast loading, it is necessary to identify these parameters. The most relevant are:

- P_{so} peak incident pressure, also known as side-on overpressure or peak overpressure;
- t_o^+ positive phase duration;
- i_s^+ positive incident impulse or specific side-on impulse associated with the positive overpressure phase;
- t_a arrival time of the blast front;
- P_r peak reflected pressure;
- i_r reflected specific impulse.

The idealized profile of pressure in relation to time for the case of a free-air blast wave, measured in an element at a certain distance, represented in Figure 2.6, is described from the moment of detonation.

Initially, the pressure on the element is equal to the ambient pressure (P_o), instant (a), and it undergoes an immediate increase, labeled by peak incident pressure (P_{so}), upon the arrival of the shock wave, instant t_a. The time interval necessary for the pressure to reach its peak value is minimal, and for design proposes, it is assumed to be zero, instant (b).

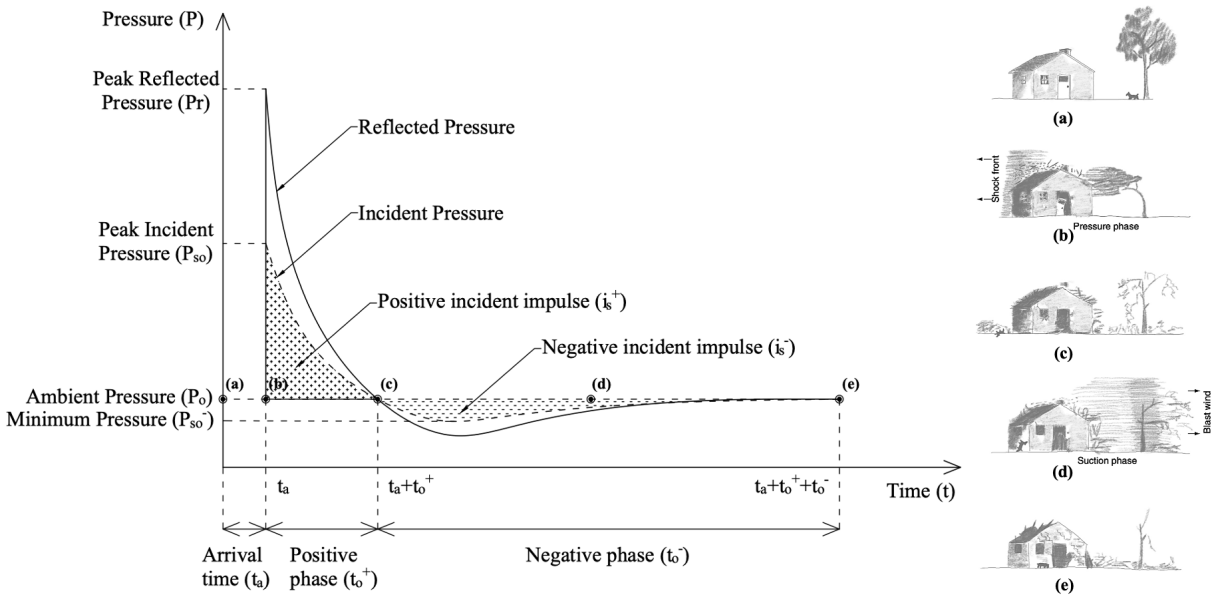

Figure 2.6: Typical air blast pressure profile on the left with respective illustration of its effects on the right, adapted from [3].

The area under the pressure curve corresponds to the impulse caused by the detonation in the structure, being this parameter one of the most relevant in the case of external explosions to characterize the destruction mechanism. The area between t_a and $t_a + t_o^+$ represents the positive impulse i_s^+, and the area linked to the negative phase stands for the negative impulse (i_s).

After its peak value, the pressure decreases rapidly with an exponential rate until it reaches the ambient pressure at $t_a + t_o$, instant (c). Following the positive phase, the pressure becomes lower than the ambient pressure (referred to as negative pressure), instant (d), and finally returns to it, instant (e). In this negative phase, the structures are subjected to suction forces. This is the reason, why sometimes, during blast loading, glass fragments are found towards the origin of the explosion, outside of the buildings instead of in its interior [32, 40]. The negative phase has a longer duration than the positive one, associated with lower pressure values, being minimum pressure defined as P_{so}^-.

The pressure drop through time is usually represented by the modified equation of Friedlander (Equation (2.1)) [30, 32]:

$$P_s(t) = P_{so} \cdot (1 - \frac{t}{t_o^+}) \cdot e^{-\beta \frac{t}{t_o^+}} \tag{2.1}$$

where P_{so} [kPa] corresponds to peak incident pressure, $t_o^+[ms]$ to the duration of the positive phase, $t[ms]$ the period of time after the instant of arrival (t_a), and β is the decay coefficient of the curve.

Blast wave impulses depend not only on the peak overpressure and the wave's duration, but also on the rate of decay of the overpressure [33]. There are several documents with an extensive analysis of possible values for the decay coefficient of the curve and, in general, several authors simplify it by using a constant value for this parameter [30, 32]. When experimental data is available, the decay coefficient can be calculated through a non-linear fitting of an experimental pressure-time curve over its positive phase. It is worth noting that for modeling purposes, in this research, the Friedlander fitting curve will be

used. Being known incident pressure (P_{so}), as well as the positive phase duration (t_o^+), the evaluation of the approximate specific impulses (i_s) produced by the shock wave is possible through the integration of the previous equation, which results in the impulse for the positive phase as can be seen below (Equation (2.2)) [30, 32]:

$$i_s^+ \left[MPa \cdot ms\right] = \int_0^{t_o^+} P_s(t)dt = \frac{P_{so \cdot t_o^+}}{\beta} \cdot \left[1 - \frac{(1 - e^{-\beta})}{\beta}\right] \tag{2.2}$$

Kinney and Graham [44], defined peak incident pressure (or peak overpressure) through the following Equation (2.3), where Z is the scaled distance and W the weight of the explosive:

$$P_{so}\left[MPa\right] = \frac{808 \cdot \left[1 + (\frac{Z}{4.5})^2\right] \cdot P_o}{\left[1 + (\frac{Z}{0.048})^2\right]^{\frac{1}{2}} \cdot \left[1 + (\frac{Z}{0.32})^2\right]^{\frac{1}{2}} \cdot \left[1 + (\frac{Z}{1.35})^2\right]^{\frac{1}{2}}} \tag{2.3}$$

For the positive phase duration calculus, Kinney and Graham [44], suggest Equation (2.4):

$$t_o\left[ms\right] = \frac{980 \cdot \left[1 + (\frac{Z}{0.54})^{10}\right] \cdot W^{\frac{1}{3}}}{\left[1 + (\frac{Z}{0.02})^3\right] \cdot \left[1 + (\frac{Z}{0.74})^6\right] \cdot \left[1 + (\frac{Z}{6.9})^2\right]^{\frac{1}{2}}} \tag{2.4}$$

Kinney and Graham [44], also introduced Equation (2.5), an empirical equation to determine the positive impulse as well:

$$i_s^+ \left[MPa \cdot ms\right] = \frac{0.0067 \cdot \left[1 + (\frac{Z}{0.23})^4\right]^{\frac{1}{2}}}{Z^2 \cdot \left[1 + (\frac{Z}{1.55})^3\right]^{\frac{1}{3}}} \tag{2.5}$$

The negative phase of the shock wave is generally much weaker and more gradual than the positive phase and, therefore, it is usually ignored for design purposes, particularly when it comes to outdoor explosions as [32, 62].

2.4.1 Shock wave reflection

When a shock wave intersects a solid surface, it becomes subjected to amplification and reflection phenomenon, being the reflected peak pressure (P_r) always higher than the incident pressure (P_{so}) that originated it. So, it generates a pressure-time history slightly different than the idealized time history of the typical air blast, even though the duration of the positive phase does not change.

This increment is attributed to the nature of the propagation of the blast wave through the air. While the wave travels, it moves along particles that collide with the surface upon arrival. Hypothetically, in an ideal linear-elastic case, the particles should be able to bounce back freely, leading to a reflected pressure equal to the incident pressure, and the surface would experience approximately the double of the acting pressure (in reality, the blast wave, as a shock wave, is a non-linear phenomenon [32]).

Depending on the incidence angle, three types of reflection can occur [30, 32]:

- Normal reflection, when a surface is perpendicular to the direction of the blast wave, the most

severe case, in terms of loading intensity values;

- Oblique reflection, when the direction of the wave incidence makes a slightly oblique angle with the target surface;
- Mach stem creation, which occurs whenever the wave impinges on a surface at a specific angle, more precisely between 40º and 55º.

The value of the pressure reflected from the surface becomes maximum at the point of normal distance between the detonation source and the surface, as can be observed in Figure 2.7.

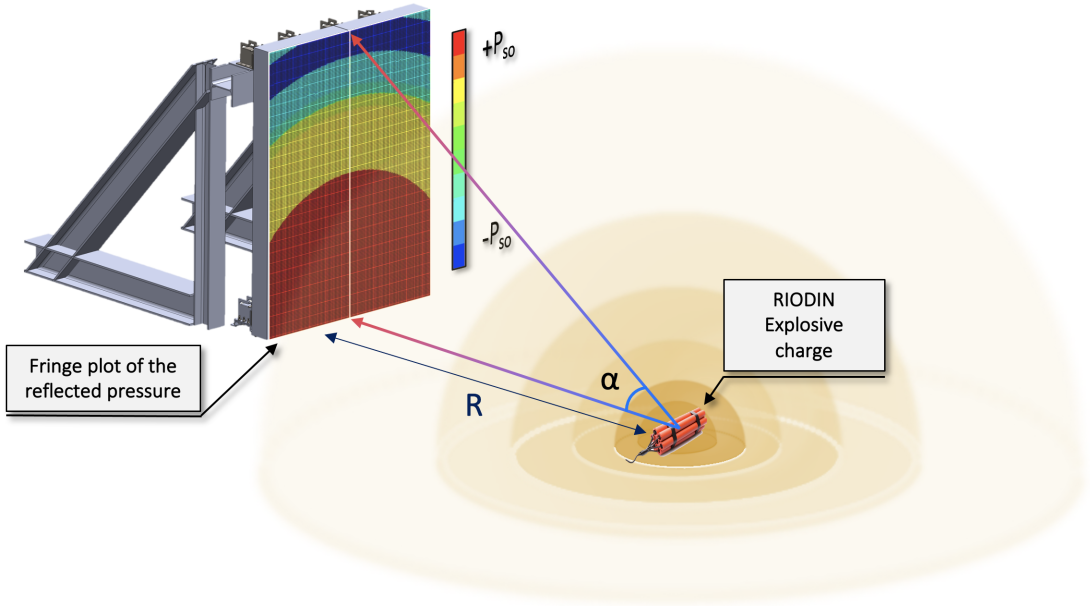

Figure 2.7: Numerical model representation of the reflected pressure on the simulated protective system. This image clearly shows two very important aspects: i) the influence of the impact angle on the magnitude of the reflected pressure, and ii) the fact that the shock wave propagates spherically.

The reflected pressure's value decreases (although not linearly) as the angle of incidence (α) increases. Its minimum value equals the incident pressure (P_{so}) and is created on surfaces perpendicular to the shock front ($\alpha = 90°$).

The reflected pressure (P_r) can be determined by several methods. The most common one is Rankine and Hugoniot method [45]. Considering the ambient pressure (P_o), Equation (2.6) can be derived:

$$P_r\,[MPa] = 2P_{so} \cdot \left(\frac{7P_o + 4P_{so}}{7P_o + P_{so}}\right) \tag{2.6}$$

This equation gives the value of the peak reflected overpressure in the case of reflections at zero angle, where it is assumed that the explosion takes place at standard sea-level conditions. Due to the current circumstances of the loading applied on the experimental campaign, it is taken into account the situation where the shock wave impinges perpendicularly all the target's surfaces, correlated to a normal reflection.

According to it, the maximum and minimum values of the reflected pressure can vary from two to eight times the incident pressure for small and large shocks, respectively. Nevertheless, experimental investigations have concluded that the reflected pressure can be several times higher than eight times

the incident pressure. This is attributed to the fact that under severe blast loads, the air does not behave in an ideal manner, which is an underlying assumption of the mentioned equation, not considering the non-linear effects. It also indicates that the ratio between the normal maximum reflected pressure and the incident pressure is not constant, but depends on the value of the incident pressure.

This equation is only valid in the case of normal reflection ([45]. If there is an angle α (angle of incidence) between the wave propagation direction and the affected surface, the process of reflection might be quite different. This angle affects the resulting reflection and, consequently, the blast loading on a structure, given by the Equation (2.7):

$$c_{r\alpha} = \frac{P_r}{P_{so}} \tag{2.7}$$

This occurrence can be taken into account using a diagram reflection coefficient, $c_{r\alpha}$, which can be found in Appendix A. The effect of the angle of incidence may be neglected, and the structure is studied under the normal reflected pressure, which is on the safe side for most cases, especially if the peak incident pressure is large. More specifically, from the curves of the diagrams, it can be concluded that, whenever the angle of incidence is approximately less than 40º, the use of a normal reflected pressure leads to a conservative design as the normal reflected pressure is higher. For angles of incidence between 40º-55º, the reflected pressure can be underestimated if the assumption of a normal reflection has been made. The reason for this reflected wave behavior for angles of incidence between 40º and 55º is attributed to the creation of a Mach stem.

Being conservative is acceptable for design purposes but not for research purposes. It becomes difficult to compare experimental results with analytical or numerical data.

It is not known a formulation to find out the direct approach of the specific reflective impulse. However, Baker et al. suggested a method [30], regarding Equation (2.8), that agrees reasonably well with experimental data, based on the assumption that the ratio between the incident and reflected impulse is roughly the same as the ratio between the incident and reflected pressure:

$$\frac{i_s}{i_r} = \frac{P_{so}}{P_r} \leftrightarrow i_r = \frac{i_s \cdot Pr}{P_{so}} \tag{2.8}$$

For the design of structures, the peak reflected pressure (P_r) could also be idealized (although very conservative) as an impulse due to a triangular equivalent load, of maximum value P_r and time duration of positive phase of the simplified linear overpressure blast-wave profile (t_d), being the reflected impulse (i_r) given by Equation (2.9) [32]:

$$i_r\,[MPa \cdot ms] = \frac{1}{2} \cdot P_r t_d \tag{2.9}$$

2.5 Scaling Laws

One of the most crucial parameters for blast loading calculations is the distance of the detonation point from the structure considered, the scaled distance in (Z). The effect of distance on blast characteristics can be taken into account by the introducing scaling laws. The most ordinary blast scaling laws are the ones presented by Hopkinson-Cranz and Sachs [3, 30, 32]. These laws can scale parameters, which were defined through experiments, in order to be implemented for a broaden diversity values of distance and charge energy release, a refinement of the Hopkinson scaling of World War I [63], and the Sachs scaling of World War II [64].

Scaled distance is used extensively to determine blast-wave characteristics. The principle behind both formulations is based on the idea that, during detonation, two charges of the same explosive, that have an equivalent geometry but different weight and are set at the same scaled distance from a selected point (under the same atmospheric conditions), produce similar blast waves at the point of interest [30, 32].

According to Hopkinson-Cranz law, a dimensional scaled distance is introduced as described by Equation (2.10):

$$Z = \frac{R}{W^{\frac{1}{3}}} \tag{2.10}$$

where Z is the scaled distance, with units m/kg$^{\frac{1}{3}}$;
R is the range from the center of the charge to the target surface or standoff distance;
W is the weight of an equivalent TNT charge.

Kingery and Bulmash have developed charts to predict spherical and hemispherical airblast parameters concerning the scaled blast distance [31]. These charts are developed based on records from explosive field tests conducted with charge weights from less than 1 kg to over 400,000 kg, at several standoff distances. These empirical charts available, in UFC 3-340-02 [32], are widely used in the literature to predict the characteristics and blast wave parameters.

2.6 TNT Equivalence

The term “TNT equivalence” is always applied to measure the effects of the output of a given explosive by comparing it to that of a TNT explosive [36]. In short, it gives us the relative energy of explosions [65]. TNT is commonly used as the reference standard as its blast characteristics resemble those of most solid-type explosives. Most high explosives, such as TNT, RDX, HMX, C4, and ANFO, produce blast waves with similar, but not identical, properties. Accordingly, the similarity in the properties of the blast waves from such explosives is often quoted in terms of the equivalency of TNT [36, 40, 65]. Additionally, more information is available about the properties of the blast waves produced by TNT than by any other explosive.

This data includes information about the properties of blast waves from so-called free-air, height-of-burst, and surface-burst explosions [40]. Thus, TNT equivalence allows obtaining the same energy of the explosive's blast, impulse, and shock wave in study. The effortless way of accomplishing this is to multiply the mass of the explosive by a conversion factor based on its specific energy and mass of TNT. Conversion factors for a range of explosives are shown in Table 2.1, adapted from Baker et al. [30].

Table 2.1: Conversion factors for a range of explosives [66].

Explosive	Mass Specific Energy $Q_x(kJ/kg)$	TNT Equivalent (Q_x/Q_{TNT})
Amatol 80/20 (80% ammonium nitrate 20% TNT)	2650	0.586
Compound B (60% RDX, 40% TNT)	5190	1.148
RDX (Cyclonite)	5360	1.185
HMX	5680	1.256
Lead azide	1540	0.340
Mercury fulminate	1790	0.395
Nitroglycerin (liquid)	6700	1.481
PETN	5800	1.282
Pentolite 50/50 (50% PETN 50% TNT)	5110	1.129
Tetryl	4520	1.000
TNT	4520	1.000
Torpex (42% RDX, 40% TNT, 18% Aluminium)	7540	1.667
Blasting gelatin (91% nitroglycerin, 7.9% nitrocellulose, 0.9% antacid, 0.2% water)	4520	1.000
60% Nitroglycerin dynamite	2710	0.600

Thus, based on the previous data, a 100 kg charge of PETN converts to 128,2 kg of TNT, since the ratio of the specific energies is 5800/4520 (= 1.283).

An alternative approach considers two conversion factors. The choice of which to use depends on whether the peak overpressure or the impulse delivered of the actual explosive is to be matched to the TNT equivalent. Table 2.2, adapted from the document TM5-855-1 [43], gives examples of these alternative conversion factors.

There are many ways to determine the TNT equivalence, such as heat of detonation, detonation energy, and afterburn energy measured by blast pressure [32, 36, 40]. These approaches may give different TNT equivalence estimations of explosives. For example, the power of an explosive can be measured by the heat of the explosion, which is function of internal energy, developed pressure, and gases produced [32].

Table 2.2: Indicative TNT equivalencies for common explosive materials [35].

Type of explosive	Pressure	Impulse
Comp. B	1.11	0.98
Comp. A-3	1.09	1.08
ANFO	0.90	0.90
Comp. C4	1.37	1.19
Cyclotol (70/30)	1.14	1.09
HBX-1	1.17	1.16
HBX-3	1.14	0.97
H-6	1.38	1.15
Minol-2	1.20	1.11
PETN	1.14	1.15
TRITONAL	1.07	0.96
Pentolite	1.42	1.00
Tetryl	1.07	1.07
TNT	1.00	1.00

An equivalent TNT weight can be determined through Equation (2.11), utilizing the ratio of the heat produced during detonation [32]:

$$W_{TNT_e} = \frac{H^d_{EXP}}{H^d_{TNT}} \cdot W_{EXP} \tag{2.11}$$

where W_{TNT_e} represents the equivalent TNT weight $[kg]$;
W_{EXP} the weight of the explosive in study $[kg]$;
H^d_{EXP} the heat of the detonation of the actual explosive $[MJ/kg]$;
H^d_{TNT} the heat of the TNT detonation $[MJ/kg]$;

Chapter 3

Protective Solution and Experimental Results

3.1 Introduction

Current literature lacks reliable information on open sources regarding the dynamic behavior of energy absorption devices adopted against blast effects. This work is part of two ongoing complimentary projects, that are trying to develop high performance protective solutions against blast loading, namely BLADE [1] and PROTEDES[2]. The former with an experimental nature, is focused on using shielding systems to improve structural behaviour of buildings and blast-resistant protective walls; the latter with a wider scope, still intended to study in detail the structural behaviour of several solutions.

The protective system developed and tested experimentally is based on a rigid panel (reinforced concrete) to which are connected a plurality of ductile metallic connectors, designed to explore an inversion mechanism.

The system has three main purposes. Firstly, rigid panels receive the blast directly, which offers protection from flying fragments, impact, and fire. Secondly, plastic deformation of the connectors, dissipates most part of the energy from the explosion, reducing the energy transmitted to the structure. Thirdly, the location of the connectors allows to simultaneously redirect the remaining transferred energy to the slabs of the structure, protecting vulnerable elements (e.g., columns).

3.2 Energy-absorption connector

During the last decades, a significant number of problems have been investigated in the field of energy-absorption connectors, ranging from applications such as crashworthiness in automotive and aircraft industries for the protection of nuclear and offshore facilities.

[1] Blast Protective Walls Design Optimization
[2] Protection of strategic Buildings Against Explosions

3.2.1 Tube

An energy absorber is a system that converts kinetic energy into another form of energy (e.g., plastic deformation). There are several typical energy absorption structures, such as rings [67, 68], tubes [69, 70], honeycomb [71–74], and corrugated structures [75, 76].

In the current research, the kernel element used was a cylindrical tube. Tubular structures performance in terms of energy absorption and failure mechanism has been widely investigated in numerous papers [69, 70]. The dynamic crushing response of circular tubes was also investigated by many researchers, focusing on the transition between global buckling and progressive folding [77, 78]. Moreover, circular tubes energy absorption capacity performed slightly better than square tubes [79]. Triangular tubes were also studied, having the worst performance [80].

3.2.2 Limitations and solution

Axially compressed circular tubes are good variations of these elements for energy dissipation following impact and for that reason have been studied by many researchers [81]. A structure that starts to deform axially can suddenly buckle in the global bending mode, causing a significant drop in the structure's capacity to absorb the impact energy [82]. However, this issue was addressed by using one of the most interesting variations of this structure, the tube inversion, which has the most efficient energy deformation mode among the ones possible. It involves turning the edge of a thin tube made of a ductile material, inside out or outside in. It additionally enables a deformation with a constant inversion load.

Tube inversion mechanism was introduced by the automotive industry and has been later adopted by NASA as a device to obtain "soft" landing of the Apollo lunar module, also having applications as buffer elements in trains and pier fenders [83]. Since then, several attempts have been made to determine the governing geometrical parameters and improve the concept.

For the experimental research carried by Gomes [84], the energy-absorbing samples preparation was carried out in three stages, according to Figure 3.1: a) expansion against a die; b) clamping by welding and c) pre-inversion. After being inverted, the energy absorption core (EAC) is ready for free inversion by dynamic loading.

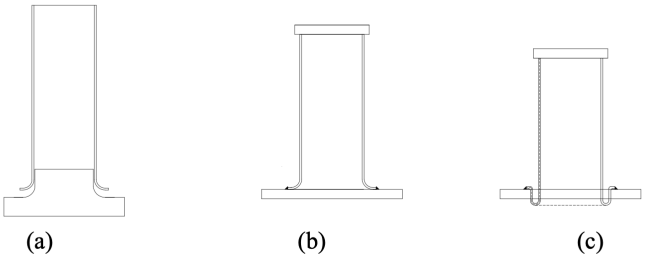

Figure 3.1: Preparation of the inversion mechanism on the energy absorption tubes used.

It is interesting to highlight the fact that the forming load leading to the first stage, expansion, is significantly higher than the inversion load, as shown in Figure 3.2. This is a remarkable aspect. It

means that the tube will not buckle locally, since the inversion force is significantly lower than the forming force. The resulting stress is not enough to cause local buckling and the formation of folds, such as the concertina or diamond deformation modes, usual in axially compressed tubes as illustrated in Figure 3.3.

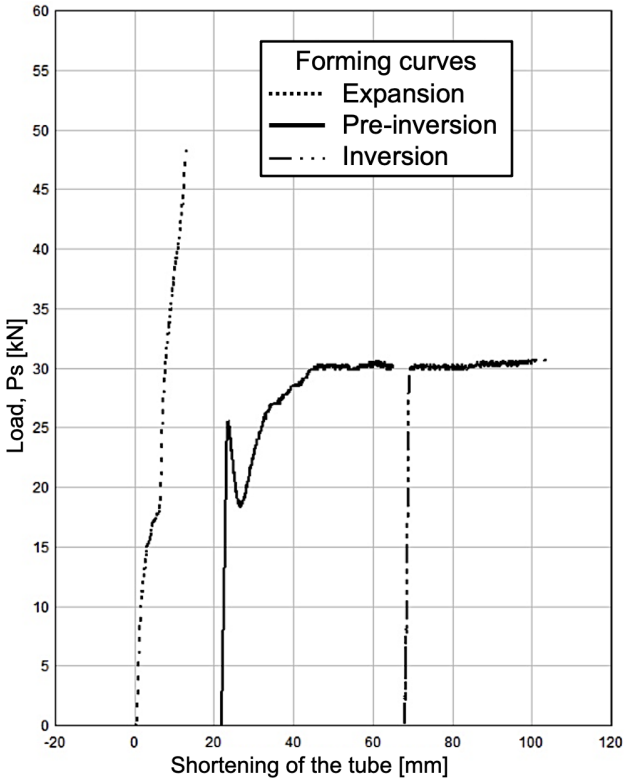

Figure 3.2: Typical load-displacement curves shape for expansion, pre-inversion and post-inversion (54 x 1.5 [mm] tube) [84].

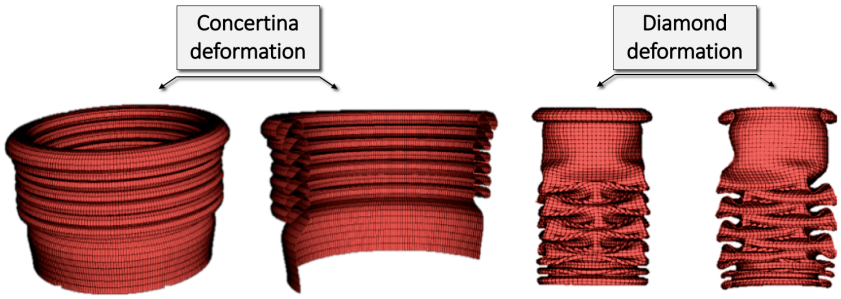

Figure 3.3: Representation of concertina or ring deformation mode [85], and diamond deformation mode [86].

The main advantage of the inverted tube is the constant value of the inversion load, as well as the increased predictability of the deformation behavior. On top of that, when demanded, the tube deforms through an inversion mechanism and does not crush or buckle. The inversion mechanism of deformation is more efficient and can absorb a large amount of energy with a lower peak force.

3.3 Materials

3.3.1 Reinforced Concrete Slab

For this study, sixteen reinforced concrete panels were produced. Material properties were determined by Gomes [27], through tensile tests on steel and uniaxial compressive tests on concrete cylinders. Each panel had the characteristics presented in the following Tables 3.1 to 3.3.

Table 3.1: Reinforced concrete slab characteristics [27]

Concrete	
Strength Class	C25/30
$f_{cm}[MPa]$	33
$f_{ctm}[MPa]$	2.6
Slab dimensions $[m]$	2.75 x 1.00 x 0.21
Concrete cover $[m]$	0.025

Table 3.2: Tensile characteristics of the steel tubes [84].

Specimen $[mm]$	E$[GPa]$	$\sigma_{y(0.2\%)}[MPa]$	$\sigma_u[MPa]$	$\varepsilon_{max}[\%]$
Φ 64 x 2	210.6	371	423	16

Table 3.3: Tensile characteristics of the steel reinforcement [27].

Specimen $[mm]$	E$[GPa]$	$\sigma_{y(0.2\%)}[MPa]$	$\sigma_u[MPa]$	$\varepsilon_{max}[\%]$
Φ 16	200	542	639.3	5

3.3.2 Energy absorption device

In this study, three tube diameters were used (64 mm, 54 mm, and 42 mm) to better understand the inversion mechanism and check the importance of the different influencing parameters. Due to time constraints, the 64 x 2 [mm] was the diameter analyzed in the present research. Physical characteristics are presented in Table 3.4. In Figure 3.4 and Figure 3.5 it is possible to check the application of the tube on the connector, as well as the dynamics of its mechanism.

Table 3.4: Detailed characterization of the tube measurements [84].

Inverted tube 64 x 2 [mm] characteristics	
Nominal diameter $[mm]$	64
Tube thickness $[mm]$	2
Radius (r_o) $[mm]$	32
Plug lenght $[mm]$	30
Plug diameter $[mm]$	58
Inversion radius (r_{inv}) $[mm]$	12
Ratio (r_{inv}/r_o) $[mm]$	0.375
Max compressing force $[kN]$	121
Diameter expanded $[mm]$	90

Figure 3.4: Representation of a section cut from the Energy Absorption Device (EAD), within the protection system [27].

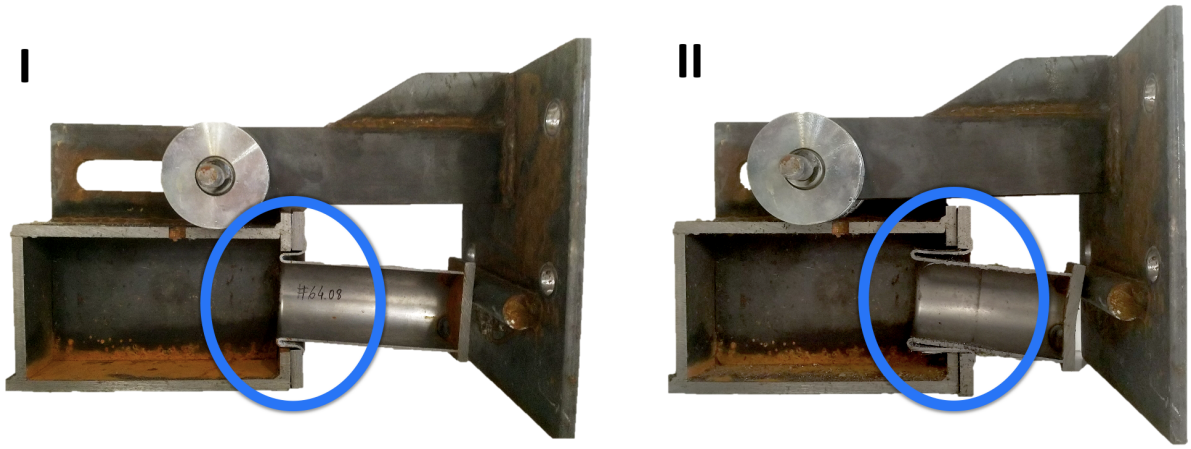

Figure 3.5: Pictures on the cut section of the EAD, where it is clear the inversion mechanism, both taken from the experimental testing campaign. I) Shows the connector before the blast. II) Illustrates the connector after the blast. Reproduced with the authorization of Gomes [27].

3.4 Components

The absorption connector includes several components, as shown in Figure Figure 3.6.

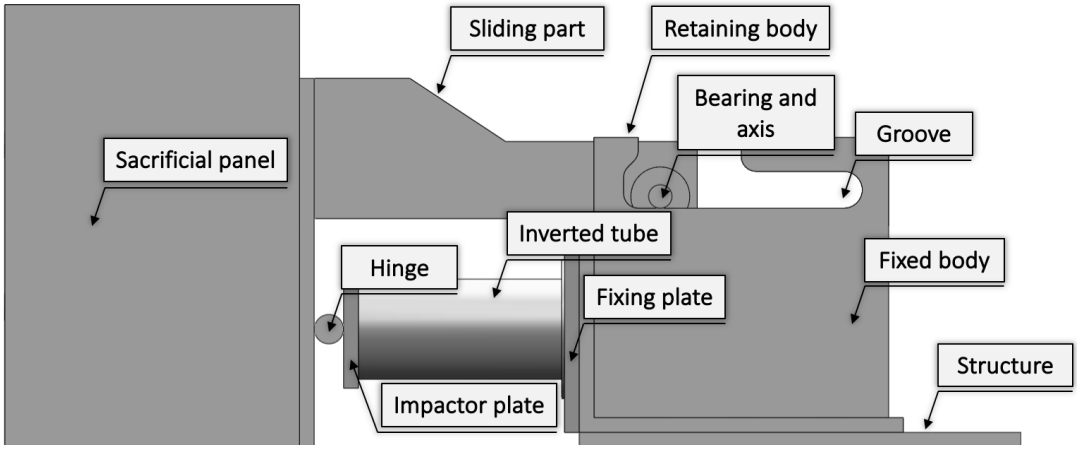

Figure 3.6: Different components that constitute the Energy Absorption Device (EAD).

An overview of these components is given below. The absorption connector has:

- An EAD, constituted by the inverted tube, which is the Energy Absorption Connector (EAC), and the two adjacent outer plates (the impactor plate and the fixing plate) to dissipate the energy by plastic deformation through the inversion mechanism of the inverted tube;
- Two outer plates are positioned on both extremities of the EAC. Being the fixing plate attached to the fixed body;
  - The impactor plate distributes the force transferred from the hinge to the inverted tube;
  - The fixing plate links the EAC to the fixed body. Together, fixing plate and the fixed body contain the inverted tube when the plastic deformation occurs;
  - The fixed body, comprises a retaining mechanism, preventing the sacrificial panel from separating when negative phase effects (suction) occurs.
- A sliding part, the removable body, attached to the sacrificial panel, slides linearly on the fixed body through two bearings (avoiding friction) and is laterally restrained through external grooves that control the shortening of the bodies when inverting the EAC.

3.4.1 Explosive

Regarding the actual explosive, there are a few studies that describe its properties [87], or use it as a charge load [88, 89]. The explosive used in the associated experimental campaign, known by the name of "Goma-2 ECO", commercially sold as RIODIN by MAXAM's, allegedly used in the March 11, 2004 train bombings in Madrid (Spain) by the Al-Qaeda terrorist organization [87], is a Spanish-made high explosive (dynamite) intended primarily for industrial use, such as mining and demolition, or military applications.

RIODIN is available in two designs, HE, high energy release, and XE, the highest energy release found within the MAXAM dynamite family [90], being the latter, the one used, whose characteristics are shown in the following Table 3.5. The blast test was conducted with an explosive load of 60 kg.

Table 3.5: Technical Characteristics of RIODIN XE [90].

Technical Characteristics	
Density Range [g/cm^3]	1.55
Velocity of Detonation [m/s]	5000$-$7500
Gases Volume [L]	842

3.4.2 Blast test setup

The blast testing campaign was conducted at the testing center of the Instituto Tecnológico da Marañosa in Madrid, Experimental setup is arranged radially comprising 4 metallic setups allowing simultaneously testing as illustrated in Figure 3.7. The defined arrangement intends to make the explosion affect all the panels equally.

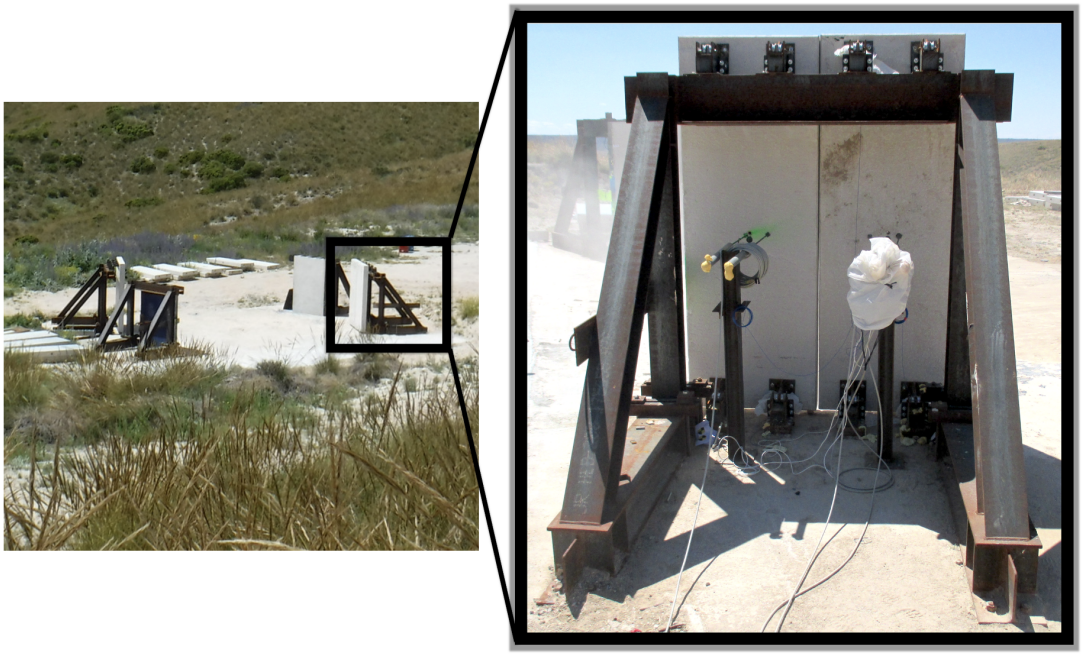

Figure 3.7: Representation of the setup defined in the experimental tests [27].

Three samples have been tested with the 64 x 2 [mm] specimen. The distance between the panel and the explosive was 5.0 m.

3.5 Results data

3.5.1 Pressure

All tests were monitored with pressure gages, allowing tracking of the incident pressure, illustrated in Figure 3.8 [27].

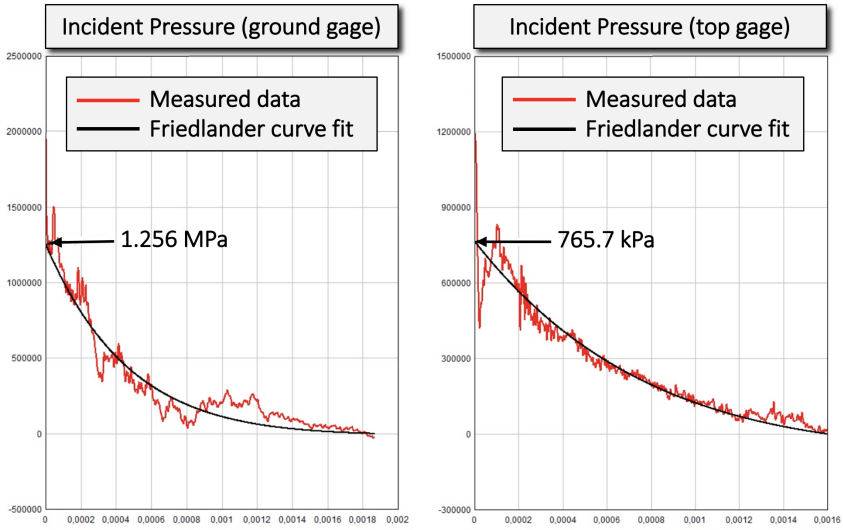

Figure 3.8: Incident pressure data with the Friedlander curve fit adjustment [27].

Nevertheless, some data collected is not valid due to noise from reflections or because some sensors and cables did not survive the testing. The data collected was then adjusted using the Friedlander curve fit for the positive phase as it is recommended.

The experimental results, plotted in Table 3.6 are somehow surprising in comparison with Kingery & Bulmash (K&B) data[3], outlined in Table 3.7. Some interesting aspects can be identified in terms of peak pressures, which are significantly higher than expected. Conversely, the duration of the positive phase it's significantly lower. This is a crucial detail that affected the definition of the blast load in the numerical analysis, which will be explained in detail in the following chapter.

Table 3.6: Experimental data, with the average adjusted parameters for both sensors [27].

Sensor ID	Incident peak pressure $P_{so}\ [kPa]$	Positive phase duration $t_o^+\ [ms]$	Incident Specific Impulse $i_s\ [kPa \cdot ms]$	Decay parameter $\alpha\ [-]$
Ground	1256	1.9	526.82	3.12
Elevated (2.5 m)	765.7	1.9	410.05	1.34

Table 3.7: Kingery-Bulmash parameters.

Kingery-Bulmash parameters for a 60 kg TNT charge at 5 m distance.	
Incident Pressure (kPa)	794.38
Reflected Pressure (kPa)	4084.29
Time of Arrival (ms)	2.87
Shock Front Velocity (m/s)	940.41
Incident Impulse $(kPa \cdot ms)$	799.33
Reflected Impulse $(kPa \cdot ms)$	2506.23
Positive Phase Duration (ms)	8.70

In order to calculate and understand the effects of the blast wave over the system, it's necessary to derive reflected values. A method that agrees reasonably with experiments is suggested by Baker [30]. It states that the relationship between the incident and reflected impulse is roughly the same as the incident and reflected pressure, described in Equation (3.1).

The reflected pressure can be computed by several methods. The most widely used is credited to Rankine & Hugoniot [30] whose calculus can be seen in Equations (3.2) and (3.3). This method, later in the numerical analysis, enabled to simulate blast effects with an alternative method.

$$\frac{i_s}{i_r} \approx \frac{P_{so}}{P_r} \tag{3.1}$$

$$P_r = 2P_{so} \cdot \left(\frac{7P_o + 4P_{so}}{7P_o + P_{so}}\right) = 2 \cdot 1256 \cdot \left(\frac{7 \cdot 101.4 + 4 \cdot 1256}{7 \cdot 101.4 + 1256}\right) = 7326.9\ kPa \tag{3.2}$$

$$\frac{i_s}{i_r} \approx \frac{P_{so}}{P_r} \leftrightarrow i_r = \frac{i_s \cdot P_r}{P_{so}} \leftrightarrow \frac{526.82 \cdot 7326.9}{1256} = 3073.2\ kPa \cdot ms \tag{3.3}$$

Concluding, although the incident specific impulse (i_s) is lower than the estimated following the K&B

[3]Kingery-Bulmash parameters allow to calculate blast-wave parameters of a hemispherical blast based on empirical relations [31]. Allowing the comparison of incident pressure, reflected pressure, incident impulse, reflected impulse, duration of positive phase, time of arrival of the shock wave, and shock front velocity values.

model, primarily due to the very short duration of the blast wave, surprisingly, the reflected impulse (i_r) derived it's much higher than expected ($3073.2\,MPa \cdot ms \gg 2506.23\,MPa \cdot ms$). Comparatively, the data measured would be equivalent to a TNT charge of 112 kg or 77 kg, respectively, in pressure and impulse equivalences.

3.5.2 Impact angle

Another interesting, although expected observation, is that the pressures measured by the elevated sensor were lower than the one on the ground. The reason for this effect is the impact angle, which when increases, values of pressure decrease. The analysis of the footage from high-speed cameras, as well as the numerical analysis, also show this phenomenon where the pressure wave is not planar, starting impinging the wall from the bottom to the top (Figure 3.9). This creates a differential (and decreasing) pressure along the slab length, playing a remarkable influence on the system's behavior.

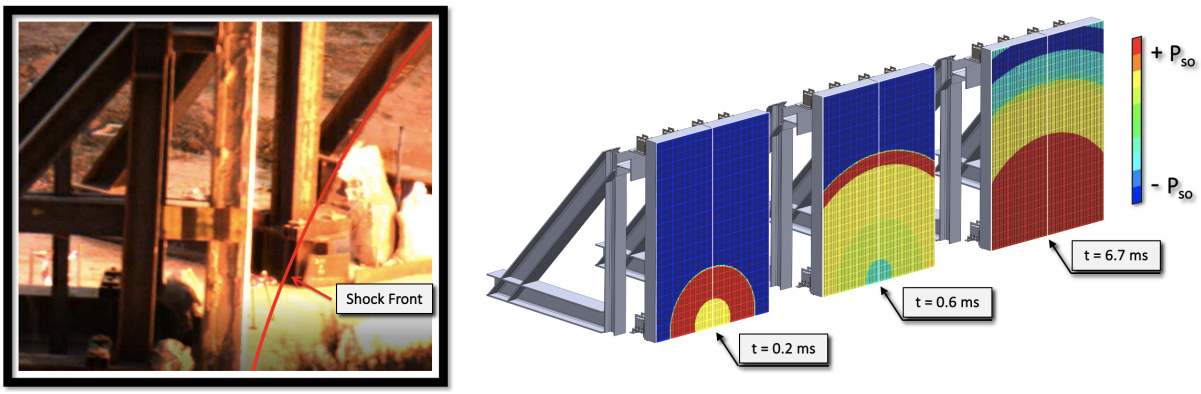

Figure 3.9: On the left, representation of the footage from high-speed cameras [27]. On the right, representation of pressure fringe plot across three-time intervals from the numerical analysis, to capture the influence of impact angle over time, across the slab length.

3.5.3 Pendulum Effect

In the experimental campaign, there were a few inconveniences that needed to be considered. From the Figure 3.10, it is evident the existence of a slight rotation of the slab. Three aspects may help to explain this effect, in particular:

- The mentioned effect was verified experimentally, where blast pressure on the wall increases from the ground level to the top;
- Additionally, the panel support system is suspended over the top connectors, leaving the bottom connectors almost free to move back and forth, aided by the bearings in the sliding part, which could further promote this effect;
- In one case, support plates from the fixed body, attached to the ground with bolts, were ripped out, further enabling this effect.

Figure 3.10: Representation of the rotational effects verified in the most severe cases [27].

3.5.4 Shortening deformation

In the first sample, displayed in the previous image, the bolts that attached the connector to the concrete panel were pulled out by the forces exerted on the support, distorting the position of the connector and preventing the complete inversion from occurring. In the face of these invalid data results, it was disregarded. Thus, when considering the specimen 64 x 2 [mm], only the following two out of these three tests were considered valid, presented in Table 3.8.

Table 3.8: Data results on shortening and rotation of the inversion tubes measured after testing campaign [27].

Sample	Location	$L_{initial}$ $[mm]$	L_{final} $[mm]$	Rotation [°]	Shortening $[mm]$	Total Inversion Length $[mm]$
#1	BL	139	75	6	63.8	75
	BR	136	NA	17	6	
	TL	138	133	3	5	
	TR	122	122	0	0	
#2	BL	139	97	3	42	84
	BR	137	97	3	40	
	TL	140	138	3	2	
	TR	141	141	3	0	
#3	BL	139	100	2	39	90
	BR	138	93	3.5	45	
	TL	139	135	3	4	
	TR	138	136	2	2	

Where the abbreviations BL, BR, TL, and TR, refer to each one of the four connectors, precisely: bottom left, bottom right, top left and top right respectively. NA is referent to the not available results from the first sample.

From collected data, an average total inversion length of 87 mm was considered later in the numerical analysis for the calibration and validation of the model. Additionally, to serve as a reference, there were tests with rigid supports, one of the panels, with these specimen connectors, had a deflection at mid span between 42 to 52 mm.

3.5.5 Force

Several force sensors were placed in strategic locations to monitor the forces transmitted to the supports. Although extensive planning was made to monitor blast tests, most of the attempts to get accurate data on force transmitted failed. Two orders of reasons explain it, namely: very high pressures that caused the rupture or disengagement of the connection cables during the test; and significant rotations of the EAC which made collected data invalid. Nevertheless, from all of them, there was at least one per EAC type that performed correctly, as plotted in Figure 3.11.

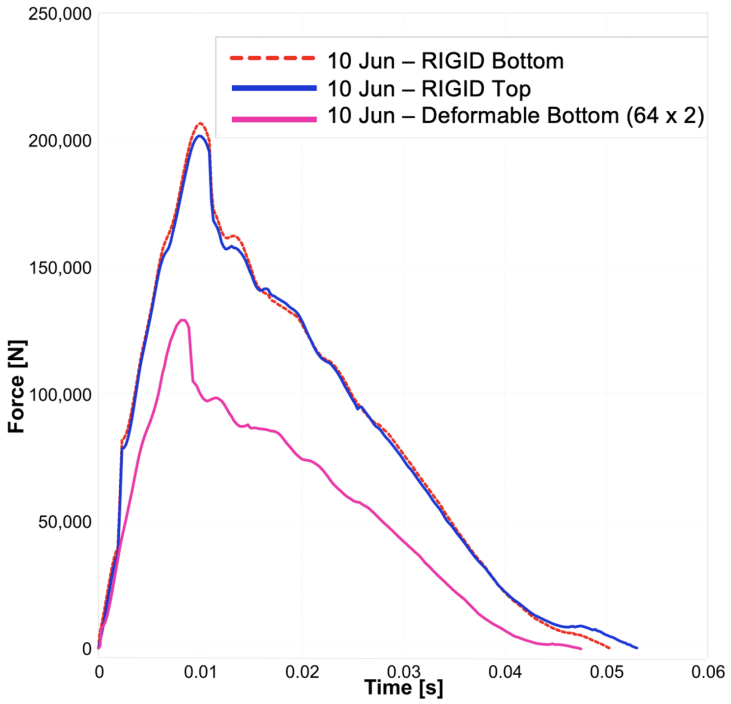

Figure 3.11: Plot of the forces applied with deformable and rigid solutions, due to the blast wave [27].

Plots clearly show the effect of introducing an EAD in reducing the impulse transmitted to the protected structure.

3.5.6 Observations

Additionally and according to the results obtained, the following relevant observations can be made:

- It was observed a differential response at the bottom and top connectors. Particularly, bottom connectors responded more than expected and top connectors. It shows that energy will be absorbed by the easiest path of resistance.
- In one case, part of the energy was absorbed by the bending mechanism (rotation of 17º) and by pulling out the screws from the concrete base.
- Buckling of the tube walls did not occur, even when significant rotation occurred, which represents a promising performance in terms of effectiveness and reliability of the protective system.
- In most cases, an eccentric impact occurred, causing a slight rotation of the EAC.

Chapter 4

Development of Numerical Models

In this chapter, the development of numerical models is presented. First, it is given a brief introduction on the relevant concepts, and methodology used. Then, it is presented in more depth the tools and the characteristics considered. Furthermore, the last version of the models is shown, and insights are given to explain decisions made. Finally, calibration methods are employed to improve efficiency, accuracy and trust in results.

4.1 Introduction

Generally speaking, traditional methods, involve the idealization of physical models through simple equations to obtain solutions. Nonetheless, these approximations oversimplify the problem, and can only provide conservative estimates. These limitations imply that only a tiny portion of real engineering problems can be solved analytically [91, 92].

Alternatively, finite element methods, and other numerical methods, are meant to provide an analysis that considers greater detail, leading to more precise and accurate results. Applications are endless, from heat transfer, stress analysis to other fields [91, 92].

4.2 Finite Element Method

The finite element method is an advanced technique used to solve complex structural analysis problems, illustrated in Figure 4.1. It is based on the idealization of an existing structural system to a mathematical model to be solved with computers that calculate the structural performance. It involves discretizing a geometry into finite elements, connected by nodes and used in a finite element solver to obtain approximate solutions [92].

Additionally, nonlinear finite element analysis techniques have been widely used to analyze structural elements, including reinforced concrete slabs under blast loads. They have proved their ability to effectively capture the damage modes and deformations [93]. The keyword here is approximate since no FEM solution is ever totally accurate.

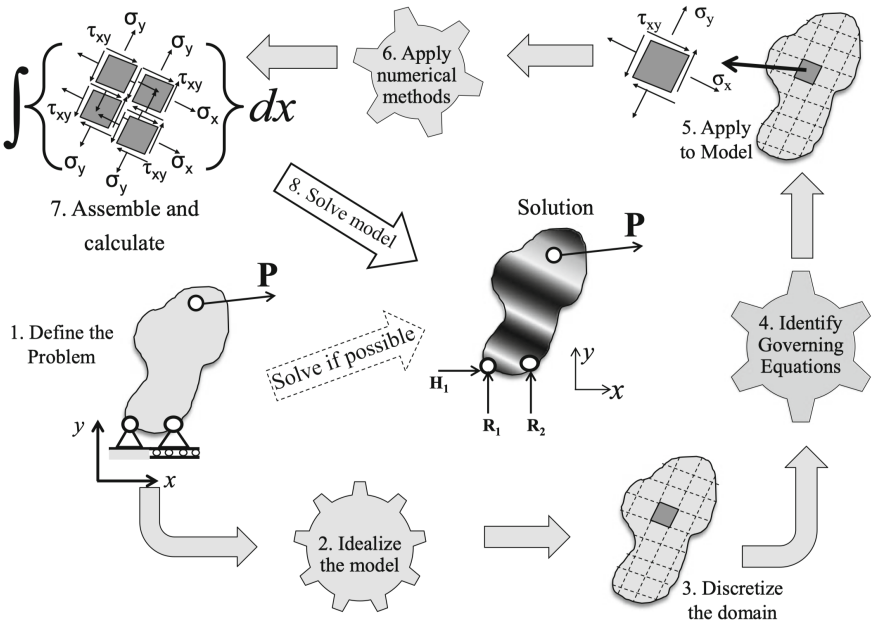

Figure 4.1: Finite element method discriminated in a schematic representation, adapted from [92].

4.3 Methodology

The translation of the protective system and associated testing campaign into a mathematical problem, represented in Figure 4.2, started with the creation of the different individual bodies geometries that constitute the system. This task was conducted with SolidWorks® Academic Version 2020-2021. Afterwards, Altair® HyperMesh® Version 2021 was used as a pre-processor to mesh the geometric model, dividing it into thousands of polygonal shapes, each of them representing an element. Subsequently, LS-Prepost was also used as a pre-processor to define the problem parameters. The analyses were then conducted through the solver LS-DYNA, achieving the problem's approximate solution. Following the analyses, the results were imported once again to LS-Prepost. In this step, the latter was used as a post-processor to convert the output into a readable or visual form.

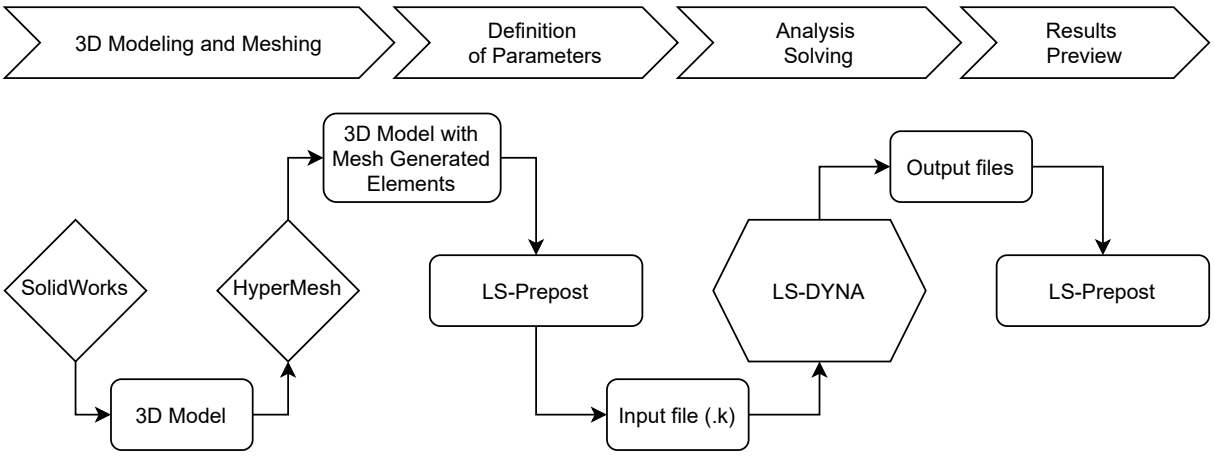

Figure 4.2: Diagram of the different phases of numerical analysis.

Autodesk AutoCAD® 2018.2 Version O.48.M.563 was also used as a secondary tool, to develop part of the load segment method (LSS), read the protective system drawings and create figures.

The methodology outlined was effective, producing good quality results with acceptable error values. To complete the analysis, a set of studies was performed afterwards to increase accuracy and produce a more trustworthy numerical study.

Results, as well as errors, problems, and setbacks are presented, aiming at explaining the methods adopted and the decisions made.

4.4 Software

4.4.1 SolidWorks Modeling

The need for precision, such as considering all the eight critical tube characteristics (nominal diameter, diameter expanded, plug length, plug diameter, tube thickness, inversion radius, radius and the ratio between the inversion radius and the radius), turned the modeling creation process into an unpractical and time-consuming task. Thus, considering the limitations and knowing that details would largely influence the quality of the outputs of the numerical analysis, it was necessary to define an adequate method, which led to SolidWorks, a Computer-Aided Design (CAD) software, which development process is outlined in Figure 4.3.

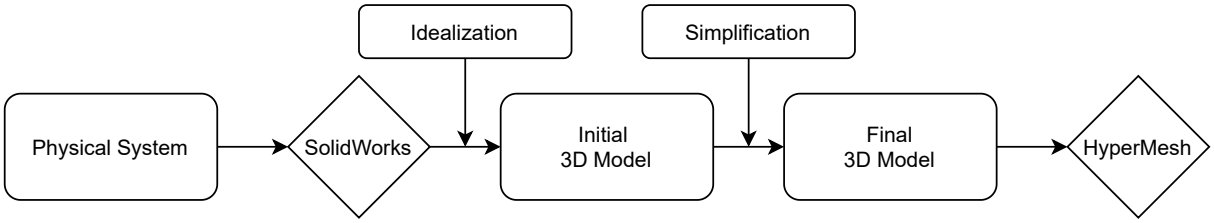

Figure 4.3: SolidWorks approach diagram.

When developing a SolidWorks design, three categories are available. These are inherent to three different types of SolidWorks files: parts (e.g., Figure 4.4), assemblies (Figure 4.5), and drawings. Knowing that components (parts) are the smallest elements that make up an artifact or a mechanical engineering system (assembly), they are the first step in building any model in SolidWorks.

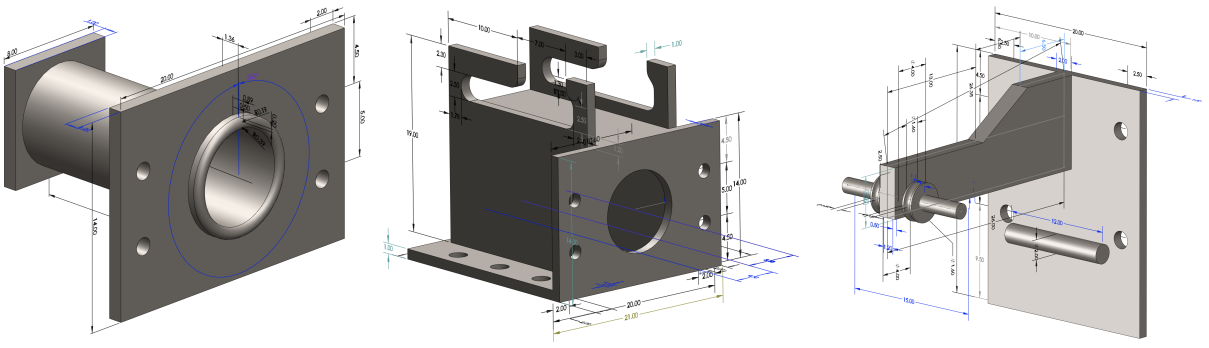

Figure 4.4: Three examples of the parts designed in SolidWorks.

Secondly, after creating all the different part files, it was possible to put them together (Figures 4.5 to 4.7). SolidWorks assemblies are the environment where there are the tools to mix more than one part with mate relationships. This approach allows to see how the different parts interact (it can simulate the movements) and helps to evaluate whether or not the parts fit together correctly.

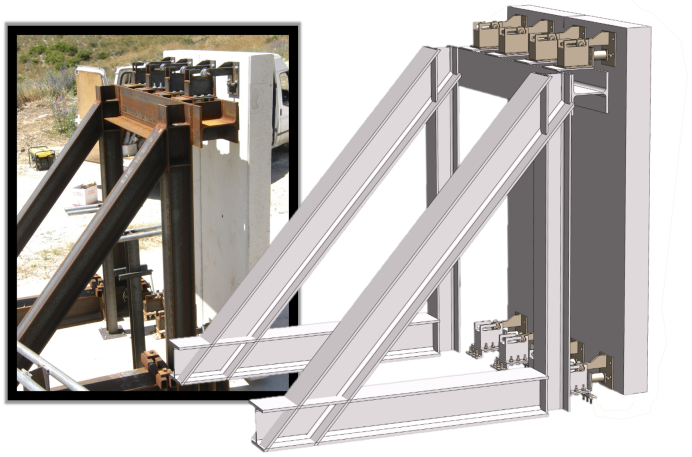

Figure 4.5: Representation of the assembly formed by over ten different parts using SolidWorks.

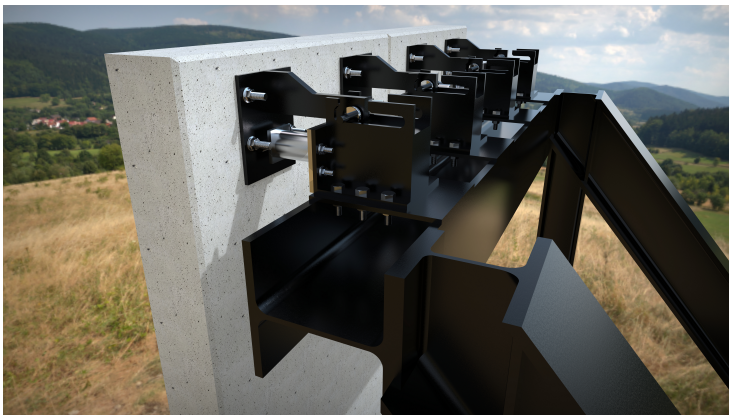

Figure 4.6: Representation of the the assembly render using KeyShot10 software.

Finally, SolidWorks drawing allows to create 2D engineering drawings of parts or assemblies. This step was not necessary. Additionally, although it was possible to define materials and mass properties, this task was done later in LS-Prepost with the remaining properties and variables.

Some struggles were faced with major lessons learned. Among those, a relevant matter is the level of detail. It was a time-consuming mistake during the modelling process to craft the model geometry precisely as in reality.

For the purpose of this analysis, this is not the proper approach. It is essential to understand that the best model, is fast, simple, and has good results. It relates to the “idealization of the model” the second step in the FEM mentioned in Section 4.2. Aspects such as the steel structure being strong and rigid helped simplify the problem. The support frame could be defined as a rigid material, suffering no deformation, which is a cost-efficient approach, that translates into fewer computer resources and faster analysis, but in order to save memory, the support frame was removed.

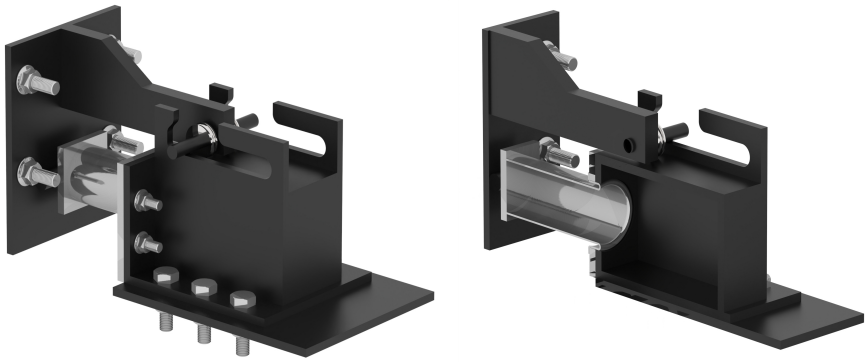

Figure 4.7: Representation of the top connector mechanism using KeyShot10 software.

Another case that was not obvious at first was the bolt's case, which has threads, and those require many resources when meshed. It happens due to the high detail needed in that area, as shown in Figure 4.8. When the contact status between the bolt and the surrounding surface is not relevant, the standard practices are to simplify the bolt, as a simple smooth cylinder plus the nuts [94]. In the end, the goal is a simpler model, however, not at the cost of having bad results.

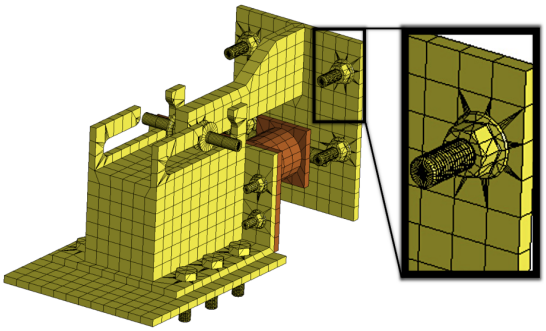

Figure 4.8: Representation of the detail needed on the bolts.

Also, contact between elements needs to be checked. If the geometries do not share nodes and the parts of the model overlap, later on, solving with LS-DYNA, the analysis will give several errors.

4.4.2 HyperMesh Meshing

Within HyperMesh, it was possible to mesh the 3D model created by following the methodology illustrated in Figure 4.9.

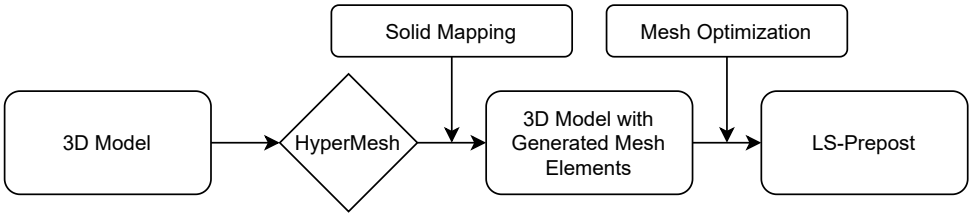

Figure 4.9: HyperMesh approach diagram.

The feature that helped most was the advanced automation tools within HyperMesh, allowing mesh

optimization from a set of quality criteria, such as the “Solid Map”. It allowed to divide the solid into multiple simpler parts and then create a volume mesh from their surfaces. Being further able to locally control the number of nodes to create compatible meshes with different and adaptive mesh densities.

Geometry cleanup and auto meshing, often cited as the most time-consuming aspects of this kind of FEM modeling, were critical aspects in generating a quality mesh that contributed to accurate analysis results, as well as saving a great deal of time. HyperMesh also has CAD interoperability, providing import and export support for the SolidWorks and LS-DYNA files, therefore delivering all the flexibility needed to implement it in the current work.

4.4.3 LS-Prepost

LS-Prepost is the advanced pre-processor and post-processor delivered free with LS-DYNA. The process with LS-Prepost embraces two separate actions, displayed below in Figure 4.10. As a pre-processor, there are essential steps related to all the ongoing definitions and parameters incorporated in the LS-DYNA input file. As a post-processor, it is possible to explore and analyze results in several possibilities, such as visual animation, fringe plotting, data history plotting, among others [95].

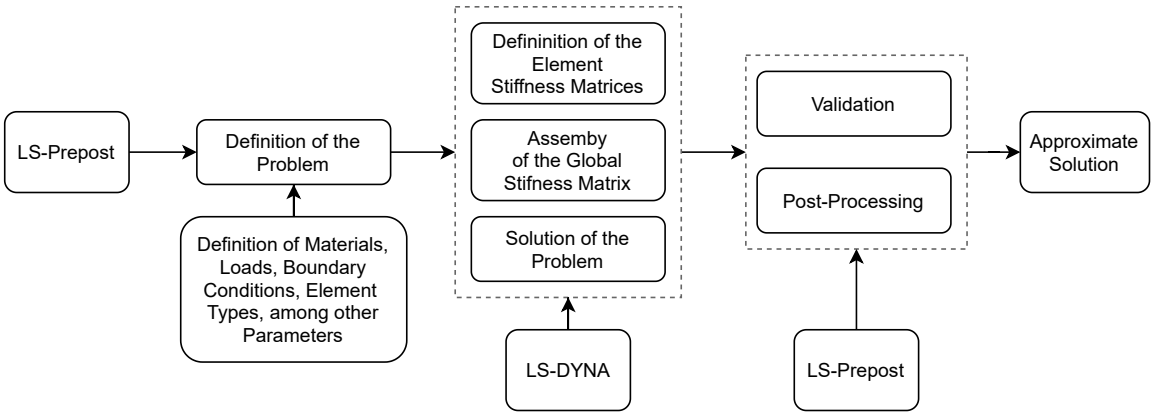

Figure 4.10: LS-Prepost and LS-DYNA approach diagram.

4.4.4 LS-DYNA

LS-DYNA is the solver used, based on the FEM, initially called DYNA3D in which primary applications were to analyse bombs dropped by US Air Force Jets [96]. The specific attraction of this software to the industry started with its nonlinear dynamic capabilities.

As a short introduction, LS-DYNA as a solver, uses a card system, called keywords, where variables within the model input file are denoted by classifications (e.g., *PART, *MAT, *LOAD). Some examples can be found in Appendix B. All the input files are in simple ASCII format and thus can be prepared using any text editor [97].

All simulations were performed using a Workstation with Windows 64-bit running on an AMD Opteron Hexadeca-core (16 Core) 2.50 GHz Processor with 256 GB of memory. The runtime of all models varied between 2.1 hours to 19 days and 4 hours, for a termination time between 0.009 seconds to 0.1 seconds.

4.5 Model Characterization

4.5.1 Material Calibration

Reinforced Concrete Slab Modeling

Concrete, a brittle material which resistance and damage behaviour are strongly influenced by loading rate, is used in the slab of the protective system. Its full-scale structural response test data is costly and difficult to obtain for these highly dynamic loads much due to the equipment required. Concrete is highly strain-rate dependent, and any material model should incorporate these nonlinear characteristics. However, due to concrete characteristics, dynamic experiments that determine these parameters are much more complicated and expensive than the static load test. Therefore, data relevant to the dynamic experiments are limited in the literature [98, 99].

Consequently, responses predicted by numerical analyses have been important resources for academics and structural engineers to determine the behaviors of reinforced concrete structures submitted to dynamic loads (e.g., impacts and blast loads). Although experiments for relevant loading rates and pressures reveal that concrete (and steel, from the reinforcement) exhibit complex nonlinear behavior that is difficult to capture in a single constitutive model, the most basic concrete behaviors should be captured [98, 99].

LS-DYNA Constitutive Concrete Models

LS-DYNA offers several constitutive material models to simulate the structural behavior of reinforced concrete. Individually they have their benefits and limitations, being the three popular ones in terms of performance, MAT072R3, MAT084, and MAT159 [98–100].

Considering the available literature and through self-experimentation, results reproduced favored the Continuous Surface Cap Model (CSCM). In the context of blast and dynamic analysis, studies described it as a reliable model when compared to experimental values [99, 101, 102]. This constitutive model is a concrete material option developed in the United States of America for road safety. Sponsored by the department of transportation to predict the dynamic performance, both elastic deformation and concrete failure [98, 103]. Even though the model was developed and evaluated for roadside safety applications, it should also apply to many dynamic problems [103].

One relevant capacity is the automatic generation of all the parameters, which becomes advantageous. The CSC model (MAT159) can model damage-based softening, confinement effect, strain-rate effect, among others. A comprehensive model review and validation application of this model can be found in references [98, 99, 103]. One additional advantage is the fact that it is significantly faster time than the alternatives.

Reinforcement and Connector Modeling

As with the concrete material models, there are several available in LS-DYNA, which allows users to define the property of steel materials and model their behavior accurately. The material models used for

the steel parts were Plastic Kinematic (MAT003) and Rigid (MAT020).

LS-DYNA Constitutive Plastic Kinematic Material

The Plastic Kinematic material model (MAT_003) was formulated by Krieg and Key [97]. It is a cost-effective model suited to model the isotropic and kinematic hardening plasticity with the option of including rate effects [98]. Also, it is available for beam, shell, and solid elements. This material was applied in reinforcement, partly on the support structure of the connector and finally on the inverted cylinder. The thin-walled component of the connector, the inverted cylinder, is a crucial component in which deformation mode and the overall crash behavior may change if the strain-rate effects are not incorporated. Therefore, being a highly dynamic problem, it is vital to consider the strain-rate effects. Consequently, the Cowper Symonds model (Equation (4.1)) was used to take into account the strain-rate effect under blast loading, which scales the yield stress by a strain-rate dependent factor:

$$\sigma_y = DIF \cdot \sigma_o = \left[1 + \left(\frac{\dot{\varepsilon}}{C}\right)^{\frac{1}{P}}\right] \cdot \sigma_o \tag{4.1}$$

Where DIF, Dynamic Increase Factor, is the strain-rate dependent factor, $\dot{\varepsilon}$ is the strain-rate, σ_o the initial yield stress, C and P are the strain-rate parameters for the Cowper-Symonds model [97].

LS-DYNA Constitutive Rigid Material

Approximating a deformable body as rigid is a preferred modeling technique in many real-world applications. The Rigid material model (MAT_020) does precisely that. Parts defined with this material are considered to belong to a rigid body. It is only used on one support component, represented in yellow in Figure 4.11 below, for the experimental load, due to the lack of registered deformations.

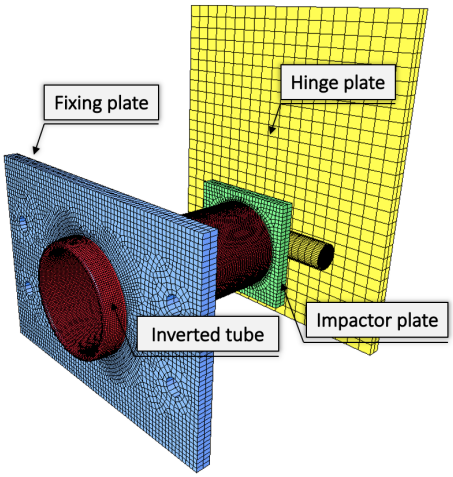

Figure 4.11: Representation of the input model parts of the connector. The yellow part is, in some analyses, considered as a rigid material.

Rigid elements are bypassed in the element processing (CPU saving), and no storage is allocated for storing history variables (memory saving); consequently, the rigid material type is cost-efficient. In

practice, rigid parts do not increase the run time. They only slightly increase the file size.

4.5.2 Optimization and Simplification

Due to the high cost of this analysis, every effort was put in place to simplify and improve its cost-efficiency. When considering the model, geometry simplification was a possible improvement due to the primary component of the connector being symmetric. Most initial analyses used this simplification. It was possible to go beyond the symmetry used (one-quarter of the model). However, having less than one-quarter of the model would be less desirable, mainly due to the loss of perception. Considering the entire model, the simulation could be done on only one concrete slab instead of two. LS-Prepost post-processing has a reflection method, which allows to create the complete model afterward.

Another simplification is the detonation time offset, which does not consider the time that the wave takes to arrive at the target. Avoiding the waste of computational time waiting for the blast wave to hit the structure might sound redundant. However, considerable cost savings can be made by offsetting the time in which the charge is detonated.

One similar simplification is the *DEFORMABLE_TO_RIGID keyword. This will make the connectors rigid for a controlled period. This means that they do not use processing power during that period, speeding up the analysis.

Additionally, simplification is the choice of the constitutive materials. Considering all the materials available, the models chosen are not the fastest. However, taken into consideration the most popular options performance-wise in blast events, for quality results, these are highly cost-effective for both materials, reinforced concrete, and steel. As mentioned already, when possible rigid materials were considered.

In the end, there was one critical improvement. Until now, solid elements have been used for the inverted cylinder. Instead, shell elements were used. Due to the high detail needed in this part, its mesh was very refined. A major part of the processing power, between 56.3% to 76.9%, would be linked to the contacts between each element and element processing only. The change to shell elements saved a lot of computational solve time and improved numerical results.

Blast testing

The principle adopted during analysis was to reason from first principles (simple to complex) and not only by analogy. With this approach, if a mistake happened, it would be easier to identify.

Therefore, every study was done isolated, at the start. As an example, to study the panel, instead of having connectors in their location boundary conditions (SPC_SET) were used, as shown in Figure 4.12.

4.5.3 Element Types

Every element is made up of nodes, which connect the ends of the elements. These nodes are also used to describe the total degrees of freedom of the element, as shown in Figure 4.13. For example,

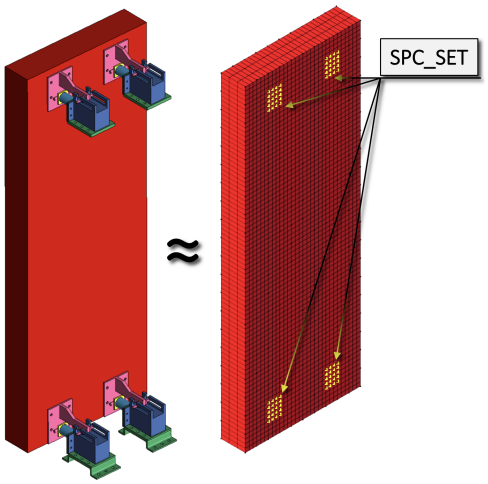

Figure 4.12: Representation of the initial approach, when analysing the panel.

in a triangular-shaped element, there are three nodes represented by edges. In a 2D analysis, that corresponds to six degrees of freedom, while in a 3D analysis, it corresponds to nine degrees of freedom.

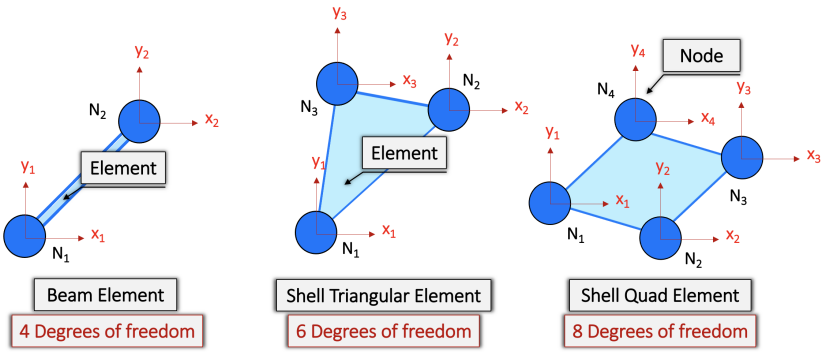

Figure 4.13: An illustration of different elements, respective nodes and degrees of freedom.

Beyond solid elements, beam and shell elements also play an important role in numerical analysis. Shell elements, for instance, are used to model structures and components that are thin relative to their major dimensions [104]. The implementation of shell elements in the inverted cylinder was based on the principle that these elements are used for modeling thin structures. For many applications, far too many solid elements would be needed to obtain a decent solution because solid elements must have a reasonable aspect ratio to be accurate.

LS-DYNA Elements

Defining the elements can be done in different ways, namely section-wise with solid, shell, and beam elements. Furthermore, it can be chosen its formulation and integration rule. The model used solid, beam and shell elements complementing each other for effective and accurate results.

Solid vs. Shell Elements

Solid elements were chosen to model everything, except the inverted cylinder of the connector, which was defined as a shell element. Shell elements are commonly used to simplify and speed up the analysis whenever they are adequate. For instance, in the model, there are elements like the support structure and the concrete target with high thickness. In those parts, it would not be very accurate to consider shell elements.

Solid elements are three-dimensional finite elements that can model solid bodies and structures without any prior geometric simplification. It benefits from the fact that it does not require geometric, constitutive, and loading assumptions; boundary conditions are treated more realistically (compared to shells or beams); finite element mesh looks like the physical system. Nevertheless, it requires higher effort: mesh preparation, CPU time, post-processing, among others; mesh refinement becomes more expensive and often has a poor performance for thin-walled structures [105].

LS-DYNA Elements Formulation

For solid elements, defined by the keyword *ELEMENT_SOLID, LS-DYNA 8-node hexahedral solid elements were used. To define the element formulation and integration rule, the *SECTION_SOLID keyword was used. Its formulation is determined under the ELFORM variable option, particularly ELFORM=1. It denotes that the element is a constant stress solid and uses a one-point integration element. This option is efficient, accurate, and even works for severe deformations. Therefore, it requires less solve time in the analysis. This formulation needs hourglass stabilization. Alternatives, such as ELFORM=2, give a fully integrated brick element formulation similar to the disadvantage of being slower than ELFORM=1. It also becomes more unstable in large deformation applications and, in many situations, is too stiff (might create shear locking effect), especially for poor aspect ratios. Accordingly, ELFORM=1 was used for the concrete solid element's formulation [105].

For shell elements, it is a similar process. It is defined by the keyword *ELEMENT_SHELL and to characterize the element formulation and integration rule. The *SECTION_SHELL keyword was used. It is given by Belytschko-Tsay formulation, under the option ELFORM=2, which also denotes a one-point integration for efficiency reasons. Additionally, it uses a selective reduced integration to avoid hourglass modes [106].

4.5.4 Contacts and Constrains

LS-DYNA has hundreds of different contacts, and it is necessary to define them. They are important to avoid errors, elements penetrations, and even unreliable results (e.g., negative volume elements). In the model NODAL_RIGID_BODY constrains were defined for each EAD, to attach it to the wall. The constrains and contacts used are shown in Figure 4.14 . The several contacts implemented are briefly explained below.

- *CONTACT_AUTOMATIC_SINGLE_SURFACE, for the inverted cylinder shell elements only. It has

the disadvantage of having higher costs than the others. However, it has the main advantage of being more accurate [97];

- *CONTACT_AUTOMATIC_SURFACE_TO_SURFACE, is also recommended in the software manual for solid elements. However, it is necessary to consider the thickness of the modeled shell elements between different parts;
- *CONTACT_INTERIOR enables the software to consider contact between the interior surfaces of the faces of solid elements. This prevents what frequently happens when materials are subjected to high pressure and highly dynamic actions, where solid elements may invert, leading to negative volumes and error terminations.

Regarding Figure 4.14 The two keywords, AUTOMATIC_SURFACE_TO_SURFACE (1) and AUTOMATIC_SURFACE_TO_SURFACE (3) will be particularly important to later draw forces from these surfaces of contact. The first contact gives information on the initial force, while the second, if it surpasses the inverted tube capacity, gives information on force arriving to the protected structure. The difference between both is the absorbed force. To clarify the methodology for the extraction of force values mentioned, three different scenarios are considered:

- The partial deformation of the inverted tube;
- The complete deformation of the inverted tube;
- The complete deformation of the inverted tube with subsequent deformation of the fixed body (connector).

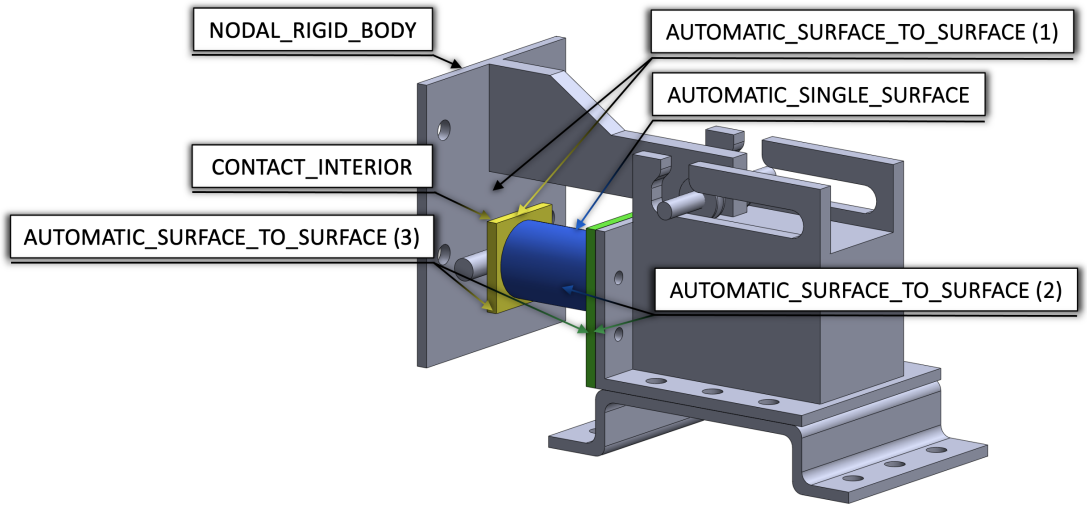

Figure 4.14: Representation of model contacts and the NODAL_RIGID_BODY constrain.

When the first happens, using AUTOMATIC_SURFACE_TO_SURFACE (1) one can determine the initial force value; When complete deformation happens, using AUTOMATIC_SURFACE_TO_SURFACE (1), again one can determine the initial force value. Additionally, one can also determine the force transmitted through the inverted tube to the fixed body, using AUTOMATIC_SURFACE_TO_SURFACE (3), thus in this situations, the difference between the two, will give the absorbed force values.

4.5.5 Deformation Control

Using hexahedral elements has its advantages, mostly the combination of accuracy and runtime efficiency. Their employment usually becomes more economical than other solid element formulations. However, it must be taken into consideration that when using hexahedral elements, there are some possible modes of deformation, such as locking (Figure 4.15) and hourglass (Figure 4.16).

Locking Deformation

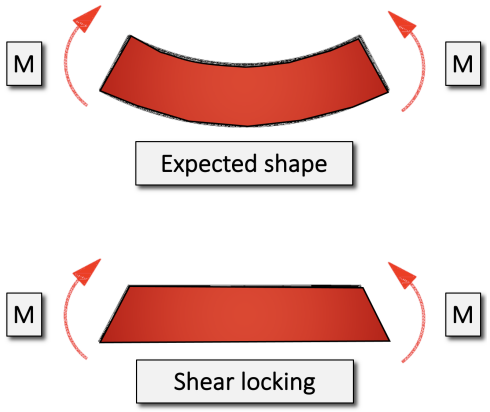

Figure 4.15: Representation of Locking deformation.

It can occur shear locking and volumetric locking. Shear locking develops due to an inability of the element edges to bend. As a result, these elements can be too stiff. The volumetric locking causes unrealistic pressure stresses to develop at the integration points, making the element behave too stiffly.

Hourglass Deformation

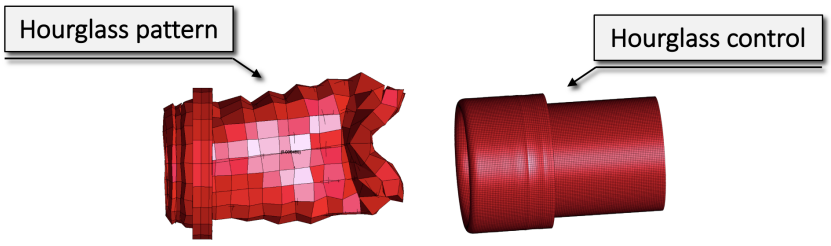

Figure 4.16: Representation of Hourglass deformation.

Due to only having one integration point, this can result in zero-strain deformation modes. The nodal position of the elements deforms without stress being registered, causing the elements to look like a cluster of hourglasses.

Later through the analysis of results, it was concluded that there was the need to implement hourglass control. There are several control type variables (IHQ). The major ones were tested, having both IHQ = 0 and IHQ = 4 given the best results. The former for high loads of TNT gave an error of negative volume. Therefore, the latter, IHQ = 4, was chosen.

4.5.6 Output Database

The output files which contain the results information are defined previously in the database keyword group. It can be done in several formats and options. The options used were:

- ASCII: mainly used for hourglass and energy (GLSTAT and MATSUM). On top of that, it was also used to obtain forces (RCFORC);
- BLSTFOR: to measure the blast pressure. This option produces the blast pressure output (reflected pressure, incident pressure, among others);
- D3PLOT: for complete graphic states output (stresses, strains, energy, velocities, among others);
- D3THDT: for time history data element (stresses, strains, energy, velocities, among others).

The time interval between outputs was chosen precisely based on the first analysis to be as cost-effective as possible. Therefore, values in seconds were 0.0001 for ASCII, BLSTFOR, D3PLOT and D3THDT.

4.5.7 Termination Time

In LS-DYNA, the analysis is stopped at a specified time, called the termination time, which is determined by the keyword *CONTROL_TERMINATION. Termination time greatly influences the analysis runtime. Additionally, because the response of the concrete slab occurs in a very short time, it needs to be precisely defined to be cost-effective and long enough to capture all the pretended information avoiding delaying the analysis and wasting processing resources. Therefore, the analyses were specified to be stopped at 0.009 seconds in both one quarter and full connector models. In the complete system model, it was specified values up to 0.1 seconds. The aim was to be able in each model analysis, to achieve the maximum deformation within this period while simultaneously registering all the needed results.

4.5.8 Mesh quality

Similar to the termination time, mesh quality is also an important parameter that influences runtime significantly. A simple mesh with good quality elements or a refined mesh with bad quality elements can create a slower analysis than expected. Additionally it tends to create distortion of the elements (Figure 4.17), which causes the time step to drop very low and thus increase the runtime, which may contribute to errors.

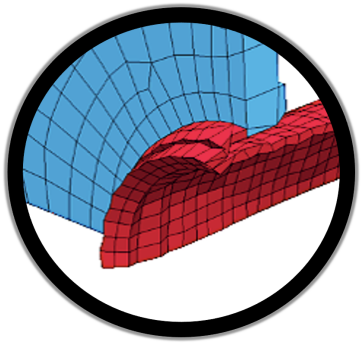

Figure 4.17: Example of a bad quality mesh that generated a long processing runtime, which is illustrated by the distortion of its solid elements.

According to Figure 4.18 examples, I) shows a simple mesh which runtime was high (up to 22 days) and gave bad results. This specific part, the inverted tube, if modeled with solid elements, it would require many elements to avoid distortion, and to have the same results, as a mesh with shell elements. One last detail that also increased the runtime in this specific model, was the non-compatibility between some element nodes. Both II) and III) are good models. They are fast and produced accurate results, being the last one more refined.

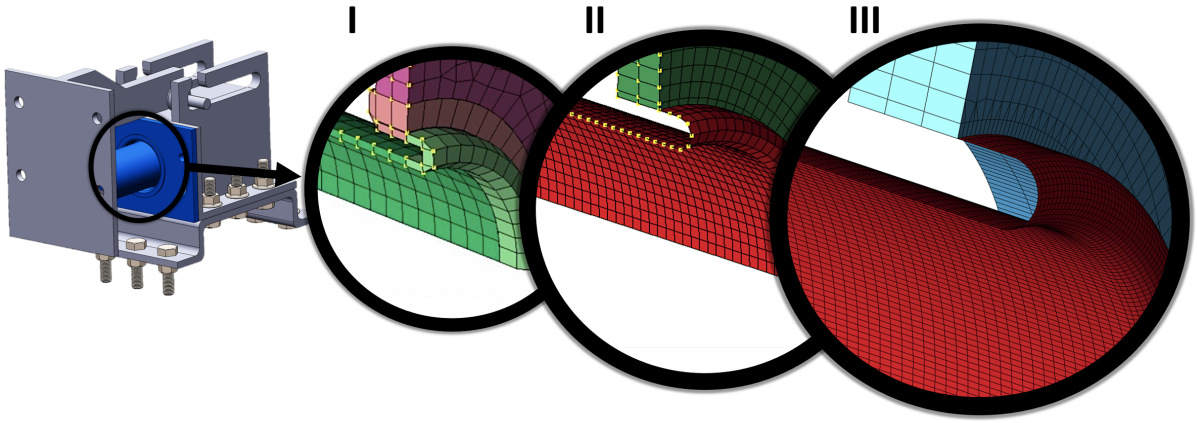

Figure 4.18: Representation of three examples of mesh improvement.

4.5.9 Strain-Rate Effects

This is a highly dynamic problem. Thus, it is important to consider the strain-rate effects. In the steel material chosen (MAT_003), those effects are considered when defining the constitutive materials through Cowper-Symonds parameters. These parameters have been widely studied, and there are several contributions in the available literature, as can be seen in Table 4.1.

Table 4.1: Cowper-Symonds parameters for mild steel.

Publication	C	P
Cowper & Symonds [107]	40.4	5
Abramowicz & Jones [108]	6844	3.91
Abramowicz & Jones [109]	802	3.585
Yu & Jones [110]	1.05E7	8.3
Marais et al. [111]	844	2.207
Jama et al. [112]	844	2.207
Sun & Packer [113]	3023	1.65

4.5.10 Blast Load Alternative Methods

Initial Velocity Generation

Initial Velocity Generation (IVG) is an alternative method that imposes an initial velocity on the selected elements. It is a cost-effective method to create the desired deformation, similar to the one created by the blast, seen in the experimental campaign tests. Initially, arbitrary velocities were used to be able to model the inversion deformation behavior accurately.

Load segment set (LSS) and load blast enhanced (LBE) methods were used to simulate a blast similar to the experimental one and find the velocity imposed onto the connectors. Then the goal was to use that velocity with the IVG method on the models. Nevertheless, this was not the best approach. Surprisingly, both LSS and LBE were less expensive than the IVG. Furthermore, IVG could not reproduce the blast effects realistically. Consequently, alternative methods were explored.

Load Segment Set

Considering blast events, it is possible in this context to use IVG. However, LSS is a more appropriate method, and cost-effective alternative. Nevertheless, its employment is only possible when the blast pressure data from the experiment is available, which was the case.

LSS exerts a predefined uniform pressure all over a specific segment set chosen, which can be in function of time. It was possible to export a pressure curve from the experimental data and use it with this method.

Since this method applies blast pressure data, it does not consider the angle of incidence on the wall. In reality, the higher the impact angle, the higher the reduction of the pressure on the slab. This effect along the span length is not considered with this method, and it plays a remarkable influence on the system's behavior.

To compensate for this effect, the slab was divided into ten horizontal segments, allowing to calculate an average pressure curve for each, considering the influence of the impact angle, as shown in Figure 4.19. A few other authors have used a similar resolution of breaking the area into many segments with a similar approach [28].

Still, velocity values were volatile (variations up to ± 3m/s), and the minimal fluctuation intervals could produce significant deviations. Only by the end of the dissertation, with a validated and calibrated model, and using LBE, it was achievable to calculate an acceptable velocity value. Compared to the previous

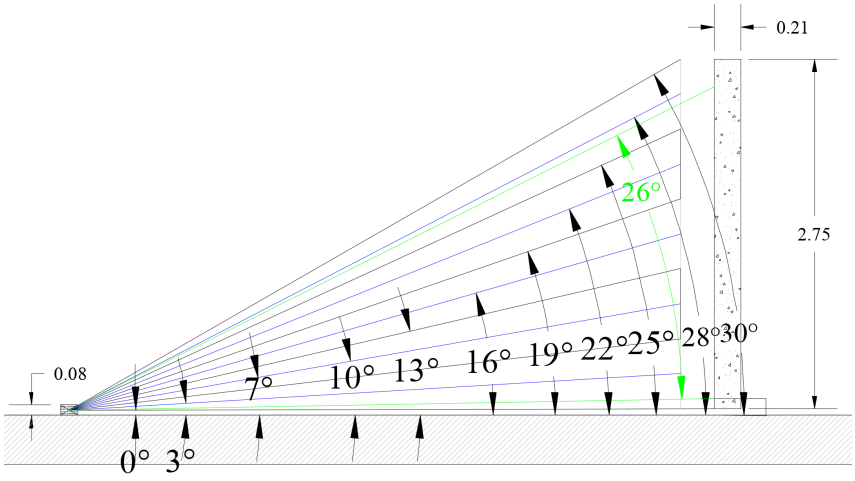

Figure 4.19: Representation of the division of the surface of the slab in ten segments.

method (IVG), the results were more accurate. Regardless, errors were still significant compared to experimental data. Additionally, the output data was limited.

Four major issues were contributing to such inaccuracy: i) It is evident that the best method is one that simulates the complete structure instead of making two separate simulations. The numerical validation and calibration of the model may become more uncertain if done separately; ii) Although the LSS method considers the influence of the impact angle, it does not take into account the fact that on detonation, energy dissipates violently through a spherical shock wave, as can be seen in Figure 4.20; iii) LSS method additionally, considers one average value for each of the ten segments, increasing the simplification, therefore the error, and finally iv) LSS results gave, as mentioned, high variations in velocity, that made it impossible to calibrate the model under the recommended 10% error.

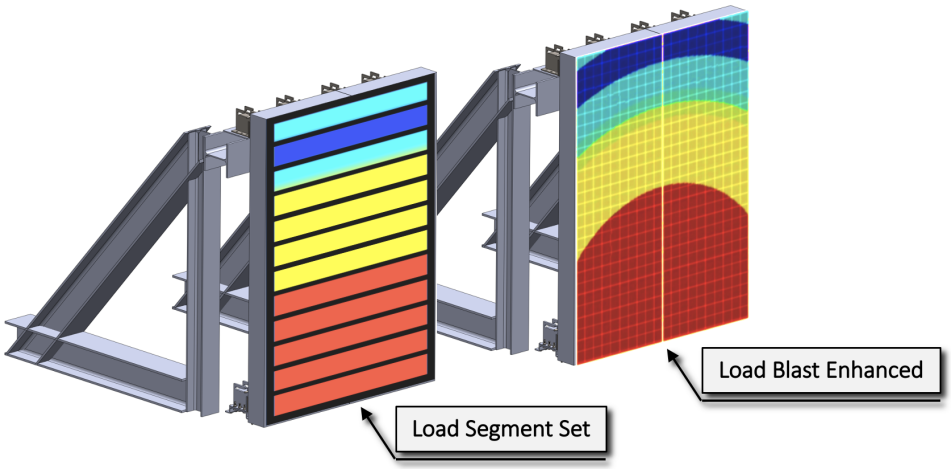

Figure 4.20: Representation of the different blast effects on the panel, considering LSS and LBE methods in the analysis.

4.5.11 Blast Load Methods

LS-DYNA has four major methods to model blast events. Namely Load Blast Enhanced (LBE), Arbitrary Lagrangian-Eulerian (ALE), a hybrid combination of the two methods mentioned (LBE and ALE), and Particle methods. LBE was the method used. It is based on a database of experimental data which provides empirical pressure histories due to conventional chemical explosions. A simplified and proven analysis approach over the expensive ALE method and Particle methods. These methods tend to be used for more complex problems, such as the structural response of a structure, scenarios with multiple wave interactions of multiple explosions, and blast wave reflections with the surrounding environment [114], which in this context did not provide a valid purpose to apply them.

Load Blast Enhanced

This method is not an alternative to blast loading. It is a method specifically designed to model blast events. Its main limitation is that it acts on a clear line of sight, applying a full blast load on the target, even if shadowed by an intervening object. However, this limitation does not impact the present study.

LBE was one of the first methods considered to analyze blast events. However, initially, it was not appropriate to use it. Every explosive has a few different characteristics, being most of them similar to TNT. In this case, the explosive used had some differences. As mentioned in Chapter 3, even when an equivalent TNT mass was determined, it would give different results considering different methods. The significant differences were that Goma-2 ECO had a bigger value of peak pressure than TNT and a shorter duration of positive phase. Additionally, the fact that the model was barely optimized in the beginning culminated with expensive analysis.

Later, there were two major reasons which empowered to use this method. First, the possibility to improve the numerical results by performing a blast load calibration. This enabled to virtually create similar pressure-curve characteristics of the Goma 2 ECO blast. Second, the optimization of the model, as it granted more quality of results in a shorter analysis period.

4.6 Numerical Models

During the numerical study, three types of model geometries have been done. Firstly, the one-quarter of the connector model (initial approach); Secondly the complete connector model (intermediate approach), shown in Figure 4.21. Thirdly, a complete full model of the system (final approach), represented in Figure 4.22.

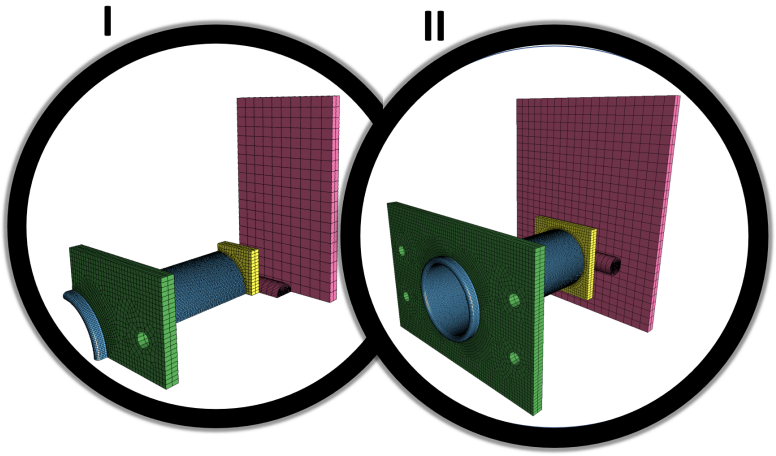

Figure 4.21: Illustration of the one-quarter of connector model (I) and the complete connector model (II).

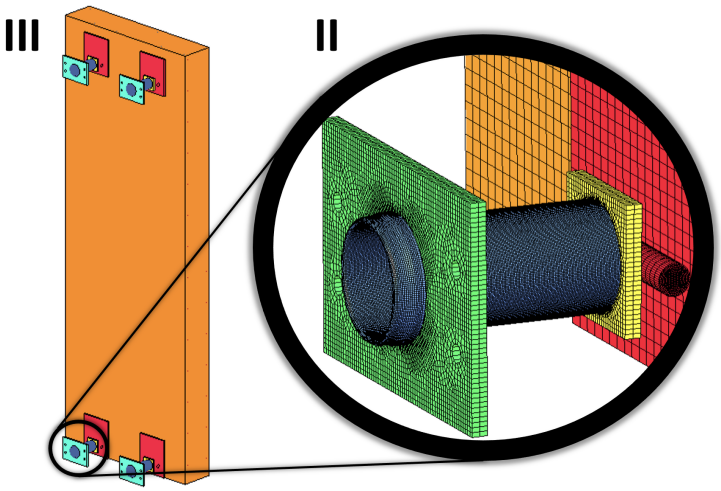

Figure 4.22: Illustration of the full connector model (II) within the full numerical model (III).

4.6.1 One-quarter of the Connector Model

To simulate boundary conditions, SPC_SET definitions were assigned, as shown in Figure 4.23. Symmetry boundary conditions (SPC_SET_1), were achieved restricting specific translations and rotations. It defines a mirror surface and should only be used if the pretended solution is mirrored along that surface. By using such boundary conditions, the domain was reduced to one-quarter, reducing significantly computer resources and processing time. These symmetry conditions were applied on both, xz-plane and yz-plane.

Boundary conditions were additionally used on the fixing plate nodes of the connector (green part) to fix the model (SPC_SET_2). It simulates the rigid connector attached to those nodes. Lastly, another boundary condition (SPC_SET_3) was used on the hinge plate (purple part) to enable it to impact the connector in an ideal way (horizontally).

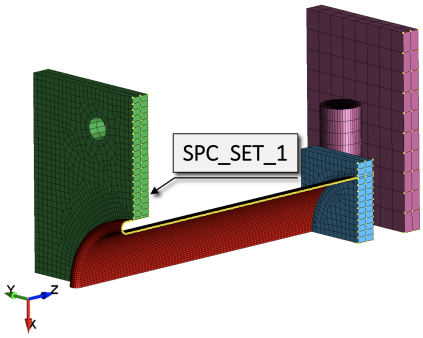

Figure 4.23: Representation of one-quarter of connector, with a restriction of y translation (δ_y = 0) and rotations x and z (Θ_x = Θ_z = 0) applied on the highlighted yellow nodes to simulate symmetry boundary conditions on the xz-plane.

4.6.2 Full Connector Model

The full connector model, has a lot of similarities to the one-quarter model. SPC_SET_1 is the boundary condition that changes because no longer is required symmetry boundary conditions, only having SPC_SET_2 and SPC_SET_3, as shown in Figure 4.24.

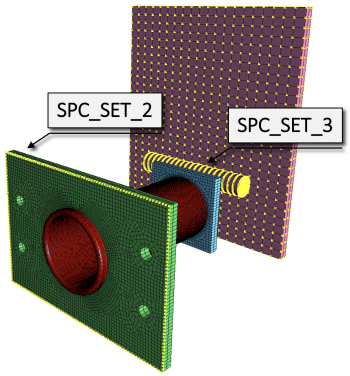

Figure 4.24: Representation of the full connector model and its restricted nodes, associated to the respective boundary defined condition.

4.6.3 Full Numerical Model

In order to understand the boundary conditions used in this model, first one must consider some aspects. The numerical and experimental images (Figure 4.26), shows how the slit where the rollers slide along was deformed by the pin of the rollers and the connection pullout. It also represents the pendulum effect described in Chapter 3.

The main goal with finite element analysis is to reproduce the experimental reality numerically as closely as possible to calibrate the model and validate the results. Initially, three systems of models were built. One model where bottom connections had its displacements restricted (Full_Restricted), like a pinned support. Another with the same restrictions, except for the surface where the plate had been ripped out, where there was no displacement restriction. Instead, rotations were restricted (No_Restricted), as illustrated on Figure 4.25.

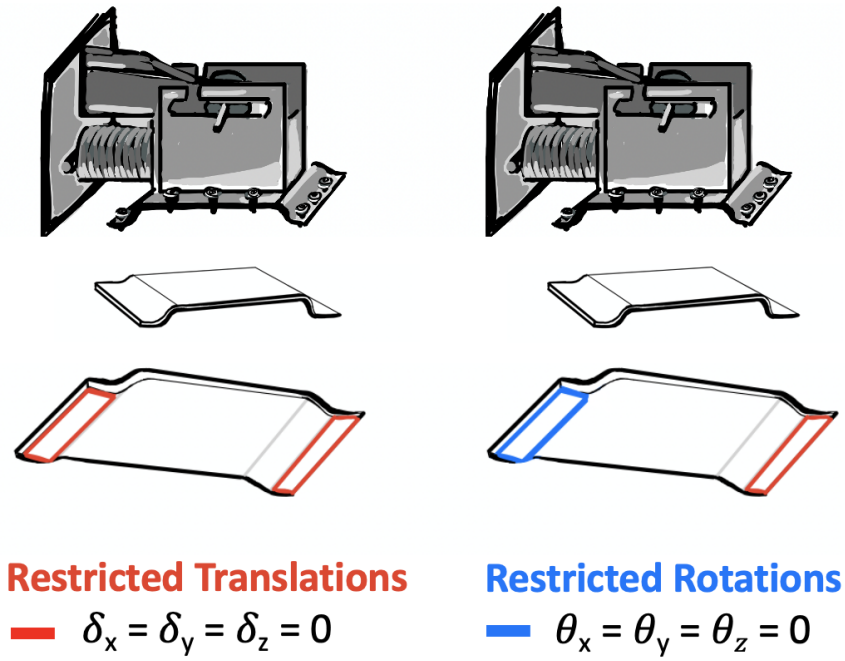

Figure 4.25: Illustration of the Full_Restricted System (left side), restricting displacements in both connector faces and the No_Restricted System (right side), restricting only the displacements in one face.

In the end, what had been observed experimentally would be in between these two situations. Therefore, a third model was created with half configurations from both systems. The bottom connectors at slab ends were Full_Restricted, and the bottom connectors in the interior were No_Restricted, having what was called Semi_Restricted System.

One of the first working models, of the whole system, is displayed in Figure 4.26. It followed the described approach. However, it had no optimization, a 4 mm mesh with only solid elements. It did not consider strain-rate parameters. Materials parameters were not calibrated. The steel yield stress, was even wrongly defined in the inverted cylinder (one magnitude below), which explains the buckling. The deviation average was 32 %, however the most important, the behaviour, was similar to the experimental data.

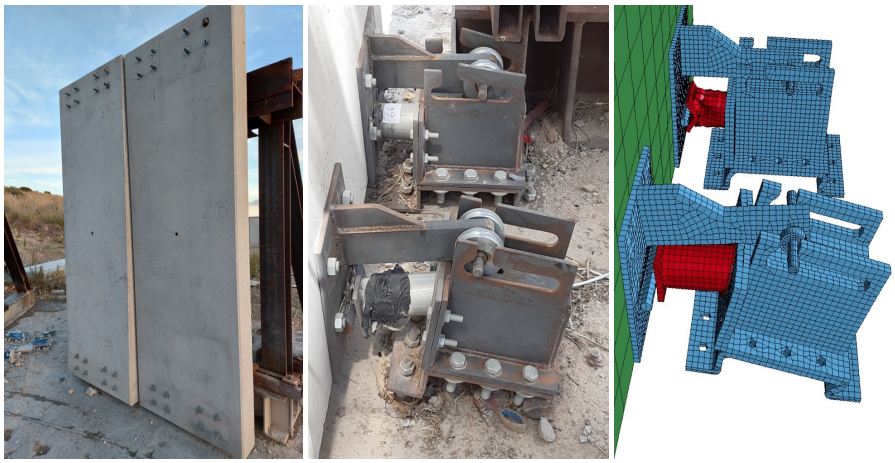

Figure 4.26: Representation of the experimental setup versus the first generation of models (May, 2021) created with Semi_Restricted_System [27].

Nevertheless, there are some aspects that hinder the development of this approach. In this context, there was no information on the connection between steel and concrete. Only having those details, of interface and connections, it would be possible to model the bolts and the ground. Additionally, the connection of the bolt to the ground is not the focus of the present dissertation. The purpose of the study is to evaluate the effectiveness of the inverted cylinder design in absorption the blast loads. Concluding, it is not the proper approach to replicate the rotation effect together with the pullout of bottom connectors. Thus, it could be a mistake to consider unreasonable boundary conditions to replicate precisely what happened experimentally. That would be almost as deceiving the results, and it would probably only work for one case scenario. Therefore, the initial methodology was adjusted.

It began with the simplest model, the one considered as the ideal response. The support connection to the ground was also considered perfectly rigid, restricting every displacement on those surfaces. Therefore, the slab would not have connectors ripped out and would suffer fewer rotation effects.

4.7 Calibration and Validation Methods

4.7.1 Blast Load Calibration

Considering the concept of the scaling laws, explained in Chapter 2, it is possible to have two charges of the same explosive, that have different weights and are set at the same scaled distance, producing similar blast waves at the point of interest. Through Figure 4.27, one can observe the differences in characteristics between the explosive used (curve in blue) and its TNT equivalent (curve in red). It is fairly clear that considering the equivalent charge in TNT, one cannot portray the same effect of the experimental pressure curve (curve in blue), which is descending faster.

Blast load calibration is the process of numerically changing TNT mass and distance to achieve the same experimental effects, particularly the same pressure curve slope. The changes, however, must be coherent with the scaling laws. Therefore, different mass and standoff distances combinations were tried to see which one gives the “best” curve.

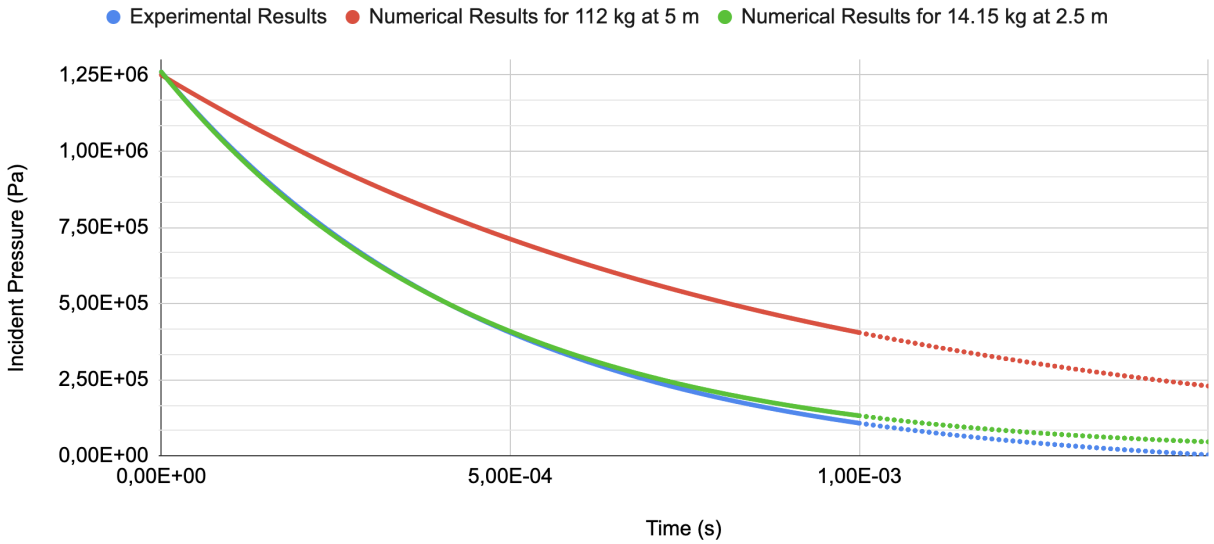

Figure 4.27: Examples of pressure curves used to iteratively calibrate the experimental curve.

Iteratively, it was possible to calibrate the results. It is noticeable, how the numerical calibrated pressure curve (curve in green), gives a better match to the experimental pressure data. To be more exact, it gives an error of 2.72 % concerning incident pressure versus the 100.84 % error from the TNT equivalent (curve in red).

4.7.2 Benchmarking

After creating the different parts and assembling them in SolidWorks, as well as refining and simplifying the models, the modeling phase was completed. Following the meshing process, the 3D solid was ready to be imported and later solved with LS-DYNA. However, the progress at this stage was dependent first on mastering LS-DYNA software.

This stage started with simple and verifiable analysis, considering elastic materials, uniform loads, simple boundary conditions, and geometry. Through benchmarking, learning the software by practicing with progressively harder examples, which problems and solutions were available, was crucial to virtually understand how to consider blast loads on different constitutive materials or even variables such as strain-rate, among others necessary aspects.

4.7.3 Mesh Convergence

One issue that is usually overlooked and affects accuracy is mesh convergence or mesh sensitivity study. It is often used in finite element analysis to ensure that computed results converge to the actual solution, whether the problem at hand is linear or nonlinear, that the results are accurate enough, and mesh quality does not significantly influence the final solution [92].

Good practices recommend that at least three points need to be considered [91]. In practice, it all starts from a relatively coarse mesh, which solution will not be wrong but will be highly inaccurate. The finer the mesh, the better the convergence of the numerical solution. However, finer meshes tend to

be expensive in computing resources, so an equilibrium must be met, a solution that is both close to the “true solution” and affordable [92]. The principle is to solve the problem on a progressively refined mesh that simultaneously will get increasingly more accurate solutions and longer computation runtime. While doing this, the percentual variation of the current solution from the previous, coarse-mesh-solution is calculated. The process is repeated until the current mesh-solution varies by less than 5 % from the previous coarse-mesh-solution. If that happens, the result has converged, and the “bliss point” was achieved, which entails that results are more reliable [92, 115].

In the beginning of the process, the first analysis focused on the simplest model, the one-quarter of the connector (inverted tube with both adjacent plates, as shown previously), due to the existing symmetry reducing the long analysis periods. Those first versions of the model were not optimized, and were built only using solid and beam elements. Reasonable solutions would take up to 768 hours to analyze, as observed in Figure 4.28.

Errors were found, and improvements were made. LBE was the method used since it was faster and more appropriate than the IVG and LSS methods. After several simulations, performing a mesh convergence study, the reasonable solutions would now take at least 14,9 hours, as shown in Table 4.2.

It is important to reinforce that this first part of the study does not calibrate and validate the results. Instead, it was used to replicate the desired deformation behavior and then perform a mesh convergence study to find the optimal mesh configuration. The calibration and validation of the numerical model were only achieved later with the simulation of the entire numerical model.

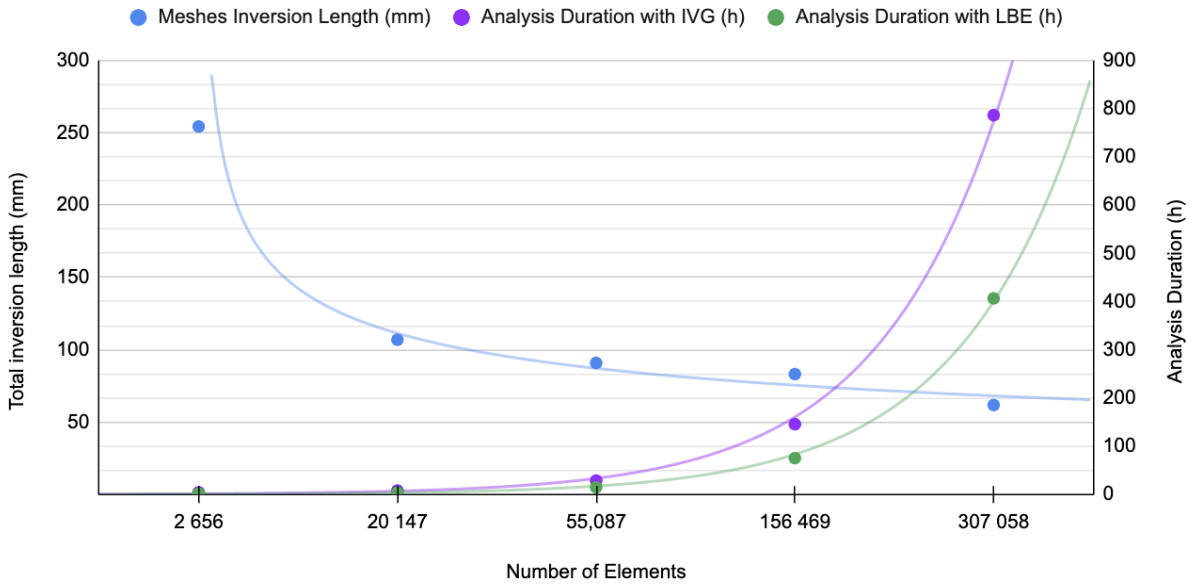

Figure 4.28: Mesh convergence study with solid and beam elements only. Mesh densities and corresponding number of elements: 2 mm (2 656 elements), 1 mm (20 147 elements), 0.75 mm (55 087 elements), 0.5 mm (156 469 elements) and 0.4 mm (307 058 elements) respectively.

Late analyses of the model, with a full connector or the full system, were only possible due to the mesh improvements, mainly the change of solid elements for shell elements in the inverted cylinder. The chosen mesh from the convergence study, would now take around 2,1 hours, an improvement of approximately 710 % in terms of speed compared to the previous 14.9 hours model, illustrated in

Table 4.3 and Figure 4.29.

Table 4.2: Mesh convergence of the last version of the model. Only solid and beam elements.

Meshes $[mm]$	Final Length $[m]$	Relative Error $[\%]$	Nº nodes	Nº Elements	Analysis Duration $[h]$
2.00	0.075	-	5 580	2 656	2.26
1.00	0.111	33.091	30 795	20 147	4.12
0.75	0.115	3.467	84 096	55 087	14.86
0.50	0.117	1.648	197 652	156 469	75.25
0.40	0.123	4.357	371 158	307 058	406.51

Table 4.3: Mesh convergence of the last version of the model. Solid, beam and shell elements.

Meshes $[mm]$	Final Length $[m]$	Relative Error $[\%]$	Nº nodes	Nº Elements	Analysis Duration $[h]$
2.00	0.123	-	9 767	7 613	0.269
1.00	0.125	1.760	19 325	14 510	2.124
0.75	0.126	0.849	27 413	23 562	3.159
0.50	0.126	0.295	65 490	55 014	31.200
0.40	0.129	1.879	250 698	237 857	186.067

Using solid elements without symmetry simplifications does not require geometric, loading, and boundaries assumptions. Additionally, overall conditions are treated more realistically. Therefore, specific analyses like the influence of eccentricities had now the best conditions to be studied.

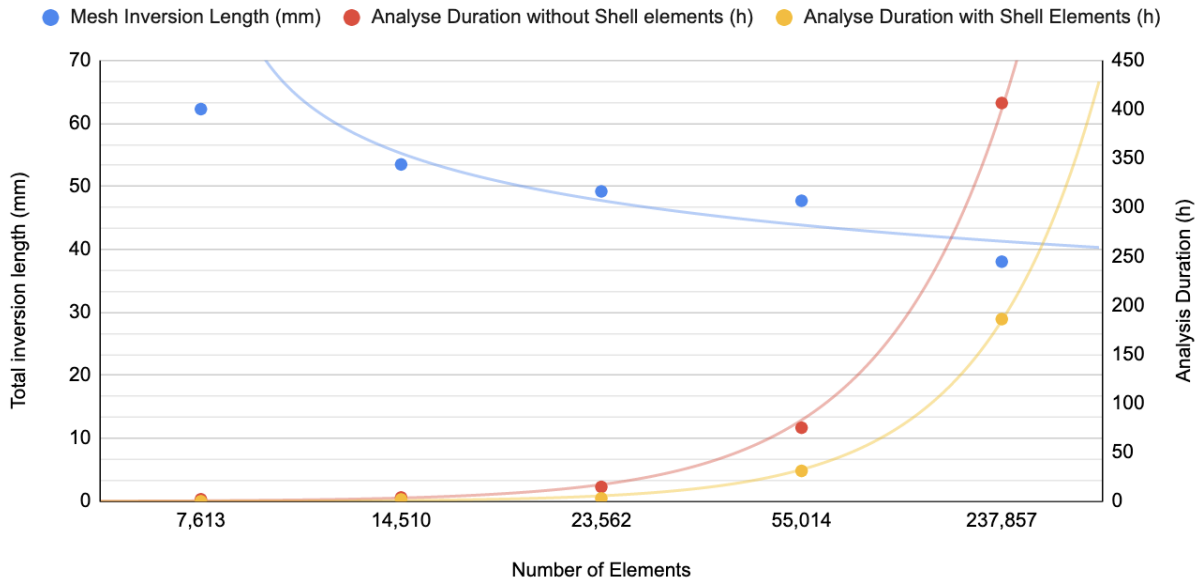

Figure 4.29: Mesh convergence of both models, with and without shell elements. Mesh densities and corresponding number of elements: 2 mm (2 656 elements), 1 mm (20 147 elements), 0.75 mm (55 087 elements), 0.5 mm (156 469 elements) and 0.4 mm (307 058 elements) respectively.

4.7.4 Experimentation

Having done the mesh convergence and benchmarking, one additional way to make results more trustworthy was to perform experimentation. This additional step, consists in the development of the numerical model until its analyses start to produce similar results to the experimental data.

In order to represent the correct visual deformation behavior, according to the experimental campaign tests, the entire protective system was modeled (slab and connectors). Knowing that in post-processing, it would be possible to replicate the model, it was only built half of the system, precisely a reinforced concrete slab with four connectors, as shown in Figure 4.30, which in practical terms is one slab with four EADs.

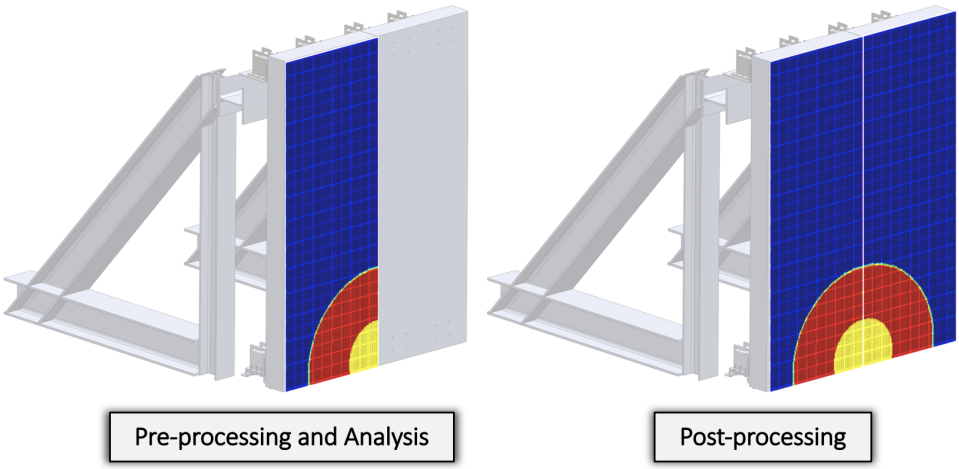

Figure 4.30: Scheme of the symmetry simplification used on the entire model.

Moreover, being a highly dynamic problem, it was vital once again to consider strain-rate effects. To take this effect into account, all strain-rate parameters presented in Chapter 4, Table 4.1, were tested (Table 4.4).

The process seeks to find the parameters that best fit the actual behavior of the system, namely the total inversion. The dispersion in terms of values, obtained by comparison with experimental results, allows to compare the different parameters and choose the one that offers the most accurate results, as well as confirming if the error value associated is acceptable.

Table 4.4: Full System results for the equivalent and calibrated load (explained in Chapter 4).

SRC ; SRP	Publications	Total Inversion $[mm]$	Deviation $[\%]$	Velocity $[m/s]$	Initial Kinetic Energy $[J]$	Internal Energy $[J]$
40.4 ; 5	Cowper & Symonds (1957)	28.4553	67.29	2.23	4 179.57	4 502.13
6844 ; 3.91	Abramowicz & Jones (1984)	71.2649	18.09	2.32	4 499.11	5 142.68
802 ; 3.585	Abramowicz & Jones (1986)	55.8398	35.82	2.29	4 405.15	5 004.65
1.05e7 ; 8.3	Yu & Jonesj (1991)	75.9581	12.69	2.33	4 551.19	5 158.38
844 ; 2.207	Marais et al. (2004), Jama et al. (2009)	64.0771	26.35	2.30	4 427.09	5 085.02
3023 ; 1.65	Sun & Packer (2014)	88.5540	1.79	2.34	4 590.76	5 221.53

There are two values for the Sun & Parcker strain-rate parameters, due to one of them having a correction (COR)[1] for higher loads of TNT, with an associated deviation was 6.32 %, that otherwise would give an error in the analysis. From the remaining results, these strain-rate parameters produced the results with the lowest deviation, which is under the recommended range (10 %). Therefore, the calibration and validation of results has been achieved.

[1]For higher loads, the model starts to give an error on the integration of the elements. As a solution, hourglass control type variable (IHQ), is set to IHQ=4. Additionally another contact is added (*CONTACT_INTERIOR). Together both solve the problem allowing to run the analysis for higher loads of explosive, at the expense of a slight increase of accuracy.

It is important to emphasize that although the results are close, they do not represent exactly what happened in reality. The values are compared based on the total inversion length. As mentioned in chapter 4, Section 4.6.3, the model was based on the ideal response, by considering the support connection to the ground as perfectly rigid, restricting every displacement on those surfaces. Furthermore, friction on the upper connectors was not considered.

Nevertheless, considering the two valid results within experimental data one can obtain the following table Table 4.5 while numerically, it was achieved Table 4.6. From these results, it can be seen a clear difference from both. A common pattern is the tendency for bottom connectors to deform more than those at the top. On top of that, even in the numerical ideal response, the pendulum effect is still manifested although less noticeable.

Table 4.5: Data results on shortening and rotation of the inversion tubes measured after testing campaign [27].

Sample	Location	$L_{initial}$ $[mm]$	L_{final} $[mm]$	Rotation $[^\circ]$	Shortening $[mm]$	Total Inversion Length $[mm]$
#2	BL	139	97	3	42	84
	BR	137	97	3	40	
	TL	140	138	3	2	
	TR	141	141	3	0	
#3	BL	139	100	2	39	90
	BR	138	93	3.5	45	
	TL	139	135	3	4	
	TR	138	136	2	2	

Table 4.6: Data results on shortening and rotation of the inversion tubes extracted from the numerical analysis.

Sample	Location	$L_{initial}$ $[mm]$	L_{final} $[mm]$	Rotation $[^\circ]$	Shortening $[mm]$	Total Inversion Length $[mm]$
#N	BL	138.1	114.5	2.4	23.6	88.5
	BR	138.1	114.6	2.5	23.5	
	TL	138.1	117.4	2.4	20.7	
	TR	138.1	117.4	2.5	20.7	

One additional insight, is the impact of velocity in the error percentage of total inversion. As mentioned, the LSS method was not considered and one of the reasons was for its volatile oscillation in velocity values (up to ± 3 m/s), since the slightest change can create big errors. Considering for example, Sun & Packer (v = 2.3415 m/s) with Abramowicz & Jones (v = 2.29 m/s), one can observe that the velocity difference is 0.0515 m/s, however the relative error in deformation is 34 %.

The further analysis that will be presented in chapter 5, were done taken into consideration Sun & Parcker strain-rate parameters (SRC = 3023; SRP = 1.65) [113].

Chapter 5

Numerical Analysis

According to Figure 5.1, at this point, the 3D model has been created and divided in elements. The model, together with its characteristics have been through calibration methods. Once calibration and validation was achieved, which is a good indication that it is correct, the study was complemented with simulation. Therefore, in this chapter, analyses will be performed, to study solutions and ideas that haven't been tested experimentally. It starts from a micro analysis that goes through some of its defined parameters, to its parts and details up to a macro analysis of the entire protective system, verifying its effects and influence. Lastly, conclusions were drawn.

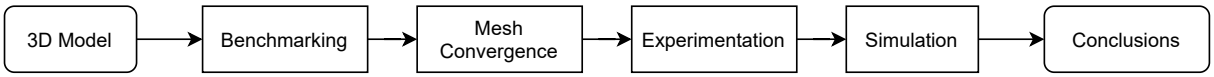

Figure 5.1: Diagram of the final numerical analysis stages.

It should be noted that the values obtained in the various simulations involving force values should be interpreted in a relative manner between them and not in an absolute form.

5.1 Simulation 1: Sensitivity analysis of Young Modulus variation

Young's modulus or elastic modulus is a mechanical property of linear elastic solid materials. Young's modulus defines the relationship between stress and strain in a solid material, and is given by Equation (5.1):

$$\sigma[MPa] = E \cdot \varepsilon \tag{5.1}$$

where E is the Young's modulus of the material;
σ is the stress;
ε is the strain.

In general, all solid materials are not linear elastic, especially when they are subjected to high levels of deformation. Furthermore blast analysis is highly nonlinear. The stresses and strains of materials exhibit nonlinear behavior such as plasticity or failure. Therefore, this propriety should not have much in-

fluence on the results. The purpose of this study was to confirm this hypothesis on its energy-absorption performance.

From the obtained results, represented in Table 5.1, it can be stated that with higher values of young's modulus:

Table 5.1: Table of Young's Modulus study.

Young Modulus $[GPa]$	Final length $[m]$	Total Inversion $[mm]$	Velocity $[m/s]$	Max Kinetic Energy $[J]$	Internal Energy $[J]$	Resultant Force Variation $[\%]$
150	0.1180	80.59	11.21	175.33	313.23	- 2.69
200	0.1179	80.78	11.17	174.23	311.95	0.00
250	0.1178	81.08	11.15	173.51	311.26	0.28
300	0.1178	81.11	11.13	172.94	310.58	- 0.07
350	0.1179	80.80	11.12	172.47	310.08	- 0.14
400	0.1179	80.71	11.10	172.09	309.62	0.25

- Total inversion length is almost the same. There is a very small oscillation of approximately 0.5 mm between the two outlying values.
- Velocity decreases very slightly too (around 0.1 m/s), which probably is related to the material becoming increasingly more rigid. It is coherent with initial kinetic energy that also has a small reduction;
- Internal energy also has a small decrease of values. Which entails that with higher values of young's modulus, less energy gets absorbed;
- Resultant force increases initially from 150 GPa to 200 GPa and between 200 GPa and 400 GPa values oscillate lightly between each other.

As expected, considering all the parameters involved, young's modulus does not influence significantly the performance behavior of the EADs.

5.2 Simulation 2: Hinge influence

One interesting feature of this solution is the hinge element, welded in the plate attached to the wall (Figure 5.2). It was expected that this element would prevent the loss of performance of the system. The purpose of this analysis is to verify this hypothesis and understand how its influence affects results.

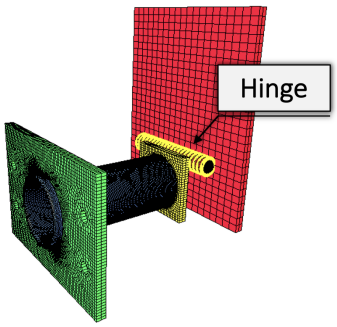

Figure 5.2: Representation of the hinge element.

One must remember that when the system is installed, there is some tendency to have some level of eccentricity as already mentioned. To analyse its influence, instead of using the hinge element, a steel plate with the same thickness was used. Nevertheless such change is also expected to have a good behavior. Two scenarios were studied: i) the most common, where the wall may be slightly inclined and ii) the one with perfect conditions, where the plate may be in full contact with the impactor plate. The first situation was analysed, considering both cases of rotation, as illustrated by Figure 5.3:

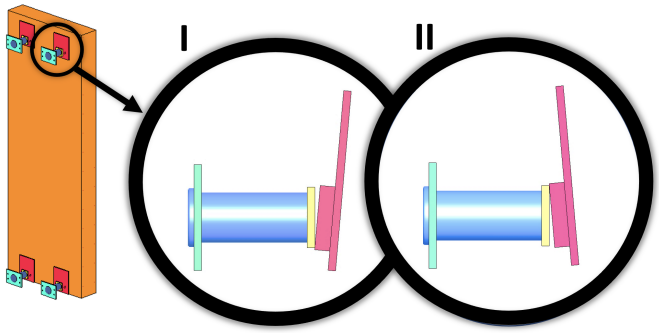

Figure 5.3: Example of two possible scenarios due to the slope of the panel: I) rotation in the clockwise direction (CW) and II) rotation in the counterclockwise direction (CCW).

In the analyses it was admitted a conservative estimate of 5 degrees of inclination at the top, which corresponds to the bottom of the slab being displaced by 24 cm. The results with and without hinge are displayed in Tables 5.2 and 5.3.

From the results collected, some conclusions can be drawn, such as:

- Total inversion across all loads is higher in the case of having the hinge element (except for the 250 kg of TNT, with CW motion);
- Velocity values are higher when using the hinge element, which may portray an easier deformation of the material, and consequently, a more efficient energy dissipation;
- Internal energy is also higher across all the tested charge loads, which indicates that more energy is absorbed in case of having a hinge, coherent to the total inversion results;
- Force results are divided. For smaller blast loads, the system with a hinge is slightly more effective, except for the 150 kg of TNT. However, from 200 kg of TNT to higher loads, which includes the last two cases (with the exhaustion of the absorption capacity), generates a greater force due to the impact resultant from the EAC crushing.
- Considering the two last more severe cases with EAC crushing, is evident the amplification effects it has on both solutions. However, the amplification on the case with the hinge element, is considerably lower.

Observations on the 150 kg case, with hinge element

The 150 kg case is an outlier, and therefore, deserving of being studied to better understand the origin of the high peak force. Thus, it was decided to analyse by comparison both cases, 100 kg and 150 kg, as shown in Figures 5.4 and 5.5 to understand such differences.

Table 5.2: Load increment results for the maximum eccentricity case with hinge, for increasing loads of TNT.

Charge Load $[kg]$	Final length Top $[m]$	Final length Bottom $[m]$	Total Inversion $[mm]$	Velocity $[m/s]$	Max Kinetic Energy $[J]$	Internal Energy $[J]$	Peak Resultant Force $[N]$	Peak Impact Force $[N]$	Impulse $[N \cdot s]$
300 TNT	- 0.0226	- 0.0061	609.68	46.85	10 461.36	16 043.08	229 574.40	271 962.80	352.00
250 TNT	- 0.0109	0.0056	562.86	39.35	7 345.07	12 218.13	186 051.70	205 933.50	402.02
200 TNT	0.0000	0.0241	504.24	31.40	4 635.80	8 734.47	158 135.20	-	324.22
150 TNT	0.0508	0.0742	302.38	23.40	2 793.02	5 262.75	183 988.50	-	267.65
100 TNT	0.0903	0.1165	138.76	14.69	1 076.90	2 435.02	114 547.10	-	185.00
60 RIODIN	0.1161	0.1333	53.63	9.03	399.42	807.30	78 659.48	-	100.80

Table 5.3: Load increment results for the maximum eccentricity case without hinge, for increasing loads of TNT.

Charge Load $[kg]$	Final length on Top $[m]$	Final length Bottom $[m]$	Total Inversion $[mm]$	Velocity $[m/s]$	Max Kinetic Energy $[J]$	Internal Energy $[J]$	Peak Resultant Force $[N]$	Peak Impact Force $[N]$	Impulse $[N \cdot s]$
300 TNT (CW)	- 0.0103	- 0.0168	606.55	41.63	8 918.75	13 655.08	186 283.40	328 120.80	480.00
300 TNT (CCW)	- 0.0152	- 0.0101	602.94	41.34	8 705.55	13 395.62	197 475.00	303 986.20	476.00
250 TNT (CW)	- 0.0014	- 0.0041	563.42	35.02	6 222.07	10 465.18	170 373.50	194 875.70	425.00
250 TNT (CCW)	- 0.0043	0.0010	559.03	34.60	6 072.02	10 275.18	178 344.50	219 464.70	411.00
200 TNT (CW)	0.0375	0.0304	416.69	27.73	3 903.41	7 233.04	166 476.20	-	316.00
200 TNT (CCW)	0.0321	0.0395	409.17	27.45	3 816.30	7 094.50	163 050.40	-	316.00
150 TNT (CW)	0.0755	0.0686	264.32	20.66	2 158.74	4 373.17	157 996.00	-	254.00
150 TNT (CCW)	0.0697	0.0769	259.36	20.43	2 109.84	4 296.76	159 798.90	-	253.00
100 TNT (CW)	0.1092	0.1022	129.50	13.75	951.93	2 142.70	119 232.30	-	198.00
100 TNT (CCW)	0.1038	0.1106	123.59	13.23	886.17	2 078.31	104 300.40	-	188.00
60 RIODIN (CW)	0.1313	0.1258	38.25	8.69	390.74	725.14	92 928.09	-	127.00
60 RIODIN (CCW)	0.1263	0.1326	34.64	8.14	358.57	699.38	88 211.65	-	117.00

From the graph (Figure 5.4), a similar pattern is shared between the two. Initially force values increase due to both, local buckling and inversion, although local buckling is the most dominant mechanism in terms of deformation. Somewhere in between, it is registered a peak force value, which soon after, returns to a lower and constant force pattern, which the inversion mechanism is the most dominant, until force values cancel out.

Considering the fringe plot (Figure 5.5), relative to the instant of maximum force value in each model, its important to clarify that the fringe plot color range is different from (I) and (II), with the aim of better illustrating the behavior developed by them.

In the first case (I), the EAC deforms axially. Peak force is registered with the development of local buckling. EAC has almost no bending deformation, except for the impactor plate. As soon as the first ”fold” is formed, there is a phase of resistance, illustrated by a), a fine red line, around the ”fold”, at 3.1 ms time-frame. This area concentrates stresses until the ”fold” is crushed impinging the peak force value through the tube. This phase of resistance is present in other cases as well, although this one, is more severe.

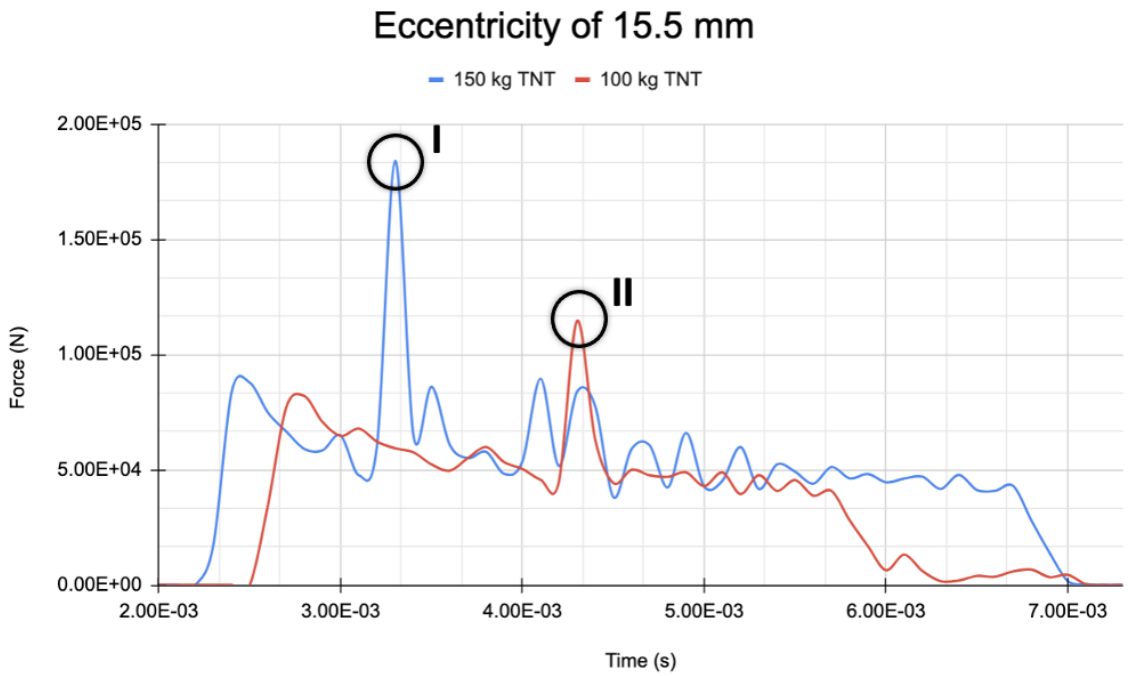

Figure 5.4: Representation of the Force in relation with time, for the 100 kg and 150 kg of TNT, with hinge element.

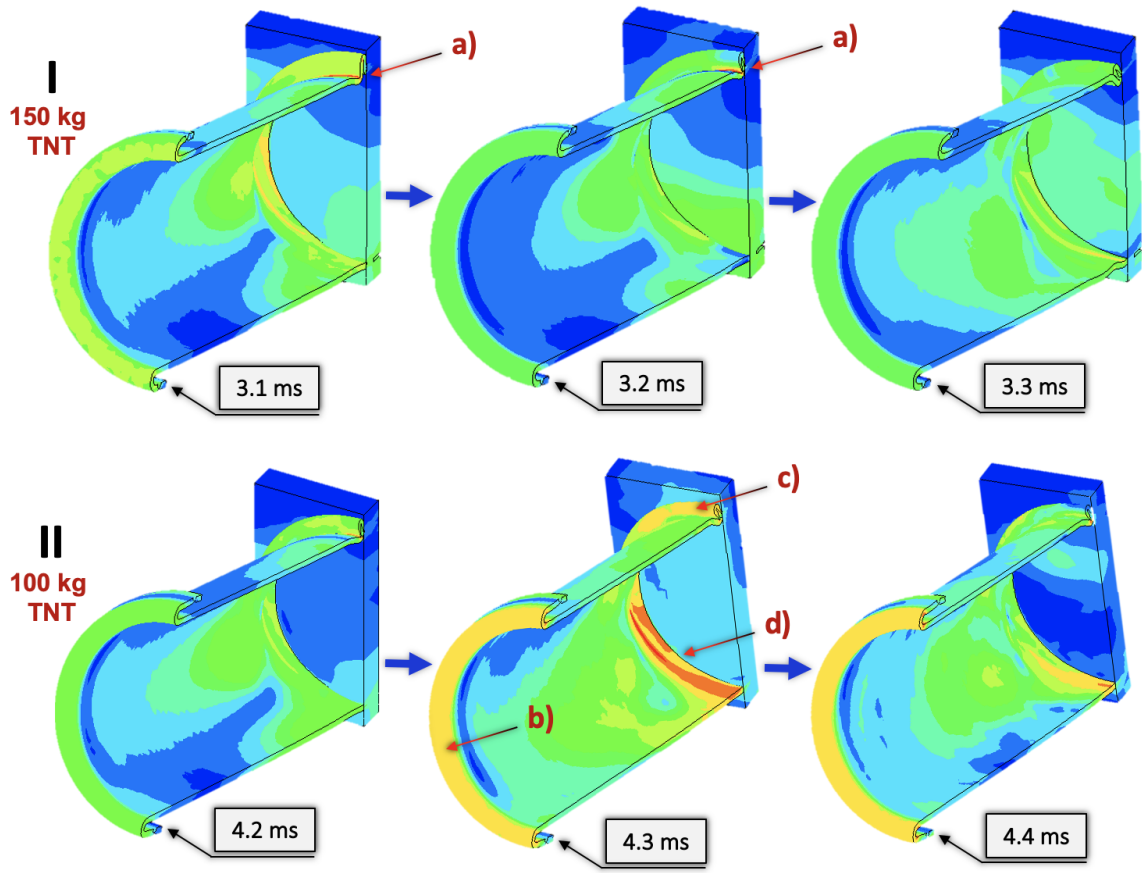

Figure 5.5: Representation of the stress fringe plot of the respective models in the study: (I) for the 150 kg of TNT case with the predominant buckling mechanism and (II) for the 100 kg TNT case with the additional bending mechanism.

Conversely, in the second case (II), with 100 kg of TNT, deformation occurs through bending and inversion. Peak force is registered in the instant where both buckling and bending mechanism deformation occur. Bending mechanism of the tube and the impactor plate, create the higher values of stress into two areas: i) on the tube inversion area illustrated by b); and ii) around the ”fold” area, outlined by c) and d), at 4.3 ms, concentrating more stress in the lower part of the tube, illustrated by d), due to the bending mechanism. This mechanism is an important effect, that allows the EAC to deform in a slightly effortless manner, with less resistance, dissipating energy more effectively, thus reducing peak force values.

Observations for the perfect setting

Let's consider now, the second scenario with perfect conditions. When full contact is achieved, and the system has no eccentricity, illustrated in Figure 5.6 whose results are detailed in Table 5.4.

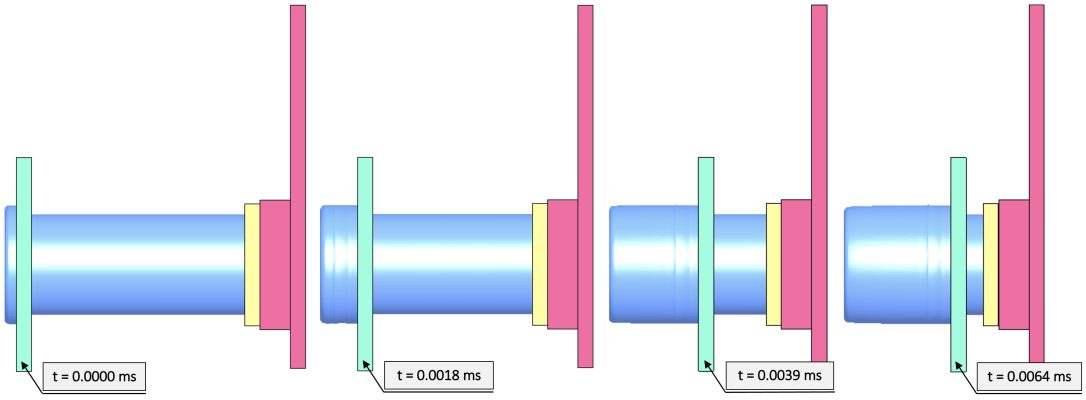

Figure 5.6: Example of the 200 kg case deformation, to highlight the inversion mechanism without buckling deformation.

Table 5.4: Comparison of results with a perfect hypothetical situation using no hinge, for increasing loads of TNT.

Charge Load $[kg]$	Final length $[m]$	Total Inversion $[mm]$	Velocity $[m/s]$	Max Kinetic Energy $[J]$	Internal Energy $[J]$	Peak Resultant Force $[N]$	Peak Impact Force $[N]$	Impulse $[N \cdot s]$
300 TNT	- 0.0125	602.36	40.80	8 467.89	12 824.89	179 396	345 360	472.00
250 TNT	- 0.0024	562.12	33.97	5 887.82	9 821.67	162 947	269 233	408.00
200 TNT	0.0315	426.42	27.00	3 697.05	6 758.63	123 548	-	316.00
150 TNT	0.0733	259.33	19.89	2 014.23	4 043.91	104 355	-	252.20
100 TNT	0.1070	124.34	12.63	804.04	1 906.49	84 810	-	184.00
60 RIODIN	0.1282	39.55	7.79	305.20	631.97	81 132	-	104.00

From the obtained results, conclusions are, to some extent, similar to the previous ones, related to the scenarios with imperfections (rotation) due to the slope of the panel.

- Values where the final length is negative, indicates that the connector has collapsed, exhausting its energy absorption capacity and deforming the adjacent plate, which in turn absorbs more energy.;
- Total inversion length values are lower compared to the hinge case;
- Velocity values, are also lower, as well as the Kinetic Energy (except for the 100 kg of TNT case);
- Peak Resultant force, is once again divided. For the experimental load (60 kg of RIODIN) and the two highest charge loads (250 kg and 300 kg, of TNT) the hinge case has better behavior and

vice-versa;

- The amplification effects are also very high compared to the hinge case.

Nevertheless, the latter analysis supports, that the compounding effect of both bending and inversion deformation mechanism of the EAC, can be more beneficial to energy and force absorption than axial inversion deformation mechanism alone.

5.3 Simulation 3: Contact between EAC elements

During the previous analysis, a few aspects stood out. Among them, the risk of contact (Figure 5.7), between the EAC elements. Therefore, it was analysed the worst case scenario, considering eccentric loading, to accurately assess if there is contact between elements, precisely the inverted tube surface and its adjacent plate edges. Several possibilities have been tested to better understand this effect, whose results are presented in Table 5.5.

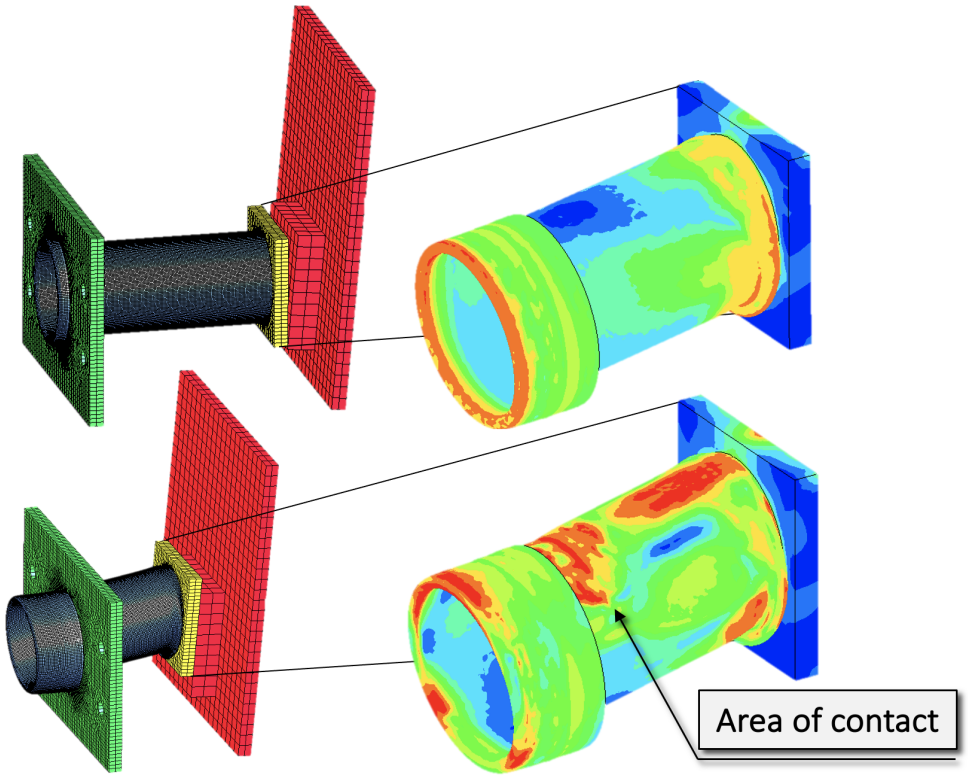

Figure 5.7: Example of the 150 kg case, with CW direction, where there was an impact between EAC elements, precisely between the fixing plate edge (green part) and the inverted tube surface (blue part).

From the table, values of ”maximum proximity” illustrate how close the elements of the inverted tube and the fixing plate were from contact. From those, certain observations can me made, namely that:

- The last values are null, on account of the absorption capacity of the system being exceeded, resulting in the total collapse of the system;
- The first values increase, and tend to a constant value of 6.4 mm, which is the vertical distance between the tube surface and the fixing plate, under undeformed conditions (perfectly straight and

Table 5.5: Load increment results on the maximum eccentricity case with the hinge element, regarding contact risk.

Charge Load $[kg]$	Final length Top $[m]$	Final length Bottom $[m]$	Total Inversion $[mm]$	Maximum Proximity $[mm]$
300 TNT	- 0.0226	- 0.0061	609.68	0.00
250 TNT	- 0.0109	0.0056	562.86	0.00
200 TNT	0.0000	0.0241	504.24	3.08
150 TNT	0.0508	0.0742	302.38	6.92
100 TNT	0.0903	0.1165	138.76	4.89
60 RIODIN	0.1161	0.1333	53.63	1.09

perpendicular). This data results capture the bending effect. For lower loads, the tube deforms not only by inversion mechanisms (and in some cases, local buckling) but also by bending mechanism. Being this effect more pronounced for lower loads;

- All the testing carried out, only happened in one case (200 kg of TNT charge load, with 20.7 mm of eccentricity), which suggests that, as long as the protective system has the capacity to absorb the blast load, there are low probabilities of having contact between elements in blast loading conditions. Nevertheless, in that specific case with contact, the protective system performed even better. The usual peak force value, turned into three, reducing peak force values, which again reinforces the system's ability to, not only deal well with imperfections and severe issues, but also to perform better in these situations.

5.4 Simulation 4: Deformation behavior

From the results obtained in the previous simulation, some additional findings were made in relation to the development of the EAC deformation mechanisms, whose results are given in Table 5.6 and Table 5.7.

Table 5.6: Load increment results on the maximum eccentricity case with the hinge element, regarding deformation behavior.

Charge Load $[kg]$	Final length Top $[m]$	Final length Bottom $[m]$	Total Inversion $[mm]$	Angle $[^\circ]$	Capacity $[\%]$
300 TNT	- 0.0226	- 0.0061	609.68	12.57	116.12
250 TNT	- 0.0109	0.0056	562.86	12.59	107.77
200 TNT	0.0000	0.0241	504.24	18.02	100.00
150 TNT	0.0508	0.0742	302.38	17.60	63.74
100 TNT	0.0903	0.1165	138.76	19.55	35.52
60 RIODIN	0.1161	0.1333	53.63	13.03	17.05

- Buckling deformation occurs from a specific charge of TNT, although its starting value is not very high, (around 60 kg of RIODIN charge, where results show some minor evidence of local buckling, represented in Figure 5.8). With 100 kg of TNT, buckling phenomena is clear, with the formation of one "fold" and its respective crushing.
- Local buckling, near the area where the hinge impacts the impactor plate, is the first mechanism of response to high force values originated by the blast loading. It buckles locally (forming a fold)

Table 5.7: Load increment results with no eccentricity, regarding deformation behavior.

Charge Load $[kg]$	Final length $[m]$	Total Inversion $[mm]$	Capacity $[\%]$
300 kg TNT	- 0.0130	604.20	109.25
250 kg TNT	- 0.0057	575.02	104.04
200 kg TNT	0.0157	489.70	88.80
150 kg TNT	0.0633	299.02	54.75
100 kg TNT	0.1021	144.04	27.08
60 RIODIN	0.1264	46.65	9.69

and crushing it afterwards, where it transitions from buckling to inversion mechanism (Figure 5.9).

- Through Figure 5.10 and Figure 5.11, it is possible to observe that the instant in which the transition of deformation mechanisms occurs, can be linked to a loss of efficiency.

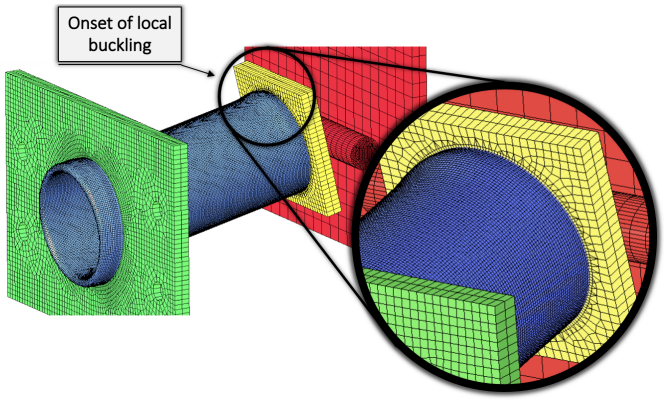

Figure 5.8: Illustration of minor signs of local buckling, from the model with 60 kg of RIODIN charge.

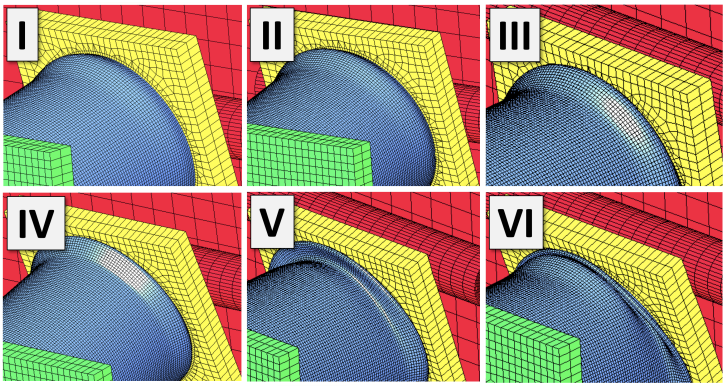

Figure 5.9: Representation of the successive moments that characterise the local buckling of the EAC.

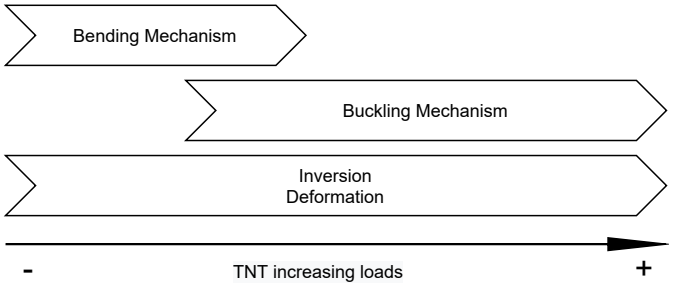

Figure 5.10: Diagram of deformation modes progression as load increases.

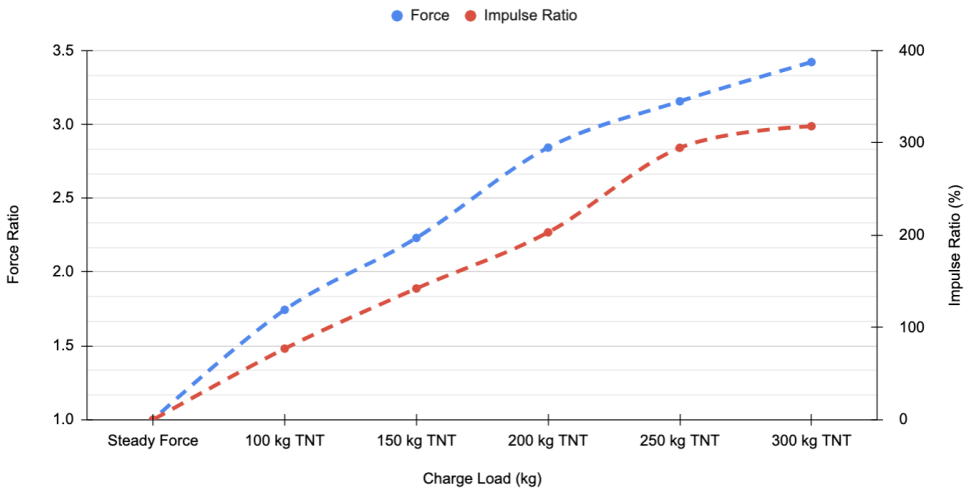

Figure 5.11: Graph of force and impulse ratio values, with increasing charge load.

- For higher loads, from 100 kg of TNT and upwards, the local buckling becomes more evident. There is, therefore, significant stress to cause local buckling.
- Until the first two cases (60 kg of RIODIN and 100 kg of TNT), the EAC was deforming by bending and inversion mechanisms (and eventually local buckling with the 100 kg case). However, after this point, the bending deformation decreases significantly (almost to none). The instant of transition will occur between the 150 kg case and the 200 kg case. Indeed, the bending mechanism occurs in virtually unnoticed manner in the first instants with 150 kg case. However by the 200 kg case it is non-existent.
- An interesting aspect, in the results with maximum eccentricity, is the angle formed by the impactor plate, that receives the hinge on impact, after the blast, which allows to see the transition of the different deformation mechanisms. Around 13 degrees ($\approx$ 60 kg of RIODIN), will be the limit of a perfect inversion without local buckling. For higher angles, local buckling starts to become more pronounced.

5.5 Simulation 5: Eccentricity analysis

One of the most relevant analyses is the eccentricity one. As mentioned before several times, including Chapter 3 observations, most cases verified an eccentric impact, causing a slight rotation of the

EAC. Therefore, the influence of eccentricities was analysed.

5.5.1 Eccentricity Analysis for 60 kg of RIODIN

An isolated EAD, was analysed under the same loading conditions, corresponding to the experimental load, for different eccentricity values, as displayed in Table 5.8.

Table 5.8: Eccentricity analyses results for the experimental load, 60 kg of RIODIN.

Eccentricity $[mm]$	Final Length on Top $[m]$	Final Length on Bottom $[m]$	Total Inversion $[mm]$	Velocity $[m/s]$	Initial Kinetic Energy $[J]$	Internal Energy $[J]$	Impulse Variation $[\%]$
0.0	0.1264	0.1265	46.4812	8.7127	363.9171	745.3704	0.00
5.2	0.1254	0.1272	47.2328	8.8303	367.4683	756.0086	-0.49
10.3	0.1240	0.1284	47.5378	8.8393	368.2507	758.8854	-2.34
15.5	0.1223	0.1298	48.0506	8.8392	371.2195	761.1432	-3.83
20.7	0.1206	0.1310	49.3750	8.8602	373.4810	764.5676	-4.61
25.9	0.1181	0.1321	51.9326	8.8836	382.6451	774.8716	-4.55
31.0	0.1161	0.1333	53.6526	8.9905	399.4160	806.8705	-3.75

From the given results, some insightful remarks can be made. For higher values of eccentricity:

- Total inversion increases, which together with increasing values of internal energy (Figure 5.16), can be taken as an increase in energy-absorption;
- Velocity increase slightly, which again reinforces the previous point. Having higher values of velocity entails that deformation occurs in an effortless manner. Such effect translates in more deformed material, therefore, more energy dissipated.

Observations on bending deformation effect

There is a relevant effect that is related to higher values of eccentricity. If a force is eccentric, this means that there will be a coupling moment on the structure and thus it will have more deformation. When the EAC is demanded, at 0 mm eccentricity, it undergoes a plastic deformation by inversion. Nevertheless, when eccentricity increases, there will be a specific point where the EAC, will not only deform by inversion but will also occur a bending deformation, which becomes more significant for higher eccentricity values.

One could think that this effect would difficult the inversion, therefore absorb less energy. However, when analysing data results carefully, through fringe plotting its possible to conclude that the EAC has a similar plastic deformation by inversion, followed by the plastic deformation by bending. Energy is dissipated by both plastic deformations, being the overall value of energy-absorption superior to the cases where there is no bending deformation.

Total inversion and impulse values (Figure 5.12), also support this aspect, by having the highest values of impulse and lowest values of deformation near the center of the cylindrical structure (0 mm case), and having the lowest values of impulse and highest values of inversion length for higher values of eccentricity.

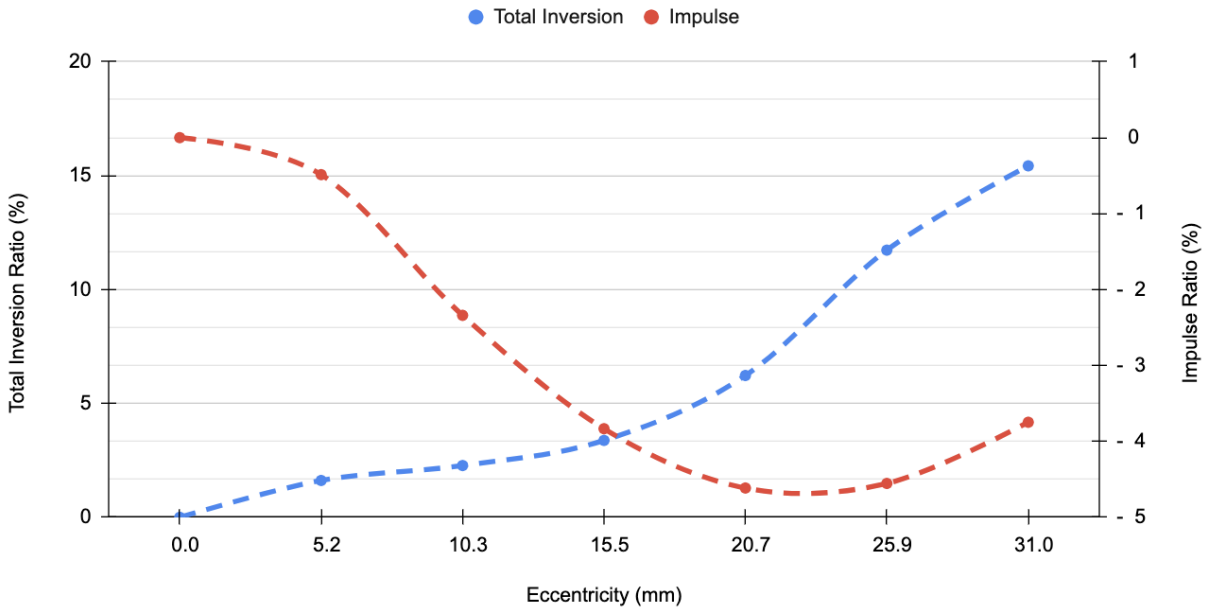

Figure 5.12: Graph of the force and impulse ratio for the 60 kg of RIODIN case.

To conclude, hypothetically, if a controlled introduction of eccentricity was possible, then data shows that it could contribute to a more efficient energy absorption, thus a better performance by the EADs. However, in reality it is difficult control such variable and implement it, in practice. What can be concluded instead, is how effective the system is, that even if it has this initial imperfections (rotations, eccentricities, and others), it most likely isn't prejudicial, much on the contrary, it probably will have a better performance.

Observations on peak force values from 0 mm to 5.2 mm

Regarding the development of the force values, theoretically, it was expected that data results would show maximum values at 0 mm of eccentricity. It was also expected that those force values would progressively decrease with higher values of eccentricity. However, in the very beginning, analysis results show an increase of force values up to at least 5.2 mm of eccentricity (Figure 5.13), and just then, they decrease as expected. Such effect deserves, therefore, to be analysed.

Despite being relatively similar, a comparison between the two situations, at the instant of peak force, reveals slight differences. Namely, in the case of 0 mm, where a greater concentration of stresses is observed in the inverted tube and in the contact area between the impactor plate and the hinge. Moreover, it is observed that in the case of 0 mm, there is a slightly greater plastic deformation, compared with the alternative. This effect allows greater absorption of energy and consequently a lower peak force.

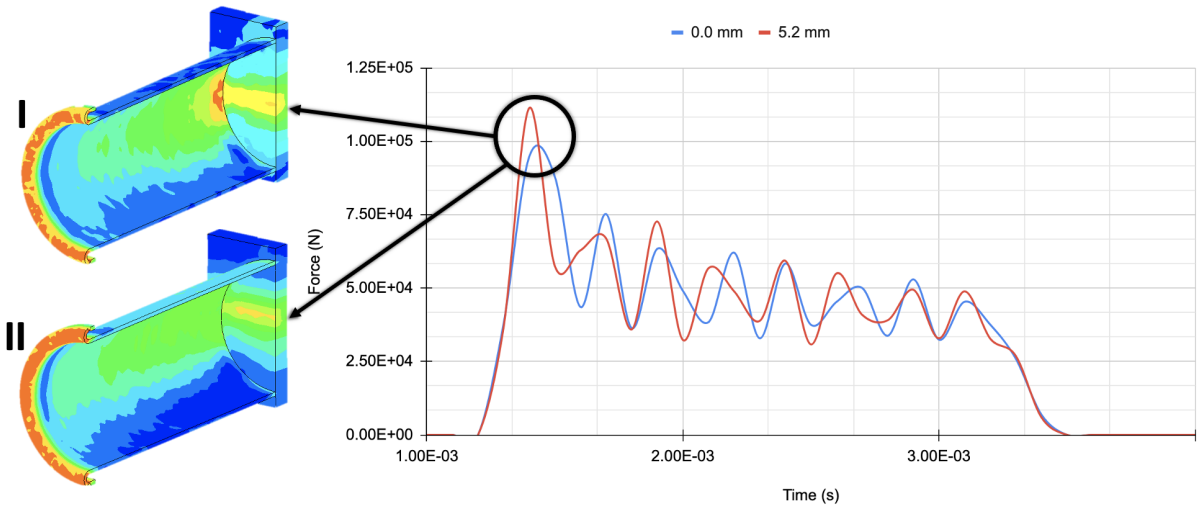

Figure 5.13: Graph of the force and impulse ratio for the 60 kg of RIODIN case, with the illustration of the respective fringe plot results. (I) relative to the 0.0 mm case and (II) to the 5.2 mm case.

5.5.2 Eccentricity Analysis for 200 kg of TNT

This analysis was motivated to better understand if the previous observations were also verified for higher load conditions. Results are presented in Table 5.9.

Table 5.9: Eccentricity analysis results for the 200 kg load of TNT.

Eccentricity [mm]	Final Length on Top [m]	Final Length on Bottom [m]	Total Inversion [mm]	Velocity [m/s]	Max Kinetic Energy [J]	Internal Energy [J]	Force Variation [%]	Impulse Variation [%]
0.0	0.0157	0.0157	489.67	30.12	4 295.81	7 920.88	0.00	0.0000
5.2	0.0144	0.0160	491.62	30.09	4 299.57	7 925.12	- 3.73	0.3155
10.3	0.0143	0.0168	490.18	30.15	4 307.12	7 922.64	- 7.52	0.6309
15.5	0.0142	0.0191	485.85	30.19	4 323.00	7 943.21	- 16.63	0.9464
20.7	0.0092	0.0325	469.03	30.79	4 607.78	8 265.01	- 25.76	6.9401
25.9	0.0004	0.0268	497.92	31.05	4 613.69	8 501.09	2.04	1.2618
31.0	0.0000	0.0241	504.24	31.36	4 635.80	8 734.47	- 7.97	2.2713

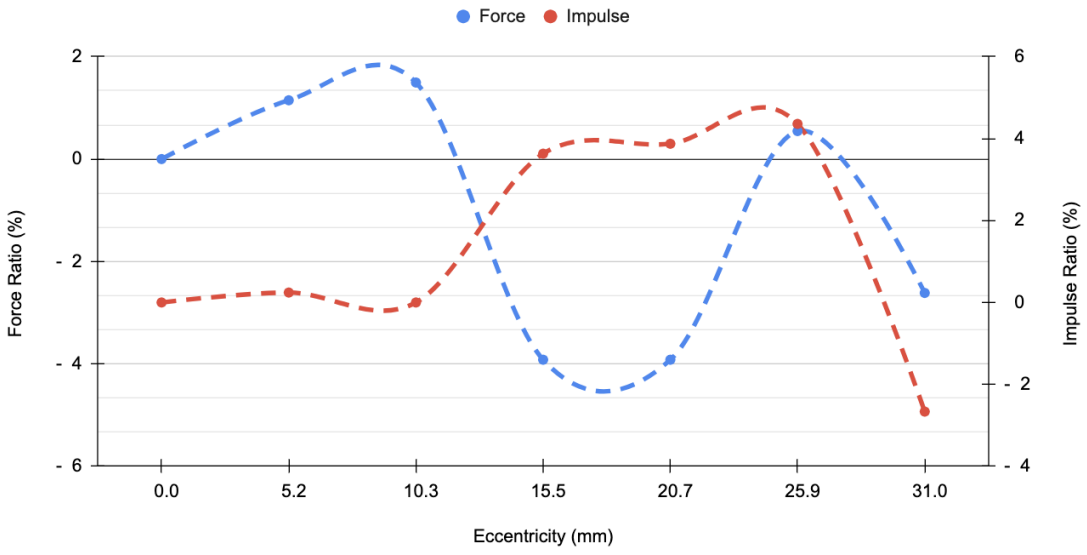

Figure 5.14: Graph of the force and impulse ratio for the 200 kg of TNT case.

Observations on peak force and impulse values from 20.7 mm to 25.9 mm eccentricities

Looking to the previous analysis, it was expected that force values would decrease continuously, however, they increase, with a maximum peak value at 25.9 mm of eccentricity.

Comparing both models, of 20.7 mm and 25.9 mm of eccentricity, it is possible to notice some relevant details, through Figure 5.15.

- The 25.9 mm case is similar to the previous situation, (150 kg of TNT, with 15.5 mm of eccentricity), where it was found an instant with higher resistance, after the local buckling effects (”fold” formation);
- According to Figure 5.15, the 20.7 mm case, unlike the usual pattern, describes three evident peak values of force;
- The first peak value corresponds to the plastic deformation of the surrounding area of the inverted tube due to the impact with the hinge plate, occurring local buckling, illustrated by the ”fold” formed (highlighted in red);
- The second peak value matches the instant where the ”fold” is crushed;
- The third peak value is due to an impact between the inverted tube surface and the fixing plate edge;
- Overall, the 20.7 mm case constitutes a trade-off, because it does not have a maximum strength value higher than the case of 25.9 mm as expected. However, these three peaks of force, ultimately contribute to a greater impulse.

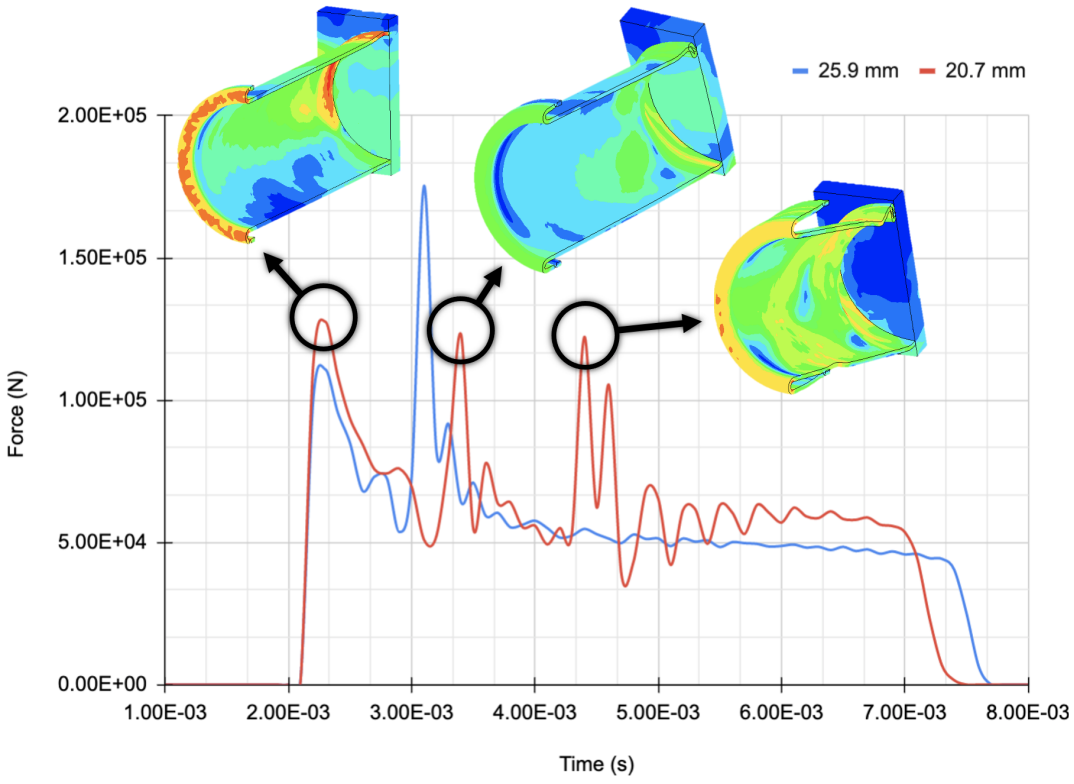

Figure 5.15: Graph comparing force values for 20.7 mm and 25.9 mm of eccentricities.

5.5.3 Internal Energy

One important variable, which gives us an insight into the absorption capacity of the system is the internal energy. Considering the results (Figure 5.16), some remarks can be made:

- Internal energy is lowest when eccentricity corresponds to the 0 mm case and increases progressively for higher values of eccentricity. That is expected. This is justified by cylindrical structures being the strongest when the load is on their longitudinal axis. In this case, there is only an axial type of deformation, inversion deformation. With stronger structures, deformations are smaller which means less internal energy, thus less energy absorbed;
- Across the three cases analysed, it is possible to see, that although the progression is constant towards the range between 10.3 mm and 15.5 mm, for higher values of eccentricity, there is an increase of internal energy, and therefore, in energy absorbed;
- Hypothetically, if the control of eccentricity in reality was something feasible, one could admit that having maximum eccentricity would improve its performance. However, in practice, its very difficult to guarantee these conditions.

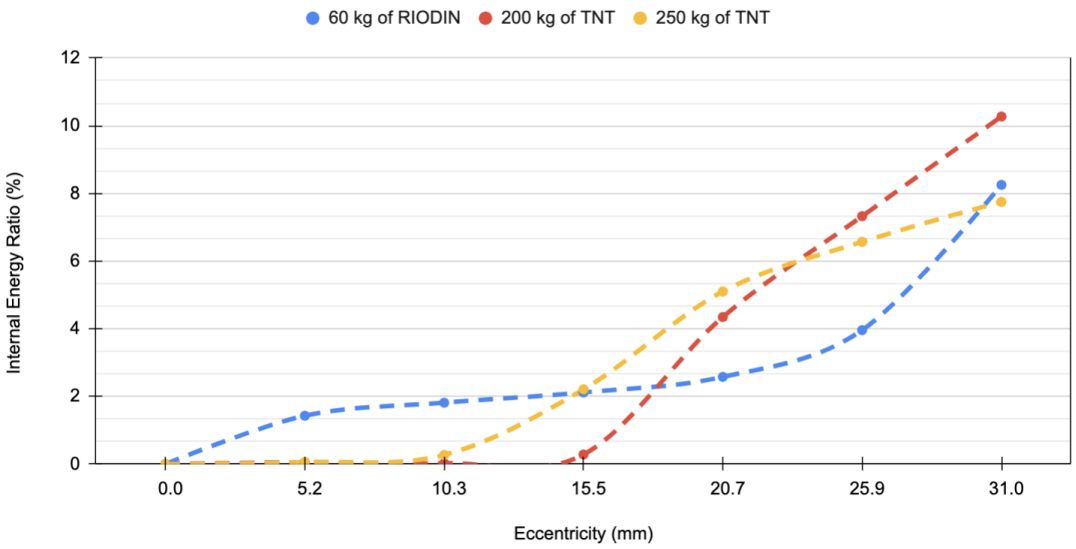

Figure 5.16: Graph of the internal energy ratio values compared to the minimum one.

5.6 Simulation 6: Full System Analysis

The goal of the following analysis was to obtain a quantifiable perception of the energy dissipation efficiency on the building by the shielding, and assess how the presence of the energy-absorption devices affects the performance of the system.

Unlike the previous deformable models, this new model with rigid EACs cannot be calibrated based on deformations. Since the EACs are considered rigid, it prevents it from deforming. In this case, the analysis used another parameters, namely the reaction forces registered on the wall, shown in Table 5.10 and in Figure 5.17. Furthermore, the deformation at midspan was also considered.

Table 5.10: Rigid System numerical results.

Model	Resultant Force - Wall $[N]$
Rigid system	206 910.2

Experimental results, Figure 5.17, display the reaction force curve of rigid and deformable systems. By analysing it, insights on the absorption performance that this system offers, can be obtained by their difference, which corresponds to an energy-absorption of the force peak approximately by 38%. Additionally, it reduces impulse as well, by 42%.

The numerical results achieved similar outcomes in relation to the internal energy, as shown in Table 5.11 and Table 5.12, precisely around 44% of the internal energy, in the respective load-case scenario. When addressing higher loads, it is registered a progressive increase of efficiency, registering an approximate reduction of 226% at the load of 200 kg.

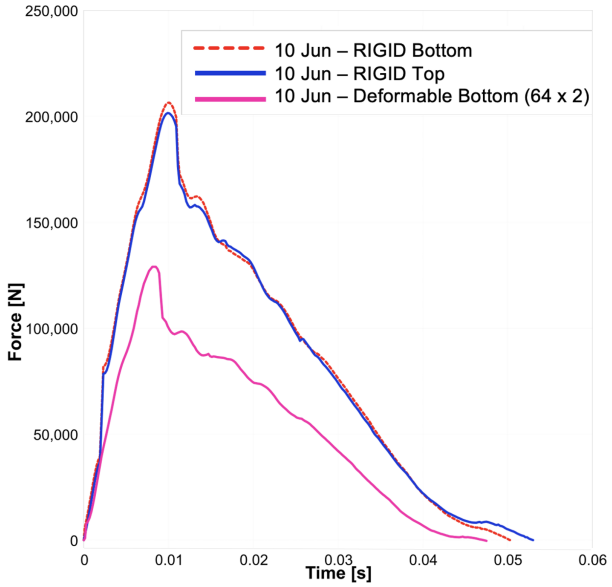

Figure 5.17: Full System experimental results [27].

Table 5.11: Full system analyses with increasing charges of TNT.

Charge load $[kg]$	Total Inversion $[mm]$	Capacity $[\%]$	Velocity $[m/s]$	Max Kinetic Energy $[J]$	Internal Energy $[J]$	$\delta_{midspan}$ $[mm]$	Angle $[°]$
250 TNT	670.8372	121.44	11.45	104 113.40	90 278.68	16.4	6.80
200 TNT	613.2228	111.01	9.56	72 958.74	65 674.22	13.6	5.66
150 TNT	525.0992	95.06	7.58	45 835.70	45 913.85	7.76	3.23
112 TNT	511.0724	92.52	5.99	23 797.69	32 256.03	4.92	2.05
100 TNT	431.0395	78.03	5.47	18 503.63	27 114.29	4.86	2.02
60 RIODIN	88.5540	16.03	2.34	4 590.76	5 221.53	3.69	1.54

Briefly, considering the deformable and rigid systems, one can observe that internal energy values are higher in the deformable cases. Therefore, one can assume that the attenuation of the building response by the shielding will correspond to a favorable energy-absorption by the protective system, which increases for higher loads.

Table 5.12: Full rigid system analyses with increasing charges of TNT.

Charge load $[kg]$	Internal Energy $[J]$	$\delta_{midspan}$ $[mm]$	Angle $[^{\circ}]$
250 TNT	-	-	-
200 TNT	20 171.85	-	-
150 TNT	22 427.88	-	-
112 TNT	19 726.71	11.10	4.62
100 TNT	16 560.18	9.59	3.99
60 RIODIN	3 635.10	3.54	1.48

Results are coherent from those obtained in the experimental campaign. The capacity of the system is surprisingly good, being virtually able to withstand big loads before the collapse of the system.

Through several tests, the conclusions were that the system was most efficient until 200 kg of TNT, where it has been verified evidence of partial destruction of the wall at the rear side, simultaneously with the collapse of the EACs.

Chapter 6

Concluding remarks and future work

6.1 Observations and Conclusions

Engineering should aim to find solutions to the problems that arise on a daily basis. Taking into account the increasing possibility of terrorist attacks using explosives, it is important to mitigate this threat. In this regard, it is intended to give a contribution by evaluating the performance of this protection system when subjected to the effects of this action. Thus, the study of the phenomenon of an explosion, and its effects on an innovative system of energy absorption, was carried out, and its behaviour was analysed as well as the analysis of additional ideas.

The study conducted consisted in the numerical analysis, using the LS-DYNA software, of a protection system based on a concrete wall and energy absorption connectors, which mechanism relies in an inverted steel tube. The results of the developed numerical models were calibrated and validated, by experimental tests performed at full scale.

Nonetheless, the analysis carried out allowed the identification of the most important aspects for the development of a numerical model:

- To model a complex geometry, it is advantageous to consider dedicated third-party software, such as SolidWorks, capable of making the process more practical and less time-consuming;
- Modelling the geometry with full detail can become a waste of time and a waste of resources;
- The integrity of the model, must be confirmed to avoid errors in the analysis;
- To mesh it is beneficial to use third-party software such as HyperMesh, which offers automatic cleaning and meshing functions, saving time and avoiding errors;
- Simplifications, become critical tools to achieve good results in a reasonable time;
- Being a highly dynamic problem, it is vital to consider strain-rate parameters in the model;
- Benchmarking, mesh convergence and experimentation are essential methods to create a trustworthy model;

With regard to the analyses, the most relevant aspects were:

- The numerical analysis confirms the resilience and efficiency of the solution in adverse conditions:

  - When the system has eccentricities;
  - when there is contact between elements;
  - When buckling phenomena occurs;
- EAC deformation limits, are derived from the deformable tube, which can be increased to certain lengths (conditioned by the possibility of global buckling phenomena of the tube);
- The EAC deformation behavior has three states of deformation: i) for lower loads has bending and inversion mechanisms; ii) for higher loads has buckling and inversion mechanisms; in between, it might a joint effect of the three.
- The protective system has the best performance for loads up to 100 kg of TNT. After 200 kg, the EAC exhausts the absorption capacity;
- For severe loads that lead to the exhaustion of the absorption capacity, having the hinge element, significantly reduces the amplification of forces on the protected structure;
- The higher the eccentricity the greater the energy dissipation;
- Bending mechanism leads to a effortless deformation, with less resistance, having a greater energy dissipation, thus reducing peak force values;
- The compounding effect of both bending and inversion deformation mechanisms, improves energy-absorption performance;
- The best results achieved, were obtained with the models where several different plastic deformations have occurred, without the premature rupture of the latter;
- The absorption effect depends not only on the EAC but also on the connector that contains it;

6.2 Future Work

- Elaboration of a similar analysis with a similar method, such as tube splitting;
- Elaboration of a similar analysis with the tube filled with energy-dissipation material (e.g., aluminium foam);
- Elaboration of a similar analysis of the remaining EADs and its comparison;
- Evaluate the effects of varying geometric properties of the EAC (e.g., diameter and thickness);
- Elaboration of a hybrid analysis, combining different connectors to combine their different capacities;
- Analyse the amplification effects of the full entire system;
- Evaluate a mixed solution, which would combine and complement this system;

Bibliography

[1] B. J. Buchanan. *Gunpowder, Explosives and the State: A Technological History*. Routledge, 1st edition edition, 2006. ISBN 9780754652595. URL https://www.routledge.com/Gunpowder-Explosives-and-the-State-A-Technological-History/Buchanan/p/book/9780754652595.

[2] J. Waller and C. Browning. *Becoming Evil: How Ordinary People Commit Genocide and Mass Killing*. Oxford University Press, 2002. ISBN 9780195148688. URL https://books.google.pt/books?id=dHBB4TJpcx0C.

[3] D. Cormie, G. Mays, and P. Smith. *Blast Effects on Buildings*. ICE Publishing, London, Dec 2019. ISBN 9780727761477. doi: 10.1680/beob.61477. URL https://www.icebookshop.com/Products/Blast-Effects-on-Buildings,-Third-edition.aspx.

[4] L. Seneca and R. Campbell. *Letters from a Stoic: Epistulae Morales Ad Lucilium*. Penguin Books, 1969. ISBN 9780140442106. URL https://books.google.pt/books?id=qLUxNQAACAAJ.

[5] M. Vergani. *How Is Terrorism Changing Us?: Threat Perception and Political Attitudes in the Age of Terror*. Palgrave MacMillan, 2018. ISBN 9789811080654. doi: 10.1007/978-981-10-8066-1. URL https://www.palgrave.com/gp/book/9789811080654.

[6] V. Marcelino. Terrorismo. 18 portugueses já foram vítimas de atentados desde 2001, 2019. URL https://www.dn.pt/mundo/terrorismo-18-portugueses-ja-foram-vitimas-de-atentados-10819452.html.

[7] P. ANSR/MAI. Acidentes de viação com vítimas, feridos e mortos - Continente, 2021. URL https://www.pordata.pt/Portugal/Acidentes+de+via%c3%a7%c3%a3o+com+v%c3%adtimas++feridos+e+mortos+++Continente-326. Accessed: 2021-07-22.

[8] P. Gill, J. Horgan, and J. Lovelace. Improvised explosive device: The problem of definition. *Studies in Conflict and Terrorism*, 34(9):732–748, 2011. ISSN 1057610X. doi: 10.1080/1057610X.2011.594946. URL https://doi.org/10.1080/1057610X.2011.594946.

[9] E. Miller. Trends in Global Terrorism: Islamic State's Decline in Iraq and Expanding Global Impact; Fewer Mass Casualty Attacks in Western Europe; Number of Attacks in the United States Highest since 1980s. Technical Report October, START - Study of Terroris and Responses of Terrorism,

2019. URL https://www.start.umd.edu/pubs/START_GTD_GlobalTerrorismOverview2019_July2020.pdf.

[10] A. Zhang, R. Woo, and H. Lawson. Four killed in gas explosion at Chinese BBQ restaurant, 2021. URL https://www.reuters.com/world/china/three-killed-gas-explosion-chinese-bbq-restaurant-2021-10-21/. Accessed: 2021-10-25.

[11] Reuters. Four killed in gas explosion at Chinese BBQ restaurant, 2021. URL https://apnews.com/article/europe-france-evacuations-kabul-9e457201e5bbe75a4eb1901fedeee7a1. Accessed: 2021-10-25.

[12] J. M. R. Santamaria and J. M. P. Correia. Propaganda of terror: Threats to security and safety in the European Union. *Portuguese Journal of Military Sciences [Revista de Ciências Militares]*, IX (1):243–273, May 2021. doi: 10.1016/j.jns.2006.06.017. URL https://www.ium.pt/?page_id=6461.

[13] EUROPOL. 2020 EU - Terrorism Situation and Trend report. 2020. URL https://www.europol.europa.eu/tesat-report. Accessed: 2021-08-02.

[14] M. Santaspirt. *Improvised explosive devices: assessing the global risk for use in terrorism*. PhD thesis, Rutgers, The State University of New Jersey, May 2020. URL https://rucore.libraries.rutgers.edu/rutgers-lib/64147/.

[15] L. D. Prockop. Weapons of mass destruction: Overview of the CBRNEs (Chemical, Biological, Radiological, Nuclear, and Explosives). *Journal of the neurological sciences*, 249:50–54, Dec 2006. doi: 10.1016/j.jns.2006.06.017. URL https://pubmed.ncbi.nlm.nih.gov/16920155/.

[16] M. D'Arienzo, F. Di Paolo, L. Chiacchiararelli, A. Malizia, and L. Indovina. A mathematical model for the diffusion of emergency warning messages during CBRNe emergencies. *Journal of Contingencies and Crisis Management*, 28(3):228–239, 2020. doi: https://doi.org/10.1111/1468-5973.12313. URL https://onlinelibrary.wiley.com/doi/abs/10.1111/1468-5973.12313.

[17] K. Rao and M. Latha. *Protection Against IED (Improvised Explosive Device) a Dreaded and Fearful Weapon of Terrorist – Problems, Solutions and Challenges*, volume 4, pages 218–225. Springer, Cham, Jul 2019. ISBN 978-3-030-24317-3. doi: 10.1007/978-3-030-24318-0_26. URL https://link.springer.com/chapter/10.1007%2F978-3-030-24318-0_26#citeas.

[18] K. Vasilis and S. George. Calculation of blast loads for application to structural engineering. Technical report, European Commission, Luxembourg, Dec 2013. URL https://core.ac.uk/download/pdf/38628317.pdf.

[19] S. Weinman. Blast incidents and their sequela. *Journal of Emergency Nursing*, 46(1):129–133, Jan 2020. ISSN 15272966. doi: 10.1016/j.jen.2019.10.013. URL https://www.jenonline.org/article/S0099-1767(19)30510-0/references.

[20] J. F. Murphy. Beirut explosion, 7 August 2020: Root cause investigation and management system failures. *Process Safety Progress*, 39(4):e12209, Oct 2020. ISSN 15475913. doi: https://doi.org/10.1002/prs.12209. URL https://aiche.onlinelibrary.wiley.com/doi/abs/10.1002/prs.12209.

[21] Murderpedia - Oklahoma City 1995, 1995. URL http://murderpedia.org/male.M/m1/mcveigh-timothy-photos-5.htm. Accessed: 2021-08-05.

[22] H. Smith. 1993: World Trade Center Bombing, 1993. URL https://buildingfailures.wordpress.com/1993/02/26/world-trade-center-bombing/. Accessed: 2021-08-05.

[23] K. R. Adam and S. Matt. Hundreds of Thousands Displaced by Beirut Explosion, 2020. URL https://nymag.com/intelligencer/2020/08/beirut-explosion-rocks-lebanons-capital.html. Accessed: 2021-08-05.

[24] D. O. Dusenberry. *Handbook for Blast-Resistant Design of Buildings*. Wiley, Jan 2010. ISBN 9780470170540. doi: 10.1002/9780470549070. URL https://onlinelibrary.wiley.com/doi/book/10.1002/9780470549070.

[25] M. E. Hynes and N. Studies. *Blast Mitigation - Experimental and Numerical Studies*. Springer, Jul 2014. ISBN 9781461472667. doi: 10.1007/978-1-4614-7267-4. URL https://www.springer.com/gp/book/9781461472667.

[26] H. S. Norville, N. Harvill, E. J. Conrath, S. Shariat, and S. Mallonee. Glass-Related Injuries in Oklahoma City Bombing. *Journal of Performance of Constructed Facilities*, 13(2):50–56, May 1999. doi: 10.1061/(ASCE)0887-3828(1999)13:2(50). URL https://doi.org/10.1061/(ASCE)0887-3828(1999)13:2(50).

[27] G. Gomes. Blast Protective Walls Optimization Design (BLADE) - Blast testing report - 10th June's Blast testing on Protective System inversion tubes 64x2mm, NATO Counter IED COE, Madrid Spain. Technical report, 2020.

[28] S. D. Adhikary and S. C. Dutta. *Blast resistance and mitigation strategies of structures: Present status and future trends*, volume 172, chapter 4, pages 249–266. ICE Publishing, Apr 2019. doi: 10.1680/jstbu.17.00056. URL https://www.icevirtuallibrary.com/doi/abs/10.1680/jstbu.17.00056.

[29] K. Mueller. "Structural Design Considerations for Blast Loading" Web Seminar, 2020. URL https://shop.skghoshassociates.com/web-seminar-recordings/structural-design-considerations-for-blast-loading-2.html. Accessed: 2021-07-30.

[30] W. E. Baker, P. A. Cox, P. S. Westine, J. J. Kulesz, and R. A. Strehlow. *Explosion Hazards And Evaluation*, volume 5. Elsevier, 1983. doi: 10.1016/0379-7112(84)90044-4. URL https://www.elsevier.com/books/explosion-hazards-and-evaluation/baker/978-0-444-42094-7.

[31] C. Kingery, G. Bulmash, and U. A. B. R. Laboratory. *Airblast parameters from TNT spherical air burst and hemispherical surface burst*. Technical report ARBRL. US Army Armament and Development Center, Ballistic Research Laboratory, 1984. URL https://books.google.pt/books?id=lg6cHAAACAAJ.

[32] U. D. U.S. Department of Defense. *UFC 3-340-02*. Department of Defense - United States of America, 2008. URL https://www.wbdg.org/ffc/dod/unified-facilities-criteria-ufc/ufc-3-340-02.

[33] Gilbert F. Kinney and Kenneth J. Graham. *Explosive Shock in Air*. Springer, 1985. ISBN 9783642866845. URL https://www.springer.com/gp/book/9783642866845.

[34] N. M. Elsayed and J. Atkins. *Explosion and Blast-Related Injuries*. Elsevier Academic Press, 2008. ISBN 9780123695147. URL https://www.elsevier.com/books/explosion-and-blast-related-injuries/elsayed-ph-d/978-0-12-369514-7.

[35] H. Hao, Y. Hao, J. Li, and W. Chen. Review of the current practices in blast-resistant analysis and design of concrete structures. *Advances in Structural Engineering*, 19(8):1193–1223, 2016. doi: 10.1177/1369433216656430. URL https://journals.sagepub.com/doi/10.1177/1369433216656430.

[36] P. W. Cooper. Comments on TNT equivalence. *20th International Pyrotechnics Seminar*, page 16, 1994. URL https://www.osti.gov/servlets/purl/10168254.

[37] E. Yandzio and M. Gough. *Protection of Buildings against Explosions*. The Steel Construction Institute, 1999. ISBN 9781859420898. URL https://www.worldcat.org/title/protection-of-buildings-against-explosions/oclc/47874123.

[38] P. Vivek and T. G. Sitharam. *Granular Materials Under Shock and Blast Loading*. 2020. ISBN 978-981-15-0437-2. URL http://link.springer.com/10.1007/978-981-15-0438-9.

[39] P. A. Shirbhate and M. D. Goel. A Critical Review of Blast Wave Parameters and Approaches for Blast Load Mitigation. *Archives of Computational Methods in Engineering*, 28(3):1713–1730, 2021. ISSN 18861784. doi: 10.1007/s11831-020-09436-y. URL https://doi.org/10.1007/s11831-020-09436-y.

[40] I. Sochet. *Blast Effects*. Springer, 2018. ISBN 9783319708294. doi: 10.1007/978-3-319-57111-9{_}9230. URL https://link.springer.com/book/10.1007/978-3-319-70831-7.

[41] H. L. Brode. A Calculation of the Blast Wave from a Spherical Charge of TNT, Rand Corp. *Rep. RM-1965 (August 1957)*, page 61, 1957. URL https://www.rand.org/pubs/research_memoranda/RM1965.html.

[42] P. Sherkar, A. S. Whittaker, and A. J. Aref. Modeling the Effects of Detonations of High Explosives to Inform Blast-Resistant Design. Technical report, University at Buffalo,

2010. URL http://www.buffalo.edu/mceer/catalog.host.html/content/shared/www/mceer/publications/MCEER-10-0009.detail.html.

[43] U. D. U.S. Department of Defense. *TM 5-855-1: Fundamentals of Protective Design for Conventional Weapons*. Department of Defense - United States of America, 1986. URL https://www.nrc.gov/docs/ML1019/ML101970069.pdf.

[44] Gilbert F. Kinney and Kenneth J. Graham. *Explosive Shock in Air*. Springer, 1985. ISBN 9783642866845. URL https://www.springer.com/gp/book/9783642866845.

[45] C. E. Needham. *Blast Waves*. Springer, 2018. ISBN 9783319653815. doi: 10.1007/978-3-7091-4364-3{_}4. URL https://www.springer.com/gp/book/9783319653815.

[46] D. Hyde. Conwep: Conventional weapons effects program. *US Army Engineer Waterways Experiment Station, USA*, 2, 1991.

[47] T. Børvik, A. G. Hanssen, M. Langseth, and L. Olovsson. Response of structures to planar blast loads – A finite element engineering approach. *Computers and Structures*, 87(9-10):507–520, 2009. ISSN 0045-7949. doi: 10.1016/j.compstruc.2009.02.005. URL http://dx.doi.org/10.1016/j.compstruc.2009.02.005.

[48] P. D. Smith, T. A. Rose, and E. Saotonglang. Clearing of blast waves from building facades. *Proceedings of the Institution of Civil Engineers: Structures and Buildings*, 134(2):193–199, 1999. ISSN 09650911. doi: 10.1680/istbu.1999.31385.

[49] S. Qi, X. Zhi, F. Fan, and R. G. J. Flay. Probabilistic blast load model for domes under external surface burst explosions. *Structural Safety*, 87(November 2019):102004, 2020. ISSN 01674730. doi: 10.1016/j.strusafe.2020.102004. URL https://doi.org/10.1016/j.strusafe.2020.102004.

[50] W. Feng, B. Chen, F. Yang, F. Liu, L. Li, L. Jing, and H. Li. Numerical study on blast responses of rubberized concrete slabs using the Karagozian and Case concrete model. *Journal of Building Engineering*, 33(December 2019):101610, 2021. ISSN 23527102. doi: 10.1016/j.jobe.2020.101610. URL https://doi.org/10.1016/j.jobe.2020.101610.

[51] M. D. Goel, V. A. Matsagar, S. Marburg, and A. K. Gupta. Comparative Performance of Stiffened Sandwich Foam Panels under Impulsive Loading. *Journal of Performance of Constructed Facilities*, 27(5):540–549, 2013. ISSN 0887-3828. doi: 10.1061/(asce)cf.1943-5509.0000340. URL https://ascelibrary.org/doi/10.1061/%28ASCE%29CF.1943-5509.0000340.

[52] Y. Han and H. Liu. Finite element simulation of medium-range blast loading using LS-DYNA. *Shock and Vibration*, 2015, 2015. ISSN 10709622. doi: 10.1155/2015/631493. URL https://www.hindawi.com/journals/sv/2015/631493/.

[53] J. Hong, Q. Fang, L. Chen, and X. Kong. Numerical predictions of concrete slabs under contact explosion by modified K&C material model. *Construction and Building Materials*, 155:1013–1024,

2017. ISSN 09500618. doi: 10.1016/j.conbuildmat.2017.08.060. URL http://dx.doi.org/10.1016/j.conbuildmat.2017.08.060.

[54] V. Karlos, G. Solomos, and M. Larcher. *Analysis of blast parameters in the near-field for spherical free-air explosions*. 2016. ISBN 9789279576034. URL https://publications.jrc.ec.europa.eu/repository/handle/JRC101039.

[55] V. Pereira. Sistema Inovador de Protecção de Edifícios face a Explos\~{o}es , composto por Painéis de Fachada em Betão Armado e Conectores em Aço de Parede Fina com Capacidade de Absorção de Energia. Master's thesis, Nov 2017. URL https://fenix.tecnico.ulisboa.pt/cursos/mec/dissertacao/1972678479053993.

[56] J. Pinto. Comportamento de Estruturas de Aço sob a Ação de Explosões - Conceção de dissipadores de energia. Master's thesis, Nov 2018. URL https://fenix.tecnico.ulisboa.pt/cursos/mec/dissertacao/1409728525632293.

[57] Z. S. Tabatabaei and J. S. Volz. A Comparison between Three Different Blast Methods in LS-DYNA: LBE, MM-ALE, Coupling of LBE and MM-ALE. pages 1–10, 2012. URL https://www.dynamore.de/de/download/papers/2012-internationale-ls-dyna-users-conference/documents/blast-impact20-d.pdf.

[58] D. K. Thai, D. L. Nguyen, T. H. Pham, and Q. H. Doan. Prediction of residual strength of FRC columns under blast loading using the FEM method and regression approach. *Construction and Building Materials*, 276:15, 2021. ISSN 09500618. doi: 10.1016/j.conbuildmat.2021.122253. URL https://doi.org/10.1016/j.conbuildmat.2021.122253.

[59] Z. Yi, A. K. Agrawal, M. Ettouney, and S. Alampalli. Finite element simulation of blast loads on reinforced concrete structures using LS-DYNA. *New Horizons and Better Practices*, 2007. doi: 10.1061/40946(248)3. URL https://ascelibrary.org/doi/10.1061/40946%28248%293.

[60] F. Zapata and C. García-ruiz. Critical Reviews in Analytical Chemistry Chemical Classification of Explosives. *Critical Reviews in Analytical Chemistry*, 0(0):1–18, 2020. ISSN 1040-8347. doi: 10.1080/10408347.2020.1760783. URL https://doi.org/10.1080/10408347.2020.1760783.

[61] X. Zhang, Y. Ding, and Y. Shi. Numerical simulation of far-field blast loads arising from large TNT equivalent explosives. *Journal of Loss Prevention in the Process Industries*, 70(November 2020):104432, 2021. ISSN 09504230. doi: 10.1016/j.jlp.2021.104432. URL https://doi.org/10.1016/j.jlp.2021.104432.

[62] ASCE. *Design of Blast-Resistant Buildings in Petrochemical Facilities*. ASCE - American Society of Civil Engineers, 2010. ISBN 9780784410882. URL https://doi.org/10.1061/9780784410882.

[63] N. Newmark and S. Fraenkel. *An Engineering Approach to Blast Resistant Design*. Reprint series. University of Illinois, 1956. URL https://ascelibrary.org/doi/10.1061/TACEAT.0007366.

[64] U. S. F. C. D. Administration. *Windowless structures, a study in blast-resistant design. Technical manual [TM-5-4]*. 1952.

[65] R. K. Wharton, S. A. Formby, and R. Merrifield. Airblast TNT equivalence for a range of commercial blasting explosives. *Journal of Hazardous Materials*, 79(1-2):31–39, 2000. ISSN 03043894. doi: 10.1016/S0304-3894(00)00168-0. URL https://pubmed.ncbi.nlm.nih.gov/11040384/.

[66] P. D. Smith and J. G. Hetherington. *Blast and Ballistic Loadings of Structures*. Routledge, 1994. URL https://www.routledge.com/Blast-and-Ballistic-Loading-of-Structures/Hetherington-Smith/p/book/9780367866877?gclid=Cj0KCQjw8eOLBhC1ARIsAOzx5cF23VVbyoopx6sqJdHrFrS280_T90W-N5seq5Ks12vG3dPYe3Yg-tYaAv2OEALw_wcB.

[67] R. Bao and T. Yu. Impact and rebound of an elastic–plastic ring on a rigid target. *International Journal of Mechanical Sciences*, 91:55–63, 2015. ISSN 0020-7403. doi: https://doi.org/10.1016/j.ijmecsci.2014.03.031. URL https://www.sciencedirect.com/science/article/pii/S0020740314001180. Mechanics of Solids & Structures.

[68] Y. Wang, Y. Yang, S. Wang, Z. Huang, and T. Yu. Dynamic behavior of circular ring impinging on ideal elastic wall: Analytical model and experimental validation. *International Journal of Impact Engineering*, 122:148–160, 2018. ISSN 0734-743X. doi: https://doi.org/10.1016/j.ijimpeng.2018.07.009. URL https://www.sciencedirect.com/science/article/pii/S0734743X17306310.

[69] X. Qiu and T. Yu. Some topics in recent advances and applications of structural impact dynamics. *Applied Mechanics Reviews*, 64(3), 2011. URL https://asmedigitalcollection.asme.org/appliedmechanicsreviews/article-abstract/64/3/030801/370039/Some-Topics-in-Recent-Advances-and-Applications-of.

[70] A. Baroutaji, M. Sajjia, and A.-G. Olabi. On the crashworthiness performance of thin-walled energy absorbers: Recent advances and future developments. *Thin-Walled Structures*, 118:137–163, 2017. ISSN 0263-8231. doi: https://doi.org/10.1016/j.tws.2017.05.018. URL https://www.sciencedirect.com/science/article/pii/S0263823116308497.

[71] Q. Zhang, X. Yang, P. Li, G. Huang, S. Feng, C. Shen, B. Han, X. Zhang, F. Jin, F. Xu, and T. J. Lu. Bioinspired engineering of honeycomb structure – using nature to inspire human innovation. *Progress in Materials Science*, 74:332–400, 2015. ISSN 0079-6425. doi: https://doi.org/10.1016/j.pmatsci.2015.05.001. URL https://www.sciencedirect.com/science/article/pii/S0079642515000377.

[72] G. Imbalzano, S. Linforth, T. D. Ngo, P. V. S. Lee, and P. Tran. Blast resistance of auxetic and honeycomb sandwich panels: Comparisons and parametric designs. *Composite Structures*, 183:242–261, 2018. ISSN 0263-8223. doi: https://doi.org/10.1016/j.compstruct.2017.03.018. URL https://www.sciencedirect.com/science/article/pii/S0263822316324047. In honor of Prof. Y. Narita.

[73] Z. Wang, S. Yao, Z. Lu, D. Hui, and L. Feo. Matching effect of honeycomb-filled thin-walled square tube—experiment and simulation. *Composite Structures*, 157:494–505, 2016. ISSN 0263-8223. doi: https://doi.org/10.1016/j.compstruct.2016.03.045. URL https://www.sciencedirect.com/science/article/pii/S0263822316302100.

[74] R. D. Hussein, D. Ruan, G. Lu, S. Guillow, and J. W. Yoon. Crushing response of square aluminium tubes filled with polyurethane foam and aluminium honeycomb. *Thin-Walled Structures*, 110: 140–154, 2017. ISSN 0263-8231. doi: https://doi.org/10.1016/j.tws.2016.10.023. URL https://www.sciencedirect.com/science/article/pii/S026382311630372X.

[75] P. Feraboli. Development of a corrugated test specimen for composite materials energy absorption. *Journal of Composite Materials*, 42(3):229–256, 2008. doi: 10.1177/0021998307086202. URL https://doi.org/10.1177/0021998307086202.

[76] Z. Li, W. Chen, H. Hao, Q. Yang, and R. Fang. Energy absorption of kirigami modified corrugated structure. *Thin-Walled Structures*, 154:106829, 2020. ISSN 0263-8231. doi: https://doi.org/10.1016/j.tws.2020.106829. URL https://www.sciencedirect.com/science/article/pii/S0263823120307072.

[77] D. Karagiozova and M. Alves. Transition from progressive buckling to global bending of circular shells under axial impact—part i: Experimental and numerical observations. *International Journal of Solids and Structures*, 41(5):1565–1580, 2004. ISSN 0020-7683. doi: https://doi.org/10.1016/j.ijsolstr.2003.10.005. URL https://www.sciencedirect.com/science/article/pii/S0020768303005870.

[78] D. Karagiozova and M. Alves. Transition from progressive buckling to global bending of circular shells under axial impact – part ii: Theoretical analysis. *International Journal of Solids and Structures*, 41(5):1581–1604, 2004. ISSN 0020-7683. doi: https://doi.org/10.1016/j.ijsolstr.2003.10.006. URL https://www.sciencedirect.com/science/article/pii/S0020768303005882.

[79] N. Jones. *Structural impact*. Cambridge university press, 2011. URL https://www.cambridge.org/pt/academic/subjects/engineering/solid-mechanics-and-materials/structural-impact?format=AR.

[80] Z. Fan, G. Lu, T. Yu, and K. Liu. Axial crushing of triangular tubes. *International Journal of Applied Mechanics*, 5:50008–, 03 2013. doi: 10.1142/S1758825113500087. URL https://www.researchgate.net/publication/258789169_Axial_Crushing_of_Triangular_Tubes.

[81] M. Shakeri, S. Salehghaffari, and R. Mirzaeifar. Expansion of circular tubes by rigid tubes as impact energy absorbers: experimental and theoretical investigation. *International Journal of Crashworthiness*, 12(5):493–501, 2007. doi: 10.1080/13588260701483540. URL https://doi.org/10.1080/13588260701483540.

[82] T. S. Pei, S. Nadiah, S. Aishah, and N. Nadiah. Oblique Impact on Crashworthiness: Review. *International Journal of Engineering Technology and Sciences*, 2017. URL https://journal.ump.edu.my/ijets/article/view/6189.

[83] S. Al-Hassani, W. Johnson, and W. Lowe. Characteristics of inversion tubes under axial loading. *Journal of Mechanical Engineering Science*, pages 370–381, 1972. URL https://journals.sagepub.com/doi/abs/10.1243/JMES_JOUR_1972_014_046_02.

[84] G. Gomes. "Report of quasi-static inversion tests on thin-walled tubes". Technical report, Faculdade de Ciências e Tecnologia da Universidade Nova de Lisboa, Monte da Caparica, 2019.

[85] F. Pled, W. Yan, and C. Wen. Crushing modes of aluminium tubes under axial compression. page 6, 2012. URL https://www.researchgate.net/publication/43476694_Crushing_Modes_of_Aluminium_Tubes_under_Axial_Compression.

[86] M. D. Goel. Deformation, energy absorption and crushing behavior of single-, double- and multi-wall foam filled square and circular tubes. *Thin-Walled Structures*, 90:1–11, 2015. ISSN 0263-8231. doi: https://doi.org/10.1016/j.tws.2015.01.004. URL https://www.sciencedirect.com/science/article/pii/S0263823115000075.

[87] J. Sáiz, J.-L. Ferrando, J.-C. Atoche, M. Torre, and C. García-Ruiz. Study of losses of volatile compounds from dynamites. investigation of cross-contamination between dynamites stored in polyethylene bags. *Forensic Science International*, pages 27–33, 2011. ISSN 0379-0738. doi: https://doi.org/10.1016/j.forsciint.2011.04.007. URL https://www.sciencedirect.com/science/article/pii/S0379073811001745.

[88] G. Morales, J. Magnusson, H. Hansson, A. Ansell, F. Gálvez, and V. Sánchez-Gálvez. Title : Behaviour of Concrete Structural Members Subjected to Air Blast Loading. pages 936–947, 2013. URL https://www.researchgate.net/publication/283249723_Behaviour_of_concrete_structural_members_subjected_to_air_blast_loading.

[89] M. Oña, G. Morales-Alonso, F. Gálvez, V. Sánchez-Gálvez, and D. Cendón. Analysis of concrete targets with different kinds of reinforcements subjected to blast loading. *The European Physical Journal Special Topics*, 225:265–282, 2016. ISSN 1951-6401. doi: 10.1140/epjst/e2016-02633-8. URL https://doi.org/10.1140/epjst/e2016-02633-8.

[90] MAXAM. RIODIN XE Thechnical Characteristics, 1872. URL https://www.maxamcorp.com/en/blasting-solutions/products/products-list/riodin-he. Accessed: 2021-08-03.

[91] A. Harish. What is Convergence in Finite Element Analysis?, 2020. URL https://www.simscale.com/blog/2017/01/convergence-finite-element-analysis/.

[92] M. Okereke and S. Keates. *Finite Element Applications*. Springer, 2018. ISBN 9783319671246. URL https://link.springer.com/book/10.1007/978-3-319-67125-3.

[93] M. Shuaib and O. Daoud. Numerical modelling of reinforced concrete slabs under blast loads of close-in detonations using the lagrangian approach. *Journal of Physics: Conference Series*, 628:180, 2015. doi: 10.1088/1742-6596/628/1/012065. URL https://www.researchgate.net/publication/280062906_Numerical_Modelling_of_Reinforced_Concrete_Slabs_under_Blast_Loads_of_Close-in_Detonations_Using_the_Lagrangian_Approach.

[94] L. F. Team. AN OVERVIEW OF METHODS FOR MODELLING BOLTS IN ANSYS, 2014. URL https://www.finiteelementanalysis.com.au/featured/an-overview-of-methods-for-modelling-bolts-in-ansys/. Accessed: 2021-06-20.

[95] LSTC. LS-PrePost Online Documentation, 2012. URL https://www.lstc.com/lspp/index.shtml. Accessed: 2021-06-22.

[96] LNLL. A computer code led to entrepreneurial success, 2014. URL https://www.llnl.gov/news/computer-code-led-entrepreneurial-success. Accessed: 2021-08-03.

[97] J. Hallquist. *LS-DYNA Keyword User's Manual I*, volume I. Livermore Software Technology Corportation (LSTC), 2007. ISBN 9254492507. URL https://lstc.com/pdf/ls-dyna_971_manual_k.pdf.

[98] M. Abedini, A. A. Mutalib, C. Zhang, J. Mehrmashhadi, S. N. Raman, R. Alipour, T. Momeni, and M. H. Mussa. Large deflection behavior effect in reinforced concrete columns exposed to extreme dynamic loads. *Frontiers of Structural and Civil Engineering*, 14(2):532–553, 2020. ISSN 20952449. doi: 10.1007/s11709-020-0604-9. URL https://link.springer.com/article/10.1007/s11709-020-0604-9#citeas.

[99] Y. Wu, J. E. Crawford, and J. M. Magallanes. Concrete Constitutive Models. *12th International LS-DYNA Users conference*, (1):1–14, 2012. URL https://www.dynamore.de/de/download/papers/2012-internationale-ls-dyna-users-conference/documents/constitutivemodeling05-a.pdf.

[100] C. Wu, J. Li, and Y. Su. *Development of Ultra-High Performance Concrete Against Blasts*. Eslsevier, 2018. ISBN 9780081024959. URL https://www.elsevier.com/books/development-of-ultra-high-performance-concrete-against-blasts/wu/978-0-08-102495-9.

[101] J. W. Wesevich, B. L. Bingham, J. Magnusson, A. P. Christiansen, and D. D. Bogosian. Comparative Study of Concrete Constitutive Models for Predicting Blast Response. *ACI Symposium Publication*, 281, 2011. doi: 10.14359/51683609. URL https://www.concrete.org/publications/internationalconcreteabstractsportal/m/details/id/51683609.

[102] S. H. Yang, K. S. Woo, J. J. Kim, and J. S. Ahn. Finite Element Analysis of RC Beams by the Discrete Model and CBIS Model Using LS-DYNA. *Advances in Civil Engineering*, 2021, 2021. ISSN 16878094. doi: 10.1155/2021/8857491. URL https://www.hindawi.com/journals/ace/2021/8857491/.

[103] Y. D. Murray, A. Abu-Odeh, and R. Bligh. Evaluation of LS-DYNA Concrete Material Model 159. *Report No. FHWA-HRT-05-063*, (May):209, 2007. URL https://www.fhwa.dot.gov/publications/research/infrastructure/structures/05063/index.cfm.

[104] J. Fish and T. Belytschko. *A First Course in Finite Elements*. WILEY, 2007. ISBN 9780470035801. doi: 10.1002/9780470510858. URL https://www.wiley.com/en-us/A+First+Course+in+Finite+Elements-p-9780470035801.

[105] C. Schmied and T. Erhart. Updated Review of Solid Element Formulations in LS-DYNA. *15. Deutsches LS-DYNA Forum*, (October):1–63, 2018. URL https://www.dynamore.de/de/download/papers/forum11/entwicklerforum-2011/erhart.pdf.

[106] A. Haufe, K. Schweizerhof, and P. Dubois. Review of Shell Element Formulations. *LSTC Developer Forum*, (September):1–35, 2013. URL https://www.dynamore.de/de/download/papers/2013-ls-dyna-forum/documents/review-of-shell-element-formulations-in-ls-dyna-properties-limits-advantages-disadvantages.

[107] G. R. Cowper and P. S. Symonds. Strain-hardening and strain-rate effects in the impact loading of cantilever beams. 1957. URL https://www.semanticscholar.org/paper/STRAIN-HARDENING-AND-STRAIN-RATE-EFFECTS-IN-THE-OF-Cowper-Symonds/489ceb815810086bdcb1375365032377dc966cb6.

[108] Dynamic axial crushing of circular tubes. *International Journal of Impact Engineering*, 2(3):263–281, 1984. ISSN 0734-743X. doi: https://doi.org/10.1016/0734-743X(84)90010-1. URL https://www.sciencedirect.com/science/article/pii/0734743X84900101.

[109] W. Abramowicz and N. Jones. Dynamic progressive buckling of circular and square tubes. *International Journal of Impact Engineering*, 4(4):243–270, 1986. ISSN 0734-743X. doi: https://doi.org/10.1016/0734-743X(86)90017-5. URL https://www.sciencedirect.com/science/article/pii/0734743X86900175.

[110] Y. Jilin and J. Norman. Further experimental investigations on the failure of clamped beams under impact loads. *International Journal of Solids and Structures*, 27(9):1113–1137, 1991. ISSN 0020-7683. doi: https://doi.org/10.1016/0020-7683(91)90114-U. URL https://www.sciencedirect.com/science/article/pii/002076839190114U.

[111] S. Marais, R. Tait, T. Cloete, and G. Nurick. Material testing at high strain rate using the split hopkinson pressure bar. *Latin American Journal of Solids and Structures*, 1:20, 06 2004. URL https://www.lajss.org/index.php/LAJSS/article/download/53/47/50.

[112] H. Jama, M. Bambach, G. Nurick, R. Grzebieta, and X.-L. Zhao. Numerical modelling of square tubular steel beams subjected to transverse blast loads. *Thin-Walled Structures*, 47:1523–1534, 12 2009. doi: 10.1016/j.tws.2009.06.004. URL https://www.researchgate.net/publication/223785563_Numerical_modelling_of_square_tubular_steel_beams_subjected_to_transverse_blast_loads.

[113] M. Sun and J. Packer. High strain rate behaviour of cold-formed rectangular hollow sections. *Engineering Structures*, 62–63:181–192, 03 2014. doi: 10.1016/j.engstruct.2014.01.023. URL https://www.researchgate.net/publication/260231369_High_strain_rate_behaviour_of_cold-formed_rectangular_hollow_sections/citations.

[114] J. Trajkovski. Comparison of MM-ALE and SPH methods for modelling blast wave reflections of flat and shaped surfaces. *11th European LS-DYNA User Conference, Salzburg, Austria*, (May 2017): 15, 2017. URL https://www.researchgate.net/publication/317560674_Comparison_of_MM-ALE_and_SPH_methods_for_modelling_blast_wave_reflections_of_flat_and_shaped_surfaces.

[115] R. Kumar. Mesh convergence study in a highly nonlinear FEA, 2016. URL https://www.researchgate.net/post/mesh_convergence_study_in_a_highly_nonlinear_FEA_problem. Accessed: 2021-06-20.

Appendix A

Influence of Angle of Incidence

As explained in Chapter 2, the following diagrams (Figure B.8 and Figure A.2) present how the impact angle affects the resulting reflection, and consequently, the blast loading on the structure. This allows to calculate the resulting reflection considering its non-linear effects.

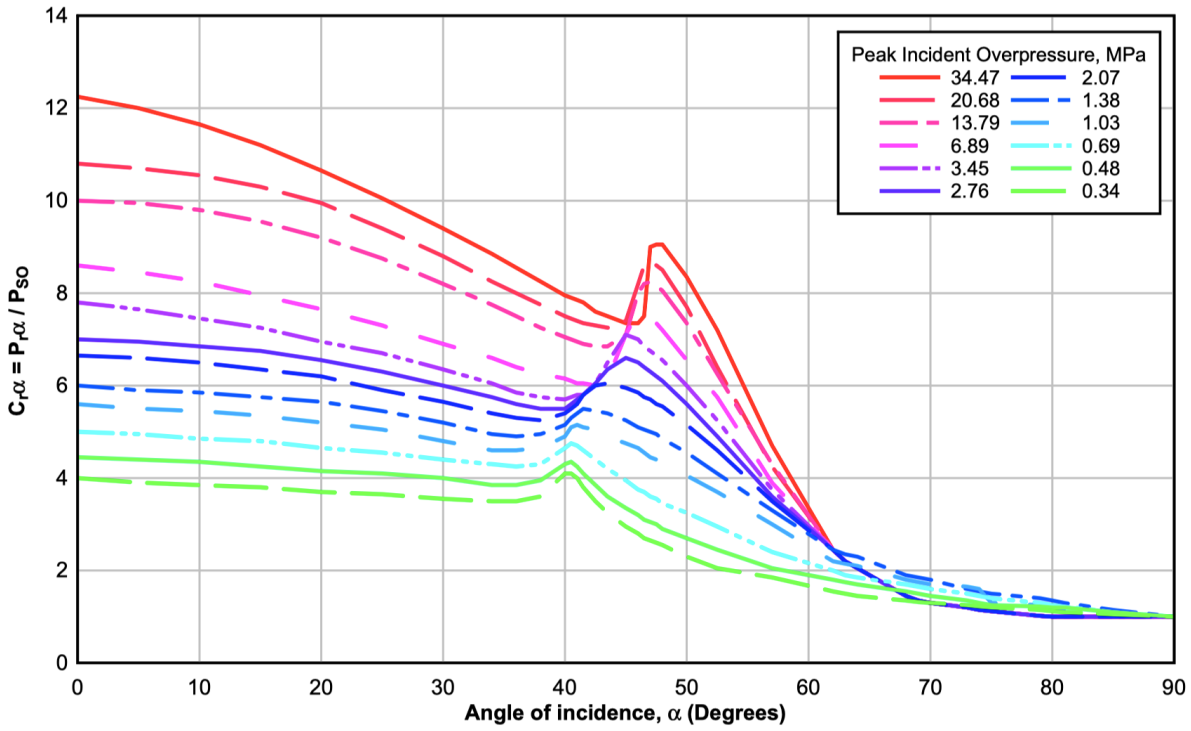

Figure A.1: Influence of angle of incidence on the reflected pressure coefficient for larger incident overpressure values [32].

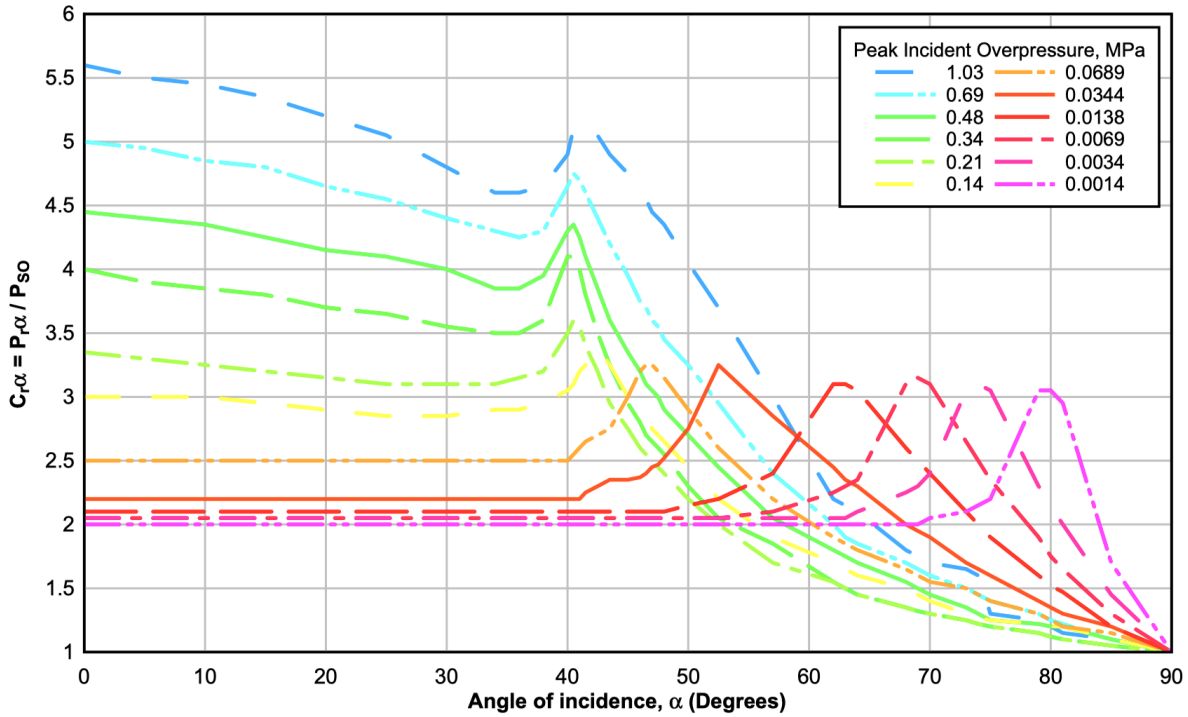

Figure A.2: Influence of angle of incidence on the reflected pressure coefficient for smaller incident overpressure values [32].

Appendix B

LS-DYNA Keywords

The following images, represent a sample of the most relevant LS-DYNA Input cards used throughout the numerical analysis.

```
*TITLE
$#                                                                         title
LS-DYNA keyword deck by LS-PrePost
*CONTROL_ACCURACY
$#     osu       inn    pidosu      iacc
         1         1         0         0
*CONTROL_CONTACT
$#  slsfac    rwpnal    islchk    shlthk    penopt    thkchg     orien    enmass
       0.1       0.0         1         0         1         1         1         0
$#  usrstr    usrfrc     nsbcs    interm     xpene     ssthk      ecdt   tiedprj
         0         0         0         0       4.0         0         0         0
$#   sfric     dfric       edc       vfc        th     th_sf    pen_sf
       0.0       0.0       0.0       0.0       0.0       0.0       0.0
$#  ignore    frceng   skiprwg    outseg   spotstp   spotdel   spothin
         0         0         0         0         0         0       0.0
$#    isym    nserod    rwgaps    rwgdth     rwksf      icov    swradf    ithoff
         0         0         1       0.0       1.0         0       0.0         0
$#  shledg    pstiff    ithcnt    tdcnof     ftall    unused    shltrw    igactc
         0         0         0         0         0                 0.0         0
*CONTROL_ENERGY
$#    hgen      rwen    slnten     rylen     irgen
         2         2         2         2         2
*CONTROL_HOURGLASS
$#     ihq        qh
         1       0.1
```

Figure B.1: Control and Database Parameters - Part I.

```
*CONTROL_ENERGY
$#    hgen      rwen    slnten     rylen     irgen
         2         2         2         2         2
*CONTROL_HOURGLASS
$#     ihq        qh
         1       0.1
*CONTROL_TERMINATION
$#  endtim    endcyc     dtmin    endeng    endmas     nosol
      0.04         0       0.0       0.01.000000E8         0
*CONTROL_TIMESTEP
$#  dtinit    tssfac      isdo    tslimt     dt2ms      lctm     erode     mslst
      0.03       0.6         0       0.0       0.0         0         0         0
$#  dt2msf   dt2mslc     imscl    unused    unused     rmscl    unused      ihdo
       0.0         0         0                             0.0                   0
```

Figure B.2: Control and Database Parameters - Part II.

```
*LOAD_BLAST_SEGMENT_SET
$#     bid      ssid    alepid     sfnrb    scalep
         1         1         0       0.0       1.0
*LOAD_BLAST_ENHANCED
$#     bid         m       xbo       ybo       zbo       tbo      unit     blast
         1     14.15      2.71       1.0      0.08       0.0         2         1
$#     cfm       cfl       cft       cfp     nidbo     death    negphs
         0.0       0.0       0.0       0.0          01.00000E20         0
*LOAD_BODY_Z
$#    lcid        sf    lciddr        xc        yc        zc       cid
         2       9.8         0       0.0       0.0       0.0         0
```

Figure B.3: Blast Load Parameters (Experimental Load).

```
*PART
$#                                                                         title
Concrete Wall
$#     pid      secid       mid     eosid      hgid      grav    adpopt      tmid
         1          1       159         0         1         0         0         0
*SECTION_SOLID_TITLE
Solid
$#   secid    elform       aet    unused    unused    unused    cohoff    unused
         1         1         0                                     0
*MAT_CSCM_CONCRETE_TITLE
Concrete
$#     mid        ro     nplot     incre     irate     erode     recov   itretrc
       159    2500.0         1       0.0         1       1.1       0.0         0
$#    pred
         0.0
$#     fpc      dagg     units
3.000000E7       0.0         4
```

Figure B.4: Concrete Material Part.

```
Inverted Cylinder
$#     pid      secid       mid     eosid      hgid      grav    adpopt      tmid
         2          2       160         0         1         0         0         0
*SECTION_SHELL_TITLE
IC Thickness
$#   secid    elform      shrf       nip     propt   qr/irid     icomp     setyp
         2         2       1.0         2       1.0         0         0         1
$#      t1        t2        t3        t4      nloc     marea      idof    edgset
     0.002     0.002     0.002     0.002       0.0       0.0       0.0         0
*MAT_PLASTIC_KINEMATIC_TITLE
Inverted Cylinder
$#     mid        ro         e        pr      sigy      etan      beta
       160    7850.02.10600E11       0.33.710000E8       0.0       0.0
$#     src       srp        fs        vp
    3023.0      1.65       0.0       0.0
```

Figure B.5: Steel Connector Material Part.

```
*CONTACT_INTERIOR
$#    psid
         2
*CONTACT_AUTOMATIC_SINGLE_SURFACE_ID
$#     cid                                                                title
         0Inverted Cylinder
$#    ssid      msid     sstyp     mstyp    sboxid    mboxid       spr       mpr
         2         0         3         0         0         0         0         0
$#      fs        fd        dc        vc       vdc    penchk        bt        dt
       0.0       0.0       0.0       0.0       0.0         0  0.01.00000E20
$#     sfs       sfm       sst       mst      sfst      sfmt       fsf       vsf
       1.0       1.0       0.0       0.0       1.0       1.0       1.0       1.0
$#    soft    sofscl    lcidab    maxpar     sbopt     depth     bsort    frcfrq
         0       0.1         0     1.025       2.0         2         0         1
$#  penmax    thkopt    shlthk     snlog      isym     i2d3d    sldthk    sldstf
       0.0         0         2         0         0         0       0.0       0.0
*CONTACT_AUTOMATIC_SURFACE_TO_SURFACE_ID
$#     cid                                                                title
         0Support
$#    ssid      msid     sstyp     mstyp    sboxid    mboxid       spr       mpr
         5         4         3         3         0         0         0         0
$#      fs        fd        dc        vc       vdc    penchk        bt        dt
       0.0       0.0       0.0       0.0       0.0         0  0.01.00000E20
$#     sfs       sfm       sst       mst      sfst      sfmt       fsf       vsf
       1.0       1.0       0.0       0.0       1.0       1.0       1.0       1.0
```

Figure B.6: Contacts.

```
*CONSTRAINED_LAGRANGE_IN_SOLID_TITLE
$#  coupid                                                                title
         0Beam and Concrete
$#   slave    master     sstyp     mstyp     nquad     ctype     direc     mcoup
         1         1         0         1         0         2         1         0
$#   start       end      pfac      fric    frcmin      norm   normtyp      damp
       0.0 1.00000E10       0.1       0.0       0.5         0         0       0.0
$#      cq      hmin      hmax     ileak     pleak   lcidpor     nvent  blockage
       0.0       0.0       0.0         0       0.1         0         0         0
$#  iboxid   ipenchk   intforc   ialesof    lagmul    pfacmm      thkf
         0         0         0         0       0.0         0       0.0
$#      a1        b1        a2        b2        a3        b3             poreini
       0.0       0.0       0.0       0.0       0.0       0.0         0       0.0
*CONSTRAINED_NODAL_RIGID_BODY
$#     pid       cid      nsid     pnode      iprt    drflag    rrflag
         7         0         8    720187         0         0         0
```

Figure B.7: Constrains.

```
*DATABASE_NCFORC
$#      dt    binary      lcur     ioopt
     0.001         0         0         1
*DATABASE_NODFOR
$#      dt    binary      lcur     ioopt
     0.001         0         0         1
*DATABASE_RCFORC
$#      dt    binary      lcur     ioopt
1.00000E-4         0         0         1
*DATABASE_SPCFORC
$#      dt    binary      lcur     ioopt
     0.001         0         0         1
*DATABASE_BINARY_BLSTFOR
$#      dt      lcdt      beam     npltc    psetid
1.00000E-4         0         0         0         0
*DATABASE_BINARY_D3PLOT
$#      dt      lcdt      beam     npltc    psetid
1.00000E-4         0         0         0         0
$#   ioopt      rate    cutoff    window      type      pset
         0       0.0       0.0       0.0         0         0
```

Figure B.8: Outputs.